THE UNIVERSITY OF CALGARY

Rayleigh-Wave Analysis and Removal Using a Novel Weighted Median Filter

by

David G. Schieck

A THESIS

SUBMITTED TO THE FACULTY OF GRADUATE STUDIES

IN PARTIAL FULFILMENT OF THE REQUIREMENTS FOR THE

DEGREE OF MASTER OF SCIENCE

DEPARTMENT OF GEOLOGY AND GEOPHYSICS

CALGARY, ALBERTA

NOVEMBER, 1993

THE UNIVERSITY OF CALGARY

FACULTY OF GRADUATE STUDIES

The undersigned certify that they have read, and recommended to the Faculty of Graduate Studies for acceptance, a thesis entitled "Rayleigh-wave analysis and removal using a novel weighted median filter" submitted by David G. Schieck in partial fulfilment of the requirements for the degree of Master of Science.

Supervisor, Dr. R.R. Stewart,
Department of Geology and Geophysics

R.J. Brown

Dr. R.J. Brown,
Department of Geology and Geophysics

Dr. F.A. Cook,
Department of Geology and Geophysics

Dr. R.M. Rangayyan,
Department of Electrical and Computer Engineering

Date: September 23, 1994

Abstract

In this study a non-linear, hybrid *f-k* filter is used to remove aliased dipping events and random noise glitches from a seismic shot gather. This weighted median filter uses time-domain coefficients, from the inverse Fourier transform of a dip or velocity filter developed in the frequency domain, as the filter weights. This results in a filter which has median characteristics but also rejects dips analogous to an *f-k* velocity filter. A fast 2-D median filter algorithm is developed and applied to synthetic and real P-SV data from the Springbank area of Alberta.

Rayleigh waves travelling in the near-surface are often dispersive (phase velocity is dependent on frequency). Three methods of estimating dispersion parameters are evaluated in this study: namely, narrowband filter analysis, shear-wave refraction, and the ω-p transform. A linear approximation to the dispersion curve is used to compress dispersive noise for synthetic data, Springbank data, and a multicomponent data set from Wyoming.

Acknowledgements

This thesis is dedicated to my wife, Cindy L. Adams, whose warm encouragement and thoughtful listening strongly influenced the realization of this work. I would like to thank my advisor, Dr. Robert R. Stewart, for his discussions, suggestions, and careful criticism of this work, always expanding my understanding of geophysics. Special thanks go to the computer "wizards" Ms. Catherine (Tina) E. Howell, Mr. Malcolm Bertram, and Mr. Henry C. Bland for developing and maintaining an outstanding computer environment for seismic research. Dr. Don Lawton initiated and supervised the field school which provided the reflection sections from Jumping Pound used in this study. Finally many thanks to my colleagues within the CREWES (Consortium for Research in Elastic Wave Exploration Seismology) group for their criticism, scepticism, and support as I developed the ideas and theory contained in this thesis.

This research was supported by a Post-graduate NSERC (Natural Sciences and Engineering Research Council) scholarship. The much appreciated computer facilities and staff were a direct result of the CREWES sponsors. Geo-X Systems Ltd. of Calgary, Alberta, generously provided their IBM 3081 mainframe computer for the development and application of the α-trim mean and phase matched filters.

Table of Contents

List of Tables

List of Figures

Chapter 1 INTRODUCTION

1.1 Definitions

Conventional seismic acquisition uses a compressional source and geophones sensitive to the vertical axis ground motion. Present day seismic surveys are conducted with geophones capable of sensing motion in the horizontal directions and so provide multicomponent data sets. Compressional or P-waves reflected or transmitted through an elastic boundary (i.e. change in shear or compressional velocity or change in density) give rise to shear waves (Aki and Richards, 1980). Given isotropic media, horizontal layering, and the range of incidence angles commonly used, these shear waves contain a vertical component. Such waves are called SV waves, and provide additional lithologic information not available through conventional seismic recording (Fertig and Krajewski, 1989). Three-component recording is directed at improving conventional P-wave sections while also recording and analyzing previously unavailable shear-wave data.

In SV recording, as geophone or source arrays are not generally used because these arrays can attenuate the desired shear wavefield, Rayleigh waves have significant amplitudes relative to reflected events. A Rayleigh wave is a large-amplitude, direct-arriving surface wave, elliptically polarized in the plane of the propagation. The particle motion is retrograde at the free surface, and its amplitude decreases exponentially to a depth equal to 0.192 times the wavelength (for a homogeneous half-space) at which point the particle motion becomes prograde (Dobrin *et al.*, 1951).

Multichannel filters are routinely used to remove linear, steeply dipping noise, such as Rayleigh or air waves, from a shot record before stacking to common reflection point sections (Yilmaz, 1987; Hatton *et al*,1986). A new dip-rejecting α-trim mean filter described in this thesis removes unwanted noise spikes and aliased dipping events better than *f-k* dip filters. This study evaluates the characteristics of the new hybrid filter on synthetic and real data.

When multiple near-surface layers are present, Rayleigh waves are dispersive (velocity varies with frequency). This characteristic has been used to infer near-surface shear-wave lithology (Mari, 1984; Szelwis and Behle, 1987;Gabriels *et* *al.*,1987; and Wattrus, 1989) and to separate or remove ground roll from the seismic record (Beresford-Smith and Rango, 1988; Saatçilar and Canitez, 1988; and Herrmann and Russell, 1990). In this study, a matched filter, based on a linear frequency-modulated approximation of the dispersion, is used to compress the Rayleigh wave before multichannel filtering.

1.2 The need for Rayleigh-wave filtering

The frequency range of Rayleigh waves (often approximately 4-20 Hz for land data in Alberta) is within the frequency bandwidth of P-SV wave data (typically 8-35 Hz for the data in this study). This precludes the use of narrowband filters or deconvolution to suppress or remove them without degrading the reflections. In P-wave conventional recording, it is standard practice to use geophone arrays which attenuate non-vertically propagating wave motion such as ground roll. However, the desired P-SV wave motion is also attenuated by these receiver arrays, and hence single or nested geophones are generally used for multicomponent recording.

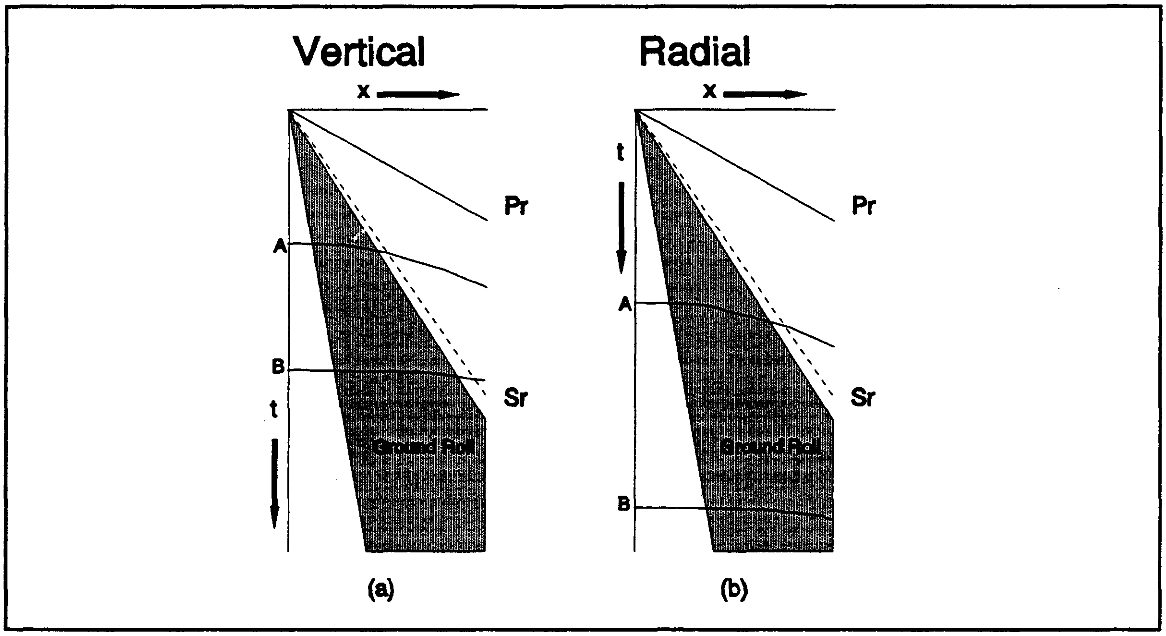

Figure 1.1 Diagram of vertical- (a) and radial- (b) wave shot gathers showing the position of refracted arrivals (Pr and Sr), ground-roll window, and reflection events (A&B). x is distance and t is time.

As depicted in Figure 1.1(a), between the "first arrivals" of the refracted P-wave (Pr) and the earliest arriving Rayleigh waves, there is a favourable P-wave reflection window within which events **A** and **B** may be adequately recorded. The velocities of shear waves are very close to the velocity of Rayleigh waves (refer Fig. 1.2), particularly in the near surface where Poisson's ratio is usually higher than 0.4 (Knopoff, 1952). Therefore source-generated shear waves which are refracted (Sr) in the near surface arrive only slightly before the ground roll. P-SV wave reflections typically are delayed by 1.5 times their associated P-wave reflections ('assuming Vp/Vs=2), and thus events **A** and **B** will often be contaminated with large-amplitude Rayleigh wave noise (Figure 1.1 (b)).

Due to low-energy sources or limitations in recording parameters (i.e. limited number of channels for 3-C data) the optimum window may not be available at the target depth for shallow reflection seismology. A robust, efficient method must be developed to obtain the required reflection signals from within the large-amplitude surface-wave window.

1.3 Noise on a converted-wave record

With the advent of multicomponent recording and the recent studies indicating its benefits, it is timely that the noise on a converted wave record should be analyzed. Three general categories of noise will be addressed: random noise, bad traces or noise glitches (spiky noise) and coherent dipping noise such as surface waves or head waves.

1.3.1 Random noise

Conventional vertical-component acquisition employs multigeophone arrays or strings, usually of nine geophones, to improve the signal-to-noise ratio (S/N) on the seismic record. The S/N ratio of random noise can be reduced by at best $\sqrt{N}$ where N is the number of geophones. On conventional P-wave array data then, the S/N ratio is 3 times better than it is on single-geophone, multicomponent records. In the case of multicomponent data only single geophones are generally used: i) due to cost considerations, and ii) because arrays cancel not only the unwanted surface waves but also the shear wavefield. In fact, geophone arrays should be considered cautiously in the field if the goal is to analyze the full vector wavefield (Miller *et al*, 1990) assuming the dynamic range of the recording instruments is sufficient.

1.3.2 Aliased dipping noise

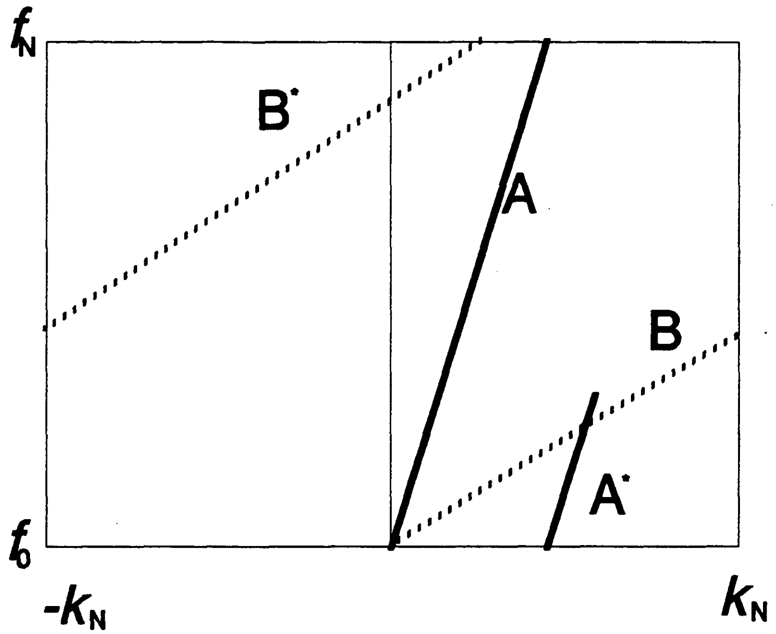

Figure 1.2 Spatial aliasing in the *f-k* domain. Dipping event A aliased in time and B aliased in space where *f* is frequency and *k* is wavenumber.

Spatially aliased noise on a pre-stack gather occurs when the ratio of spatial wavenumber to temporal frequency, or dip, wraps around to the opposite dip in the *f-k* domain. Event A (Figure 1.2) is not spatially aliased although it could be temporally aliased as shown by A^*. Event B is spatially aliased and reappears at a negative dip as B^*. In the time domain, spatial aliasing can be recognized by dip reversal. Time-domain filtering may not suffer from this problem as it arises in the Fourier transformation of the data (Hatton *et al.*, 1986). For example, shallow converted reflections may arrive before the shear headwaves, and thus a first-break mute to remove these headwaves would also remove the shallow events. These headwaves may be removed with a dip-reject filter such as an *f-k* filter; however these low-frequency, low-velocity arrivals often have aliased dips, and hence are difficult to remove with a dip-reject filter (Yilmaz, 1987).

1.3.3 Surface waves

Rayleigh waves and Love waves are large-amplitude, low-frequency, low-velocity events on the seismic shot gather. The bandwidth of these noise trains overlaps the bandwidth of shear-wave signals. This overlap in frequencies makes surface waves difficult to separate from the converted wave reflection events on the basis of frequency alone. However, in the case of multiple near-surface layers these waves are dispersive; that is, their phase velocity is a function of frequency (Al-Husseini *et al.*, 1981). This property can be exploited in order to separate surface waves from the underlying converted wave reflections (Saatçillar and Canitez, 1988; Herrmann and Russell, 1990).

1.3.4 Spikes, glitches, and bad traces

When planting a single multicomponent geophone, great care must be taken to ensure good coupling with the ground. In the case of a multigeophone array or string, the chances of all receivers having poor coupling is small. Generally, the raw records obtained from the single-receiver case have more bad traces, poorer S/N ratio, and smaller amplitude range (Edelmann and Helbig, 1987); more editing is required and often there will be more large-amplitude spikes (time-limited large-amplitude wavelet) or glitches (data samples missing or in error).

1.4 Thesis objective

The purpose of this thesis is basically two-fold. First, to design and implement a new pre-stack, nonlinear filter which attenuates unwanted noise, primarily Rayleigh waves, on a multicomponent record. Second, to optimize the new filter by estimating and compressing the dispersion characteristics of Rayleigh waves. The goal then is to improve the quality of a converted-wave stack by improving the S/N ratio of pre-stack records.

1.5 Data sets used

Five data sets are used to demonstrate the concepts in this thesis. Synthetic P-SV component shot gathers are used to depict the abilities of the weighted α-trim mean filter in removing unwanted random or aliased noise. The two-component converted wave reflection profile is used as a real data example of this algorithm. A multicomponent synthetic shot gather demonstrates the full vector wavefield of surface waves and their dispersive properties. Finally, the analysis and filtering of dispersive Rayleigh waves are demonstrated with two separate multicomponent P-SV wave reflection sections.

1.5.1 Synthetics

Two synthetic shot gathers were generated for this study. The P-SV shot gather was used to demonstrate the weighted α-trim mean filter. The multicomponent ground-roll shot record enabled testing of the dispersion algorithms and inversion.

1.5.1.1 Kinematic vertical-component shot gather

Synthetic data set were generated using a program written in Fortran for an IBM 3081 mainframe computer made available by Geo-X Systems Ltd. The P-SV velocity function, consisting of 11 time-velocity pairs from the Springbank example (section 4.3), served as the model to generate hyperbolic reflection events in the form of a shot gather. An offset-varying amplitude and zero-phase band-limited (10-70 Hz) wavelet was assumed to generate the converted reflection events. These events have equivalent zero-offset amplitudes and no reflection multiples are calculated. The linear dipping events are created by assuming a zero-phase band-limited wavelet time shifted at the given dip specified in ms/trace. Random Gaussian noise with the same bandwidth as the primary converted reflections was added to these synthetics with an root mean squared (RMS) amplitude 1/4 of the peak amplitude of the primaries. Three noise spikes, again with the same bandwidth of the primaries, were also added at 4 times the peak amplitude of the primaries. The synthetic shot gathers are shown in section 2.4.2 to demonstrate the *f-k* weighted α-trim mean filter.

1.5.1.2 Full-wavefield shot gather

A full-wave equation synthetic package (VESPA from Sierra Corp.), available on the CREWES IBM 4381 computer, can generate a single shot or VSP full wavefield record using matrix propagation. The model used in this case incorporated three shallow layers on top of a half-space with P- and S-wave velocities shown in Table 1.1 as per a previous refraction study (Lawton, 1990).

	Vp (m/s)	Vs (m/s)	Thickness (m)	ρ (gm/cm^3)
Weathering	600	295	10	2.2
Drift	2450	295	10	2.2
Half space	3150	1300	∞	2.2

Table 1.1 Velocities used for full-wavefield VESPA synthetic shot gathers.

The density is constant in all layers at 2.2 gm/cm^3. An isotropic model was assumed with a quality factor of Q=2000 (very low attenuation). Only vertical and radial components are generated using the following parameters:

Number of traces:	48
Station interval:	30 m
Source type:	3-D point source
Source depth:	12 m
Minimum offset:	30 m
Maximum offset:	1440 m
Sample rate:	2 ms
Record length:	4 s

These shot records are presented in section 3.3 as part of the discussion on dispersion estimation. Two additional models demonstrate the effects of increased spatial sampling (ie. Model 2, station interval = 10m) and weathering thickness (ie. Model 3, weathering = 5m) on the ω-p transforms.

1.5.2 Real data

Three real data sets are used in this study. The first is a two-component data set acquired by the University of Calgary 1990 Geophysics Field School, from the Springbank area of Alberta. The second is a three-component data set from the same area recorded the following year. The third is a multicomponent data set, shot by Union Oil of California (UNOCAL) in the Casper Creek field area of Natrona County, Wyoming.

1.5.2.1 Two-component reflection data

The two-component field data set (FS90-1) was recorded in August, 1990, as part of the Geophysics Field School course at Springbank, Alberta (Twp 25, Rge 3 W5). Data from a dynamite source were recorded on vertical- and radial-component geophones with the following parameters:

Number of traces:	48
Station interval:	30 m
Geophones:	3-C Oyo, 10 Hz
Minimum offset:	30 m
Maximum offset:	1440 m
Source:	dynamite, 1 kg
Source depth:	10-15 m
Instruments:	Sercel 338HR
Sample interval:	2 ms
Record length:	6 s
Fold:	24

The resulting P-SV converted-wave reflection section is shown in section 2.4.3 as part of the real data demonstration of the weighted α-trim mean filter.

1.5.2.2 Three-component shallow reflection data

The three-component field data (FS91-1) was recorded in August, 1991 and ties the previous years two-component data to the east (refer Fig.1.2). A Betsy 8-gauge seisgun shot at the surface was the energy source. This generated surface-wave

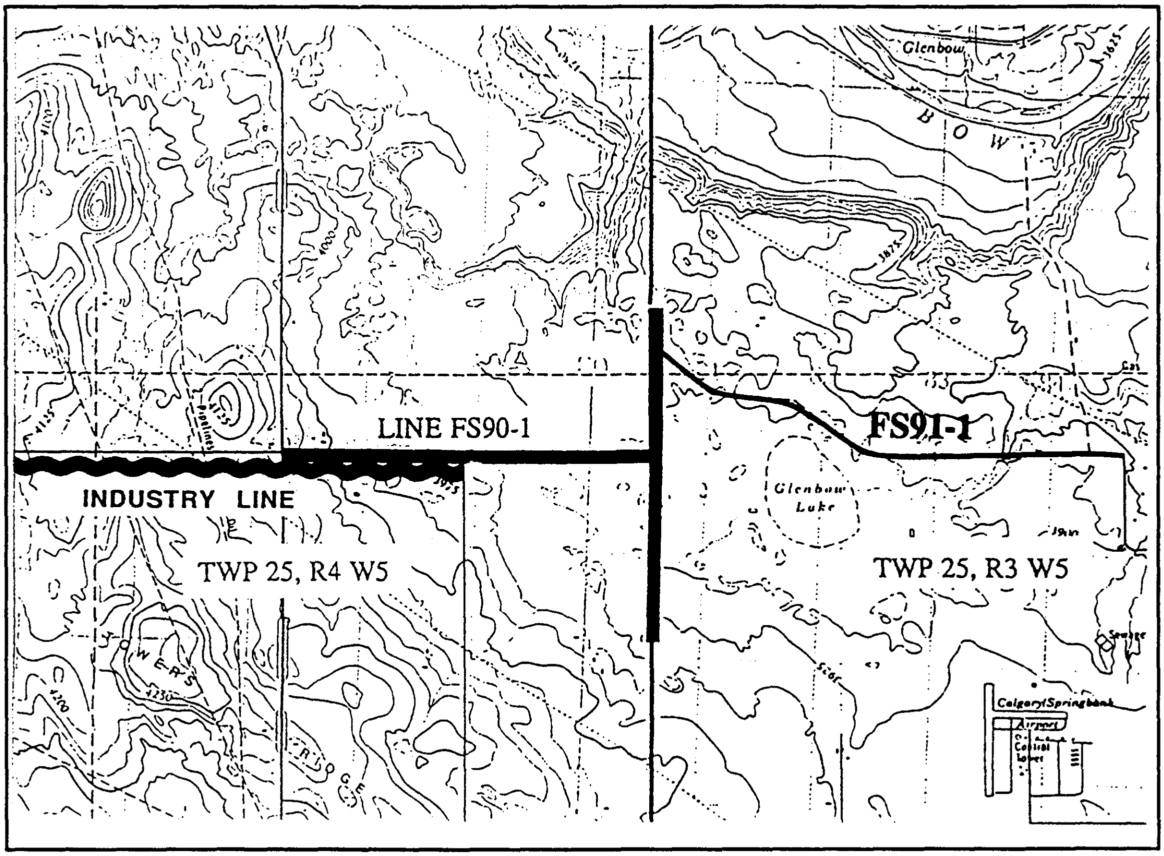

Figure 1.3 Springbank Alberta showing locations of lines FS90-1 and FS91-1.

energy on all three recorded components. This data set was used to demonstrate the application of phase matched filtering in conjunction with weighted α-trim mean filtering to reduce dispersive ground roll on a pre-stack record (refer to section 3.5.2 and 4.5.1). Only the vertical component was considered because no appreciable reflection energy could be observed on the radial or horizontal components. The field parameters for this second line are:

Number of traces:	32
Station interval:	10 m
Geophones:	3-C Oyo, 10 Hz
Minimum offset:	10 m
Maximum offset:	160 m
Instruments:	Sercel 338HR
Sample interval:	2 ms
Record length:	1 s
Fold:	40

1.5.2.3 South Casper Creek

This three-component data set was acquired by UNOCAL in 1988. A single cable, consisting of eighty three-component geophones, was placed in a line (no station roll). A dynamite source was rolled through this cable starting at 600 meters from the first geophone and ending 600 meters off the last geophone for a total line length of 2400 meters. The field parameters for this line were:

Number of traces:	240 (80 X 3-components)
Station interval:	15 m (50 ft)
Shot point:	60 m (200 ft)
Geophones:	3-C,10 Hz
Minimum offset:	15 m
Maximum offset:	1200 m
Instruments:	MDS-10
Sample interval:	2 ms
Source type:	Dynamite, 4.5 kg (10 lbs)
Source depth:	46 m (150 ft)
Record length:	4 s
Fold:	20

These data are depicted in Chapter 4.5 for the final applications of the α-trim f-k and linear frequency compression filters.

Chapter 2 WEIGHTED MEDIAN FILTERS

2.1 Introduction

Two statistical estimates often used in image enhancement and seismic processing are the mean and the median (Claerbout,1985). Median filters, first introduced by Tukey (1971) as an alternative to running average filters for smoothing data, are more robust because noise spikes or glitches are not included in the estimate (Claerbout and Muir, 1973). The mean minimizes the sum of the squares of the differences around a point, and the median minimizes the sum of the absolute values of the differences. Both are measures of the central tendency of a given distribution of points, and there are many reasons why one might be considered preferable to the other for smoothing and filtering data.

Applications of median filters to geophysical data are relatively few. Claerbout and Muir (1973) discuss the use of median filters to detect first arrivals and also describe the related L_1 norm inversion. Evans (1982) applies a median filter as a general de-spiker for coded time signals. A clear description of how the mean relates to the median as a filter is given by Bednar (1983). Directional median filters to remove linear noise from a seismic record (Kirlin *et al.*, 1985) and noise from a vertical seismic profile (Hardage, 1983) have been presented (Stewart, 1985). Green (1986) introduced the idea of removing spurious events from a seismic trace with a 1-D median filter followed by a Lagrangian interpolator to replace clipped maxima and minima. The concept of compound median filtering (Leaney and Ulrych, 1992), which reduces the input data to a series of root signals with blocks of a certain length, is applied to log processing to obtain "blocky" signals.

2.2 Median filter characteristics

For a normal distribution of data, the median and the mean are exactly the same for an odd number of points, and for large sample distributions (Bednar, 1983). However, if a distribution is skewed or has a large central peak, the median is a better estimate of the central point of the distribution. A method of evaluating the quality of the mean or median estimate based on the mean-squared-error (MSE) is given by Bovik *et al.*, 1983. Further, it has been shown that the quality of the mean estimate is unrelated to the skew or kurtosis of a given distribution, but that the quality of the median estimate improves with increased kurtosis or skew (Stavig and Gibbons, 1977).

In the case of a normal distribution of random variables (x_i) it has been shown (Justusson, 1981) that the variance of the median is:

$$VAR[Median(x_1,...,x_n)] \approx \frac{\sigma^2}{n+\frac{\pi}{2}-1} \cdot \frac{\pi}{2}, \qquad n=1,3,5,... \tag{2.1}$$

where the mean of n random variables has a variance of σ^2/n. This means that for normal white noise, the variance of the median is approximately 57% larger than for the mean.

2.2.1 Relating the mean to the median

We can define a quantity L_2 as the sum of the squared differences between x_{mean} and a data series x_i, where N is the number of samples in the filter window as

$$L_2 = \sum_{i=1}^{N} (x_{mean} - x_i)^2 \tag{2.2}$$

Then L_2 can be minimized by setting its partial derivative with respect to x_{mean} to zero giving

$$x_{mean} = \frac{1}{N} \sum_{i=1}^{N} x_i \tag{2.3}$$

We can also minimize L_1, the sum of absolute values of the differences (Claerbout, 1985) as

$$L_1 = \sum_{i=1}^{N} |x_{median} - x_i| \ . \tag{2.4}$$

Again this can be minimized by setting the partial derivative of L_1 equal to zero, resulting in

$$\sum_{i=1}^{N} sgn(x_{median} - x_i) = 0 \ , \tag{2.5}$$

where the sgn function is +1 when the difference is positive and -1 when the difference is negative. Equation (2.5) formally defines x_{median} so that it is greater than x_i for *N/2* terms and less for the other N/2 terms. Note that if *N* is an even number equation 2.4 suggests that x_{median} be between the middle two values of x_i or, explicitly, the average of the two middle values. The mean of data samples x_i can be related to the median with the α-trim mean concept (Bednar, 1983; Bednar and Watt, 1984).

$$x_\alpha = \frac{1}{N-2\alpha(N-1)} \sum_{i=1+\alpha(N-1)}^{N-\alpha(N-1)} x_i \tag{2.6}$$

where x_i is the *i*th data item in the sorted sample array ($x_1 \leq x_2 \leq x_3 .. x_N$) and *N* is the number of samples. The α-trim mean, with values greater than 0 and less than 1/2, removes extraneous data values from the filter window before averaging. The median ($\alpha=0.5$) and the mean ($\alpha=0$) are continuous limits of the α-trim averages.

Figure 2.1 shows the use of eq.(2.6) by filtering a 400-sample random noise trace with a 21-point running average type α-trim filter. Increments in α of 0.05 from the mean ($\alpha=0.0$) to the median ($\alpha=0.5$) are used. Note the similar character of all filtered outputs. Running average mean filters are time-invariant and can easily be described in the frequency domain by a very simple transfer function, *sinc(x)* or *sin(x)/x*. Alpha-trim mean filters ($\alpha>0.0$) are a class of time-variant, data-dependent filters. Figure 2.2 is the frequency domain representation of the time-domain traces. We can see that the amplitude spectra are similar, especially below $\omega \leq 2\pi/n$ where n is the number of filter points (ie. 21). This is in agreement with Justusson (1981), where he observes that the transfer functions of both the running mean and median are similar within this range, but that the median is irregular above this range.

2.2.2 2-D median filters

Two applications of 1-D median filters to 2-D data will be discussed next, namely the separable or two-pass and the square or one-pass median filters. The separable or two-pass median filter consists first of filtering each row of a 2-D data set with a 1-D median filter. The resulting output data set is then filtered by a second one-dimensional filter, usually the same as the first, along each column (Narendra, 1978). The square or one-pass median filter consists of passing a 2-D window, usually

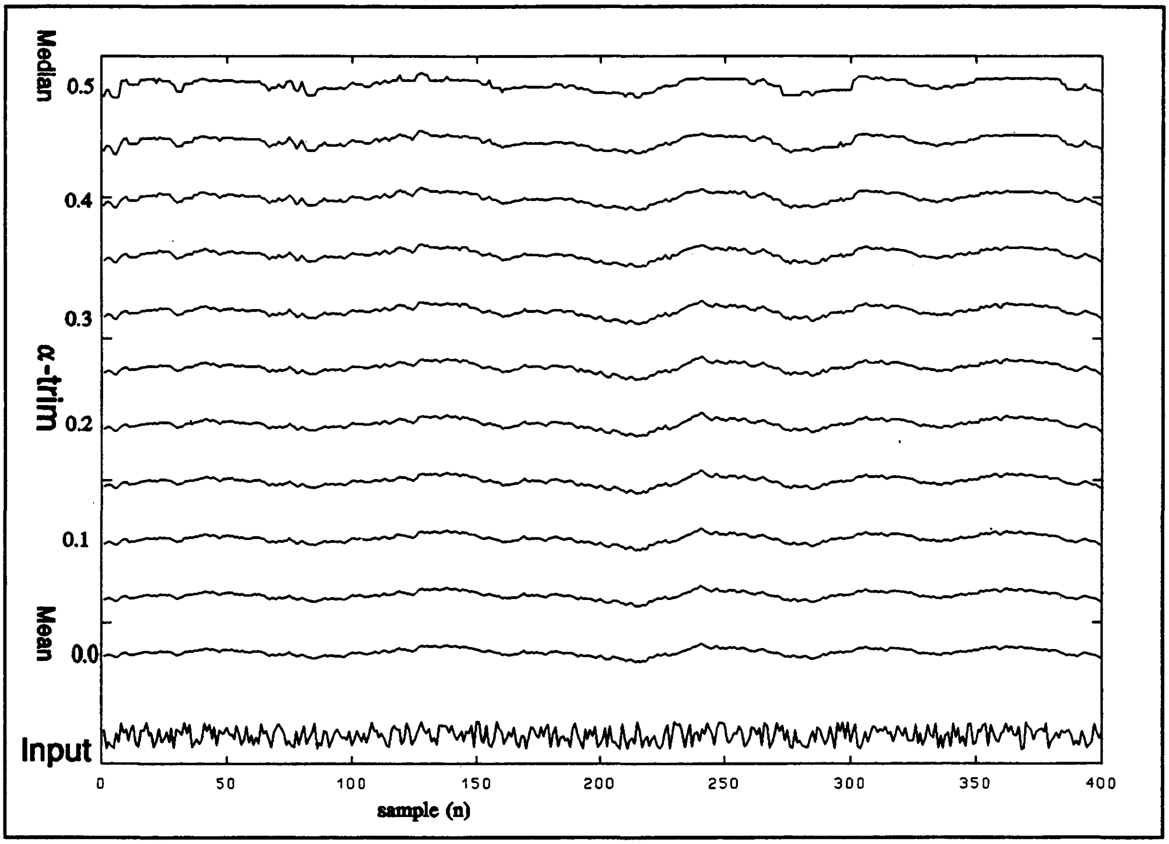

Figure 2.1 Random noise filtered with α-trim mean ($0.0 \leq \alpha \leq 0.5$).

a square box, across the data set. The output at each position is taken as the median of the data values within the window (Liao *et al*, 1985).

A simple 2-D image is shown in Figure 2.3; the same image after normally distributed random noise (mean=0.0, σ=1.0) is shown in Figure 2.4. This image consists of a raised 10x10 square block (left), a 3x3 block (top), a raised triangular block (right), two raised crossing lines (front), and a 10x10 pyramidal block (centre). The results of the application of a 5x5 simple median filter are depicted in Figures 2.5 and 2.6. The mean squared error (MSE) of the image is obtained by taking the square root of the differences of the original input (no noise added) squared and the output of the filters. The MSE is calculated only for the 10x10 square and triangular blocks, and the central pyramid; the other three components were intended as noise to be removed. The one-pass filter produces a smoother output with MSE equal to 3.802. The two-pass filter preserves the sharp corners of the raised blocks better, and has an MSE of 0.984.

The results of first applying the row filter followed by the column filter had

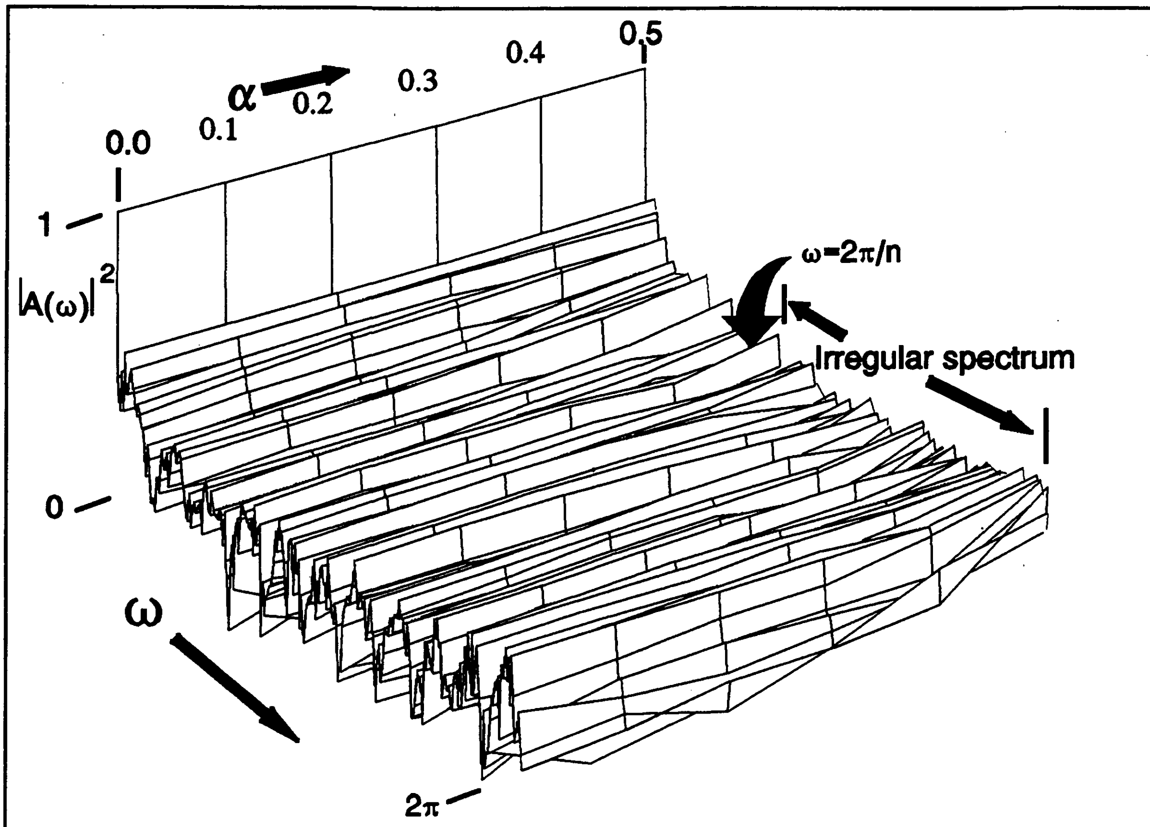

Figure 2.2 Frequency domain representation of α-trim filtered random noise traces of Figure 2.1.

similar MSE but different output values than the same operation in reverse order (ie. applying the column filter first followed by the row filter). This is due to the non-linear or data-dependent characteristics of the median filter.

The two-pass operation does not remove the raised 3x3 block because 1-D median filters do not affect shapes greater than 1/2 the operator length (ie. for n=5, only glitches less than 3 will be removed). However, the one-pass filter treats the moving window square as a single long array of 5x5 or 25 data points in the median process. This implies that 2-D glitches less than 12 points will be removed; hence the disappearance of the 3x3 raised block (i.e. 9 raised data points). The one-pass simple median filter is more powerful in its discrimination of 2-D signals over noise (Justusson, 1981). Stewart and Schieck (1993) found similar results for seismic data in the case of two-pass 3-D filtering when compared to one-pass applications.

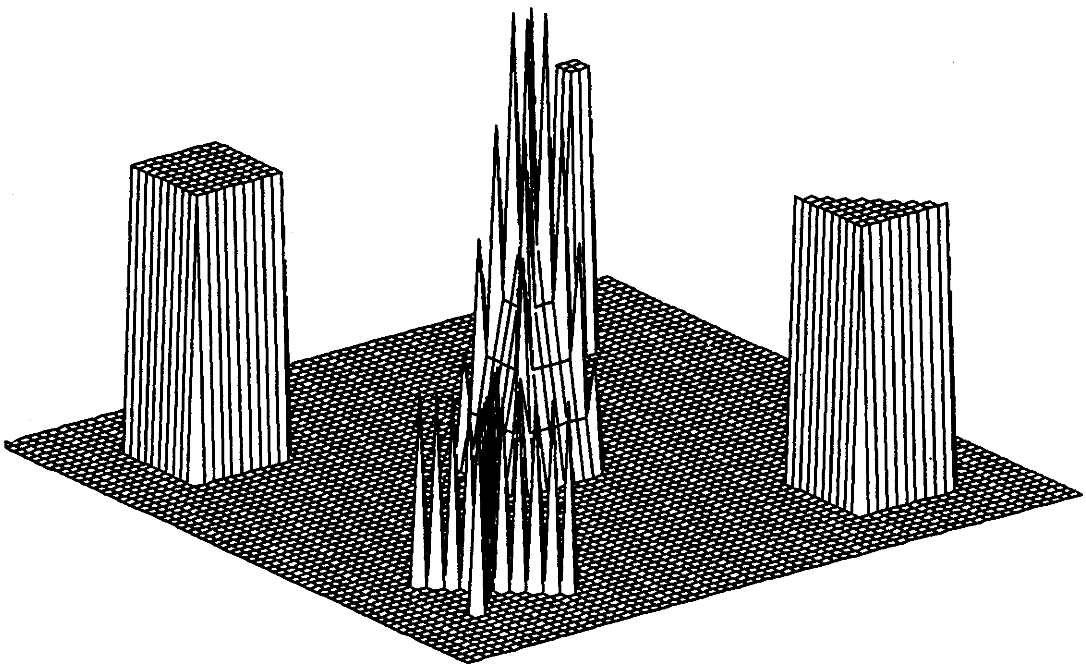

Figure 2.3 Test image.

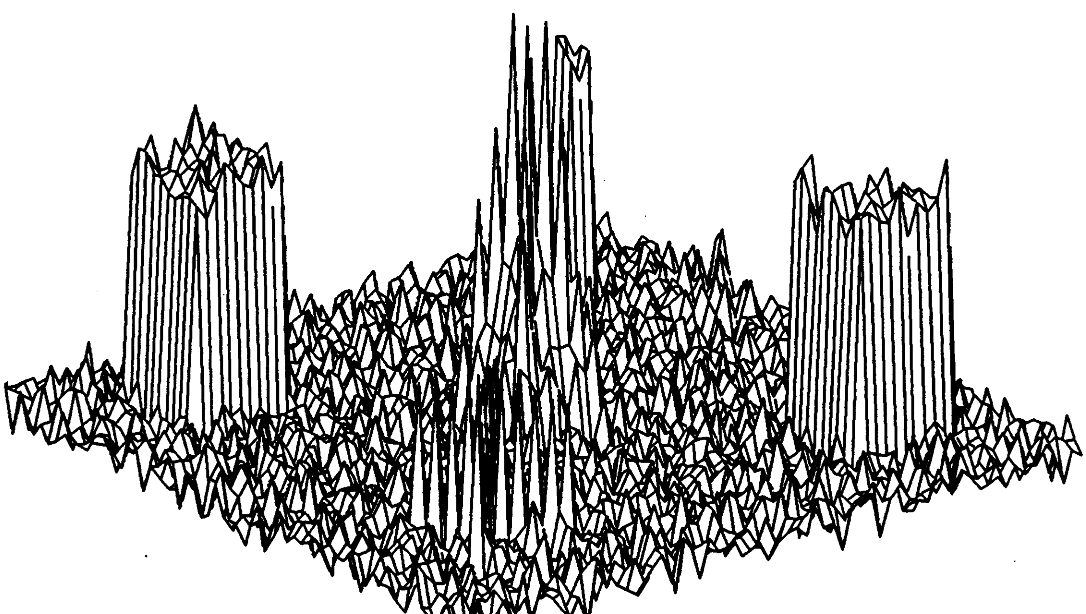

Figure 2.4 Test image with normally distributed random noise added.

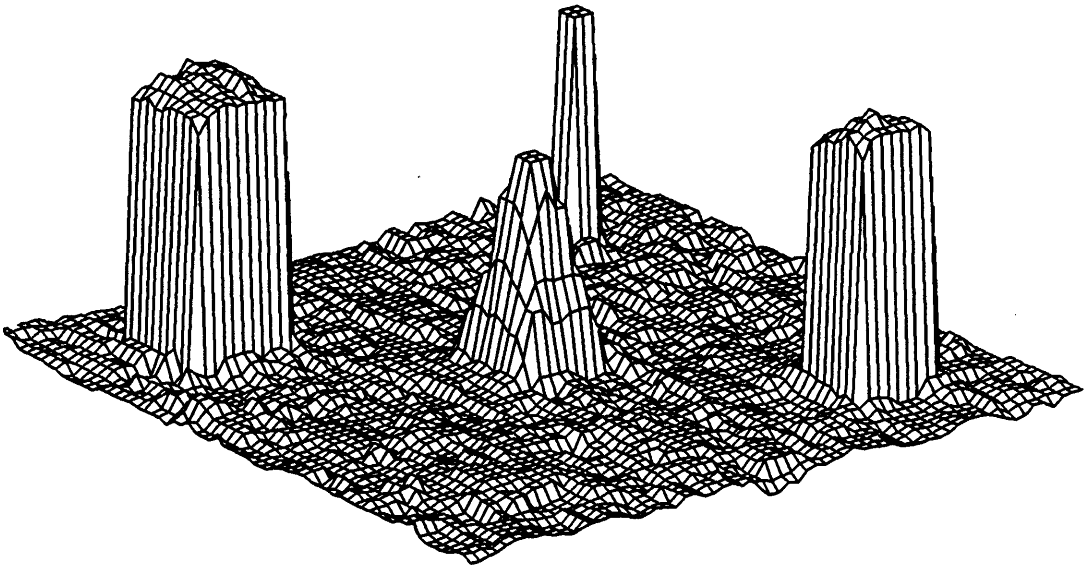

Figure 2.5 Output after two-pass or separable 5x5 median filter.

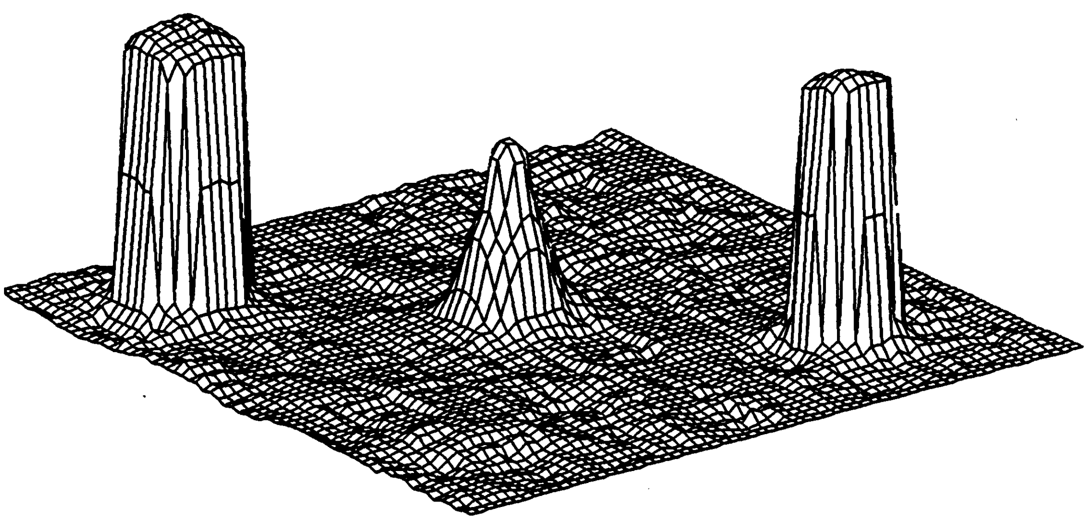

Figure 2.6 Output after one-pass of the square 5x5 median filter.

2.2.3 The weighted median filter

If it is desirable to bias the output of a filter by some series of coefficients, the weighted median concept can be used. This is done by repeating data values by the absolute value of the weighting coefficients, sorting this data series, and selecting the middle value. Stewart (1985) applied this technique to a normal moveout corrected shot gather and used the time-domain coefficients of an *f-k* fan filter as the weights. This enables dip rejection and/or enhancement coupled with the desired properties of the median filter (spike rejection, edge preservation). A post-stack application of the weighted median filter to a 3-D volume was demonstrated by Stewart and Schieck (1993). The analytical difference between a 2-D and full 3-D time-domain operator is shown in appendix A.

In simple median filters all data values within the window have the same influence on the resulting output, analogous to an equally-weighted running average filter. We can define the weighted median function as:

$$x_w: \qquad \min \sum_i |w_i|\,|x_w - x_i| \tag{2.8}$$

where x_w is the weighted median value (Claerbout and Muir, 1973). This reduces to the previous definition if all of the weighting factors are equal to 1. Including a weight of 2, for example, means duplicating the same data value twice before selecting the middle value. Also note that the output median value is always equal to an actual input data value even if the weights are not integers. Based on the above definitions, negative weights are not included in this estimation process. Stewart and Schieck (1993) demonstrate how the negative filter coefficients (band-pass, *f-k*) commonly used in digital signal processing can be applied using the weighted median definitions. The data values are multiplied by the sign of the associated filter coefficients and weighted according to the absolute values of the filter coefficients:

$$x_w: \qquad \min \sum_i |f_i|\,|sgn(f_i)x_i - x_w| \ . \tag{2.9}$$

Again this function is minimized by setting its partial derivative equal to zero, giving:

$$\sum_{i=1}^{N} |f_i \,|\frac{\partial}{\partial x_w}|\; sgn(f_i)x_i - x_w| = 0 \tag{2.10}$$

$$\sum_{i=1}^{N} |f_i|\frac{\partial}{\partial x_w} sgn(\gamma_i)\gamma_i = \sum_{i=1}^{N} |f_i| sgn\gamma_i,$$

$$with \quad \frac{\partial sgn\gamma_i}{\partial x_w} = 0, \quad where \quad \gamma_i = sgn(f_i) * x_i - x_w \,,$$

$$\sum_{i=1}^{N} |f_i| [sgn(f_i)x_i - x_w] = 0. \tag{2.11}$$

When applying the weighted median process with negative coefficients f_i the data values are multiplied by the polarity of the coefficients and augmented by the absolute values of these weights. This augmented array is then sorted and the data value which corresponds to half the sum of the weights is selected. Note also from eq. (2.11) that the output value, although corresponding to an input value of the augmented array, could actually be reversed in polarity. This is analogous to a mean process in which the data values are multiplied by the filter coefficients and summed to obtain an output value. This method of application also lends solution to fractional coefficients in the augmented array because the median data value is selected when the sum of the filter weights is greater than or equal to half their total.

Consider the filter weights $f_i = (-2.5, 1.5, 1, 3)$ applied to the series of data values x_i = (-1, 3, 1000, -2, 1, 4, 3,...). At the first sample location, the absolute values of the filter weights are attached to the data and the first sample is reversed in polarity as follows:

$$x_i = 1, \; 3, 1000, -2$$
$$f_i = 2.5, 1.5, \; 1, \; 3;$$

then the data are sorted in pairs carrying the attached filter weights:

$$x_i = -2, \; 1, \; 3, 1000$$
$$f_i = 3, 2.5, 1.5, \; 1$$

The total sum of the filter coefficients is 8 so the middle value occurs where the sum of the weights equals 4 or $x_w = 1$. The resulting weighted median output series would then be x_{w+2} = (1, 1, -2, 2,...). This would be the result whether or not

x_3 were 10, 100, 1000, 10,000, or -10,000. Similarly, the equivalent mean processed is applied by multiplying the weights by their corresponding data values and summing at successive indices. The mean process yields the output sequence x_{w+2} = (125.13, 186.69, -311.25, 2.44,...).

In this example, the mean is biased by the single large data sample x = 1000 yet the median is not affected. In a sample size N, for a simple mean, each sample is given a weight N^{-1} in the averaging process. By manipulating the Nth data point the sample mean can assume any arbitrary value. In the case of the weighted mean this can be expressed as:

$$x_{mean} = \frac{1}{\sum_{i=1}^{N} w_i} \left[\sum_{i=1}^{N-1} w_i x_i + (w_N x_N) \right] \tag{2.12}$$

If x_N is an erroneous data point, it will tend to bias the mean so that the mean will not represent the main body of the data. To minimize this problem an estimator which incorporates some degree of data editing, in which aberrant data values are given little or no weight (w_N=0) in the averaging, is required. Rather than averaging the entire data set, a few inconsistent data points are removed or trimmed before averaging. This is known as the weighted α-trimmed mean (α>0), or, in the limit of trimming all data values except the middle value, the weighted median (α=0.5). Mathematically, this can be represented as:

$$x_\alpha = \frac{\sum_{i=1+\alpha(N-1)}^{N-\alpha(N-1)} w_i x_i}{\sum_{i=1+\alpha(N-1)}^{N-\alpha(N-1)} w_i} , \tag{2.13}$$

where x_i are ordered.

This filter is part of a general class of non-linear, data-dependent, order statistical filter commonly used in digital image filtering, edge detection, and data communications filtering (Bovik *et al*,1983; Pitas and Venetsanopoulos, 1986; and Longbotham and Bovik, 1989). This general class of order-statistic filters involves sorting an input data array and statistically filtering to create a new output data array.

2.3 Algorithm design

Although the advantages of the weighted α-trim filter are clear, the application of this computationally intensive filter can be limited by long computer run times, rendering it impractical for routine data processing. It must be demonstrated that a computationally efficient algorithm can significantly minimize this apparent disadvantage.

2.3.1 Sorting

The applications of order statistic filters are limited by the efficiency of the sorting algorithms used. Poor sorting algorithms can result in 1000-fold increase in computing time (Wirth, 1986). Sorting algorithms considered include Bubblesort, Straight Insertion, Heapsort, and Quicksort; the last two algorithms being easily available in the C language, (Press, 1986).

Bubblesort involves multiple passes of the data, simply comparing adjacent data values within a string and swapping them into sorted order until nothing changes in a complete pass. This is definitely the worst sorting algorithm except in the extreme case of an already sorted array. Straight insertion requires a second data string which is built by comparing new values to the already inserted values, and shifting these down if required to accommodate values in between. This is an n^2 operation but very simple to program, and may be considered for small data strings. Heapsort and Quicksort are essentially logarithmic methods (i.e. require $nlog(n)$ operations). Of these two methods, for strings greater than $n=256$, Quicksort is reportedly faster than Heapsort by a factor of 2 to 3 (Wirth, 1986).

A version of Quicksort was used in this study. This was further optimized by sorting on half-word values, thus reducing the machine language moves and comparisons to only 16-bit operations. This was achieved by scaling the dynamic range of the input values to within the necessary -32767 to 32767 range before sorting. Full accuracy was maintained because after sorting only the index was used to recover a full floating point median value from the actual input array. If two numbers are equal within the half-word dynamic range after scaling, but out of order when considering their full value, it was assumed that the sorting error was negligible.

2.3.2 The fast 2-D weighted-median algorithm

The computational time for a mean process is proportional to n, the number of points at each spatial application of the operator. However, the sorting algorithm used here is logarithmic (ie. proportional to $nlog(n)$). For example, a 2-D operator using 13 seismic traces by 15 time samples, or 195 data points, requires roughly five times the computational effort for a weighted median process relative to the mean. Sorting algorithms can be significantly improved by a factor of two to three if the data are partially sorted (Wirth,1986). In this way, the computational effort can be reduced to $3n$, suggesting that the *f-k* weighted median as applied in this paper could take only 3 times more time than the more conventional mean *f-k* filters commonly used in seismic processing.

Gurwitz (1990) reports on his experience with weighted-median algorithms used to solve L_1 norm approximations. He makes an empirical comparison between partial Heapsort and Quicksort methods as previously described as well as a third linear-time method. Linear-time methods involve dividing the given data string into small strips of 5 elements each, and creating a new string made up of the medians of these data strips and their associated weights. Gurwitz observes that the partial Quicksort methods for sufficiently large data windows (ie. $n > 100$) are substantially better than both of the other methods.

Huang *et al* (1979) developed a fast 2-D median filtering algorithm which takes advantage the overlap of an *mxn* window which moves by one column for each output data point. By replacing the previous n points and inserting in their place n new numbers while leaving the sorted matrix of $mn-2n$ numbers unchanged, a very significant time improvement was observed.

One method of supplying a partially sorted array to the sorting algorithm is to use the sorted 2-D data box of the previous time sample and replace only the new locations with the data values at the current time location (Huang *et al.*, 1979, and Bednar and Watt, 1984). Two additional considerations must be addressed to use this roll-along method (Figure 2.7). First, the data values that were previously reversed due to negative filter coefficients that are now positive (or vice versa) must be flipped in polarity before sorting. Second, all of the filter coefficients previously attached to the data must also be moved down in time. This is easily achieved by

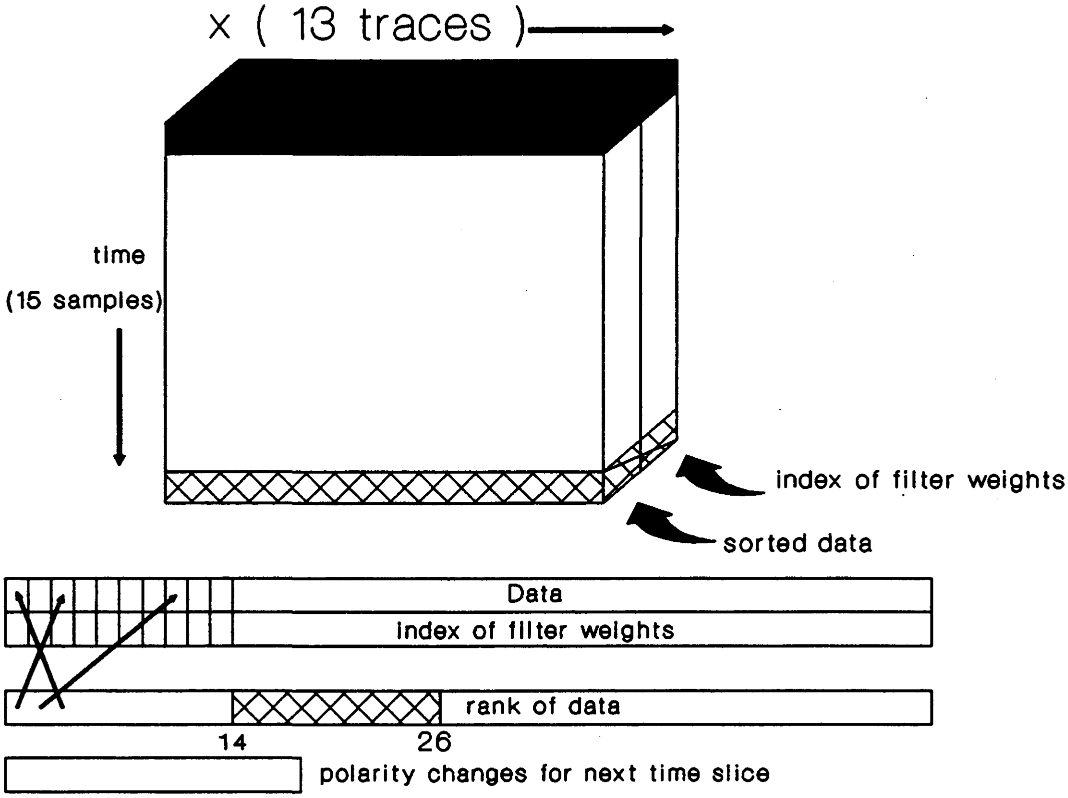

Figure 2.7 Weighted median algorithm design procedure showing the required computer arrays; data, attached filter weight indexes, rank of data and polarity change indexes.

attaching only the address of the filter coefficients and decrementing this address by the spatial width of the 2-D operator (ie. 15 samples x 13 traces). The rank of the sorted array will indicate where within the sorted data array each index of the original 2-D data matrix is actually located, thus enabling direct replacement of the oldest time strip with the new data values into the previously sorted array.

2.4 *f-k* dip filter coefficients as median weights

By using the time-domain coefficients of an *f-k* fan or pie-slice filter as weights the weighted α-trim mean filter can reject user specified dips. The time-domain coefficients are obtained by inverse Fourier transforming the desired fan filter from the frequency domain to the time domain. Multiplication in the frequency domain corresponds to convolution in the time domain. This operator can be applied in time by overlaying the coefficients on a data window, then multiplying and adding to replace the value in the centre of the window with this new value (Yilmaz, 1987). In practical terms, convolution is computationally more intensive than multiplication in the frequency domain, and hence, the latter is preferred in the case of conventional *f-k* filtering. However, processes such as the α-trim cannot be applied in the frequency domain in order to obtain a corresponding operation in the time domain.

2.4.1 Operator generation

The *f-k* fan or velocity filter is depicted in Figure 2.8 and defined in the frequency domain as:

$$F(f,k) = \begin{cases} 1 & \frac{-|f|}{v} < k < \frac{|f|}{v},\ |f| < f_N \\ 0 & otherwise \end{cases} \tag{2.14}$$

The impulse response is given by the 2-D inverse Fourier transform of $F(f,k)$:

$$f(t,x)=\frac{1}{2\pi}\int_{-\infty}^{\infty}\int F(f,k)e^{2\pi i(ft-kx)}dkdf \tag{2.15}$$

and from eq. (2.14),

$$f(t,x)=\frac{1}{2\pi}\int_{-f_N}^{0}\int_{-\frac{f}{v}}^{\frac{f}{v}} e^{2\pi i(ft-kx)}\ dkdf + \int_{0}^{f_N}\int_{\frac{f}{v}}^{-\frac{f}{v}} e^{2\pi i(ft-kx)}\ dkdf. \tag{2.16}$$

The transfer function is symmetric with respect to the origin, and hence this simplifies to:

$$f(t,x)=\frac{1}{\pi}\int_{0}^{f_N}cos2\pi ft\int_{-\frac{f}{v}}^{\frac{f}{v}}e^{-i2\pi kx}\ dkdf \tag{2.17}$$

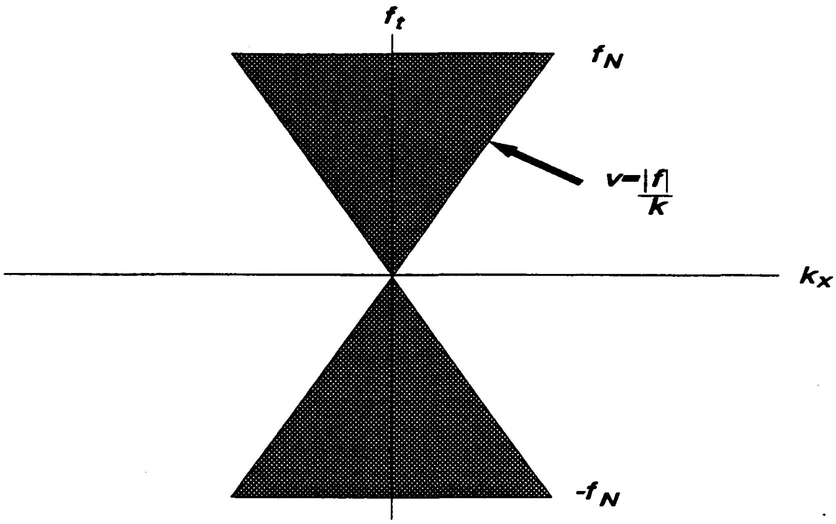

Figure 2.8 f-k domain velocity filter

The inner integrand can be simplified using trigonometric identities as:

$$\int_{-\frac{f}{v}}^{\frac{f}{v}} e^{-2\pi ikx}dk = \frac{1}{-2\pi ix}\int_{-\frac{f}{v}}^{\frac{f}{v}} -2\pi ixe^{-2\pi ikx}dk$$
$$\frac{e^{2\pi i\frac{f}{v}x} - e^{-2\pi i\frac{f}{v}x}}{2\pi ix} = \frac{\sin(2\pi\frac{f}{v}x)}{\pi x} \tag{2.18}$$

Eq. (2.16) can now be written as:

$$f(t,\, x) = \frac{1}{\pi^2 x}\int_0^{f_N} \sin(2\pi\frac{f}{v}x)\,\cos(2\pi ft)\; df. \tag{2.19}$$

From the CRC standard math tables (Beyer, 1982), integral equation 319:

$$\int \sin(mx)\,\cos(nx)dx = -\frac{\cos(m-n)x}{2(m-n)} - \frac{\cos(m+n)x}{2(m+n)}. \tag{2.20}$$

Substituting (2.20) in the integrand of Eq. (2.18) and making use of basic trigonometric identities, the final result is:

$$f(t,\,x) = \frac{x}{4v\pi^3}\left(\frac{\sin^2[2\pi f_N(\frac{x}{v}-t)]}{\frac{x}{v}-t} + \frac{\sin^2[2\pi f_N(\frac{x}{v}+t)]}{\frac{x}{v}+t}\right) \tag{2.21}$$

This impulse response is spatially and temporally symmetric and has a zero phase shift. An example of this operator is depicted in Figure 2.9 for a $\pm$ 4 ms/trace limit in the velocity transformed from the *f-k* domain.

2.4.1.1 Tapering and smoothing

Analogous to the spectral representation of a 1-D filter, poor tapering between the pass and reject zones in the *f-k* domain introduces artifacts at dips corresponding to these dip edges. However, large tapers in frequency and wavenumber will reduce the ability to discriminate between pass and reject dips of the filtered data. Tapering the dip edges in the frequency domain will also collapse the time-domain impulse response of the operator. This is desirable because the time domain response will be truncated to a finite size (ie. 13 traces X 15 samples) to minimize the computational time of the order statistic process. Figure 2.10 is the result of taper by a factor of 30% of the Nyquist frequencies and wavenumbers in the *f-k* domain of the filter response in Figure 2.9. The box in Figure 2.10 represents truncation of this operator modified for processing the synthetics of section 2.4.2.

2.4.1.2 Size considerations

The spatial and temporal size of the operator truncation box (Figure 2.10) depends on the dip cut-off desired. A large operator can prohibitively increase the computational time but provide a more regular transfer function in the case of the weighted median. The transfer function for the median filter approximates the equivalent linear filter below $2\pi/n$ where n is the operator size. Therefore a trade-off in regular transfer function verses computational efficiency must be made. The 13-trace by 15-sample operator used in this thesis contained the larger-valued coefficients but maintained a regular transfer function and practical computer run times.

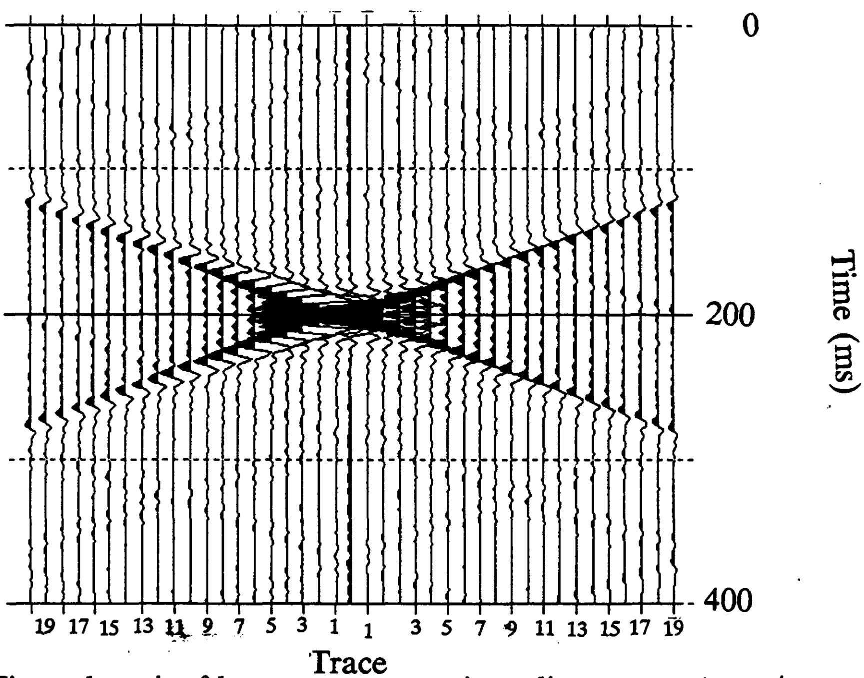

Figure 2.9 Time domain f-k operator to reject dips > $\pm$ 4 ms/trace with no smoothing applied in the frequency domain.

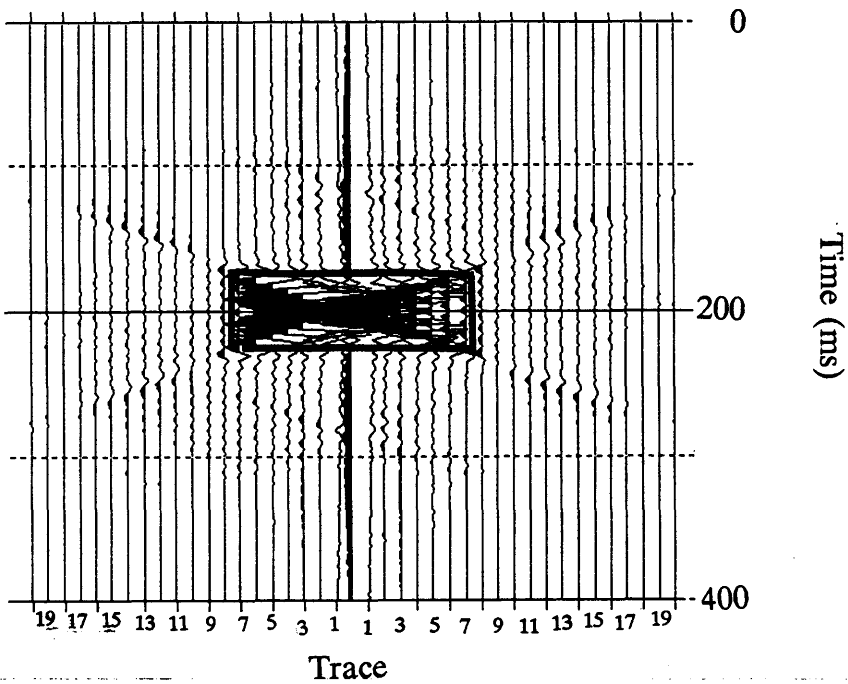

Figure 2.10 Time domain f-k operator to reject dips > $\pm$ 4 ms/trace with dip reject smoothing applied at 30% of Nyquist value in both frequency and wavenumber. The box defines the truncated operator used for this study.

2.4.2 Application to synthetic data

To test the aliased dip-reject characteristics, random noise reduction, automatic trace editing, and the de-glitching aspects of the various *f-k* filters, a synthetic shot gather was generated (Fig. 2.11).

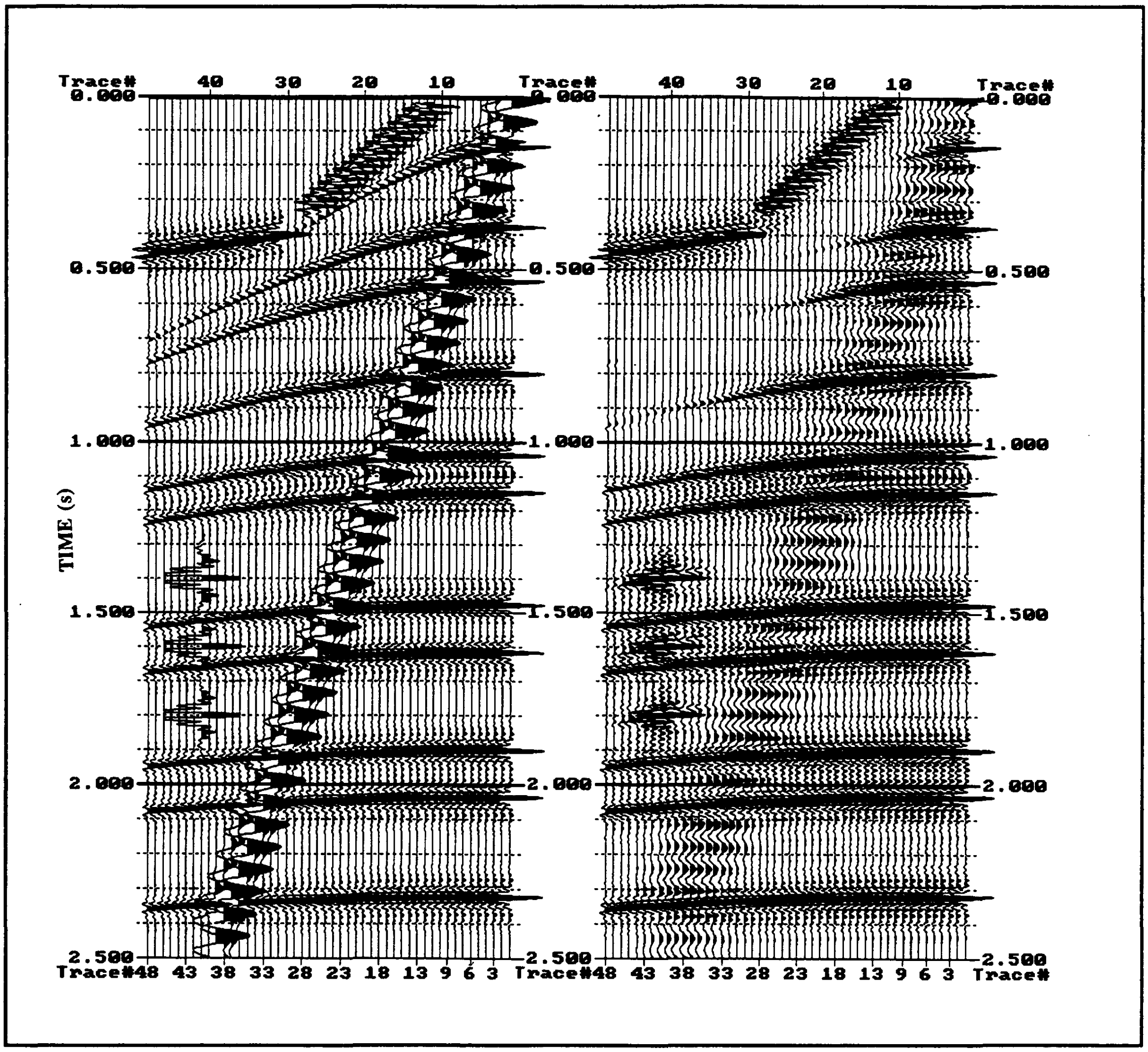

Figure 2.11 Synthetic shot gather using the Jumping Pound model a) input data b) after f-k filtering to reject dips > $\pm$ 4 ms/trace (velocities < 7500 m/s).

The synthetic gather consists of 11 primary hyperbolic events derived from a velocity function representative of Springbank, Alberta, band-limited to 10-70 Hz. Each record consists of 48 traces with a trace spacing of 30 m. in order to relate to the real data example shown in the next section. Two aliased dipping events which might be representative of non-dispersive ground roll (8-15 Hz, 70 ms/trace or 428 m/s) and a near-surface multiple refraction (14-70 Hz, 16 ms/trace or 1875 m/s) are inserted in the synthetic data set. The two dipping events are spatially aliased as seen in the *f-k* transform plot (Figure 2.12) both events wrap around to negative dips as previously discussed in chapter 1. Three noise glitches representative of tape errors are located on trace 43 at times 1.4, 1.5 and 1.6 seconds.

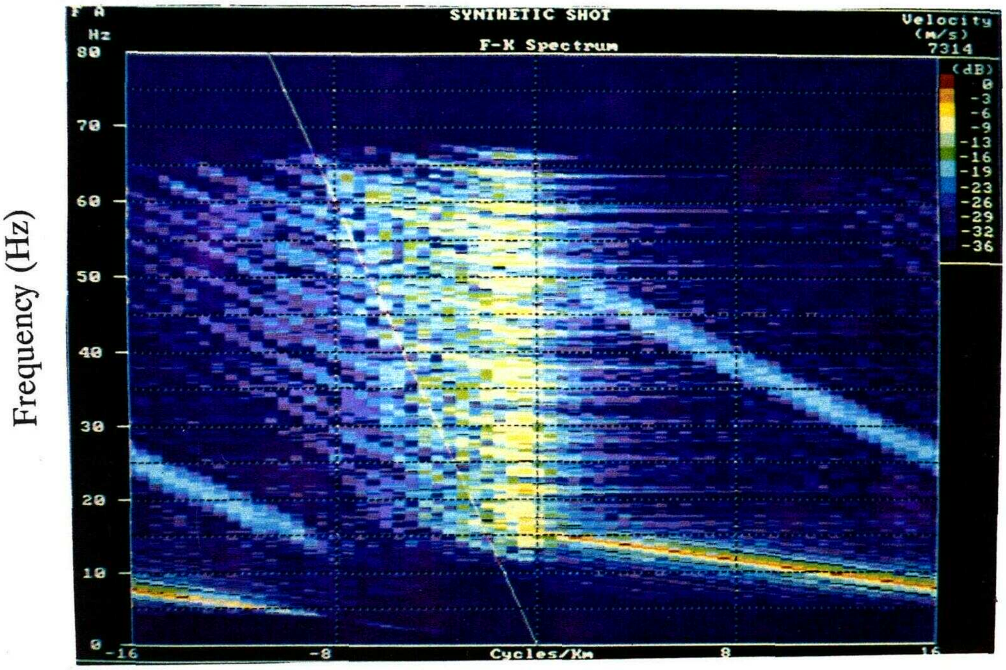

Figure 2.12 f-k transform of synthetic shot gather in figure 2.11 a).

The synthetic gather was *f-k* filtered with a dip reject of $\pm$ 4 ms/trace (Fig. 2.11 b). The glitches were not removed but remain as the time-domain operator of the *f-k* filter. The higher frequency, 16 ms/trace aliased dip, appears as a negatively dipping event in the band 50 to 70 Hz. The low-frequency ground roll, which has negative dips within the passband of this filter, also remains as a negatively dipping event with a bandwidth of 10 to 20 Hz. The primary events below 1.0 second are virtually identical to the input shot gather in Figure 2.11 a).

Random noise, band limited to 15-70 Hz, was added to the gather with an RMS magnitude 1/3 that of the primary events (see Fig. 2.13 a). Trace 11 in Figure 2.13 a) is a high-amplitude noise trace representative of a bad trace within the shot gather. Figure 2.13 b) is the output after application of the $\pm$ 4 ms/trace *f-k* filter as

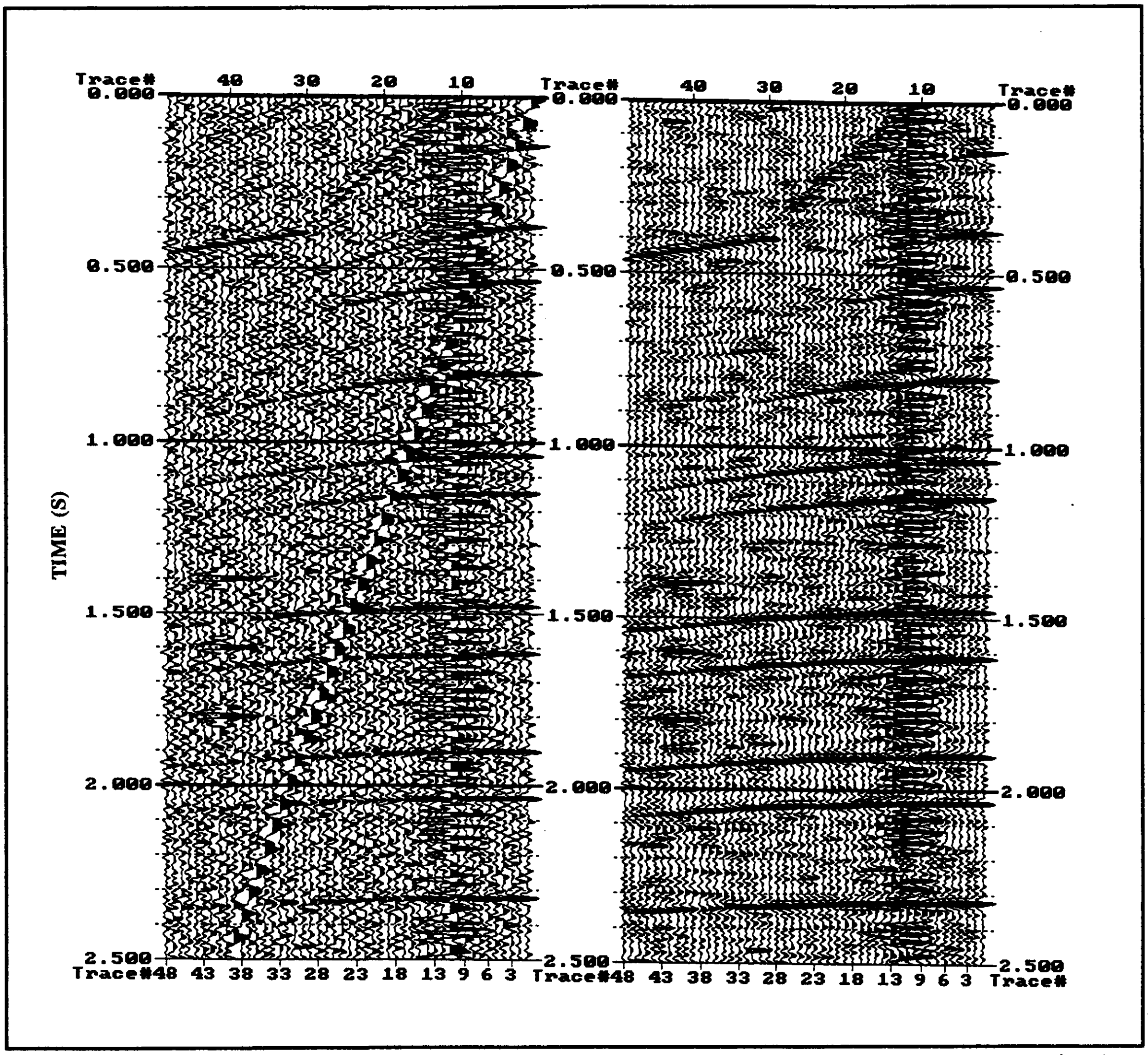

Figure 2.13 Synthetic shot gather a) with random noise and bad trace added, b) after f-k dip-reject filter of $\pm$ 4 ms/trace.

in Figure 2.11 b). Random noise is reduced only by the smear of the time-domain operator and still remains within the passband of the spatial filter. Figure 2.14 a) is the result of applying the same spatial operator. However, in this case the operator was truncated to a 13-trace by 15-sample 2-D matrix and applied as a weighted median process. The aliased dips are completely removed. However, the amplitudes of the primary events are reduced by a factor of $19/20^{th}$ of the original synthetic. This is due to the clipping of peaks and troughs often observed with the application of median or other data-dependent filtering (Green, 1986). In fact, any value that is a maximum or a minimum can never be a median value. Random noise is not smeared

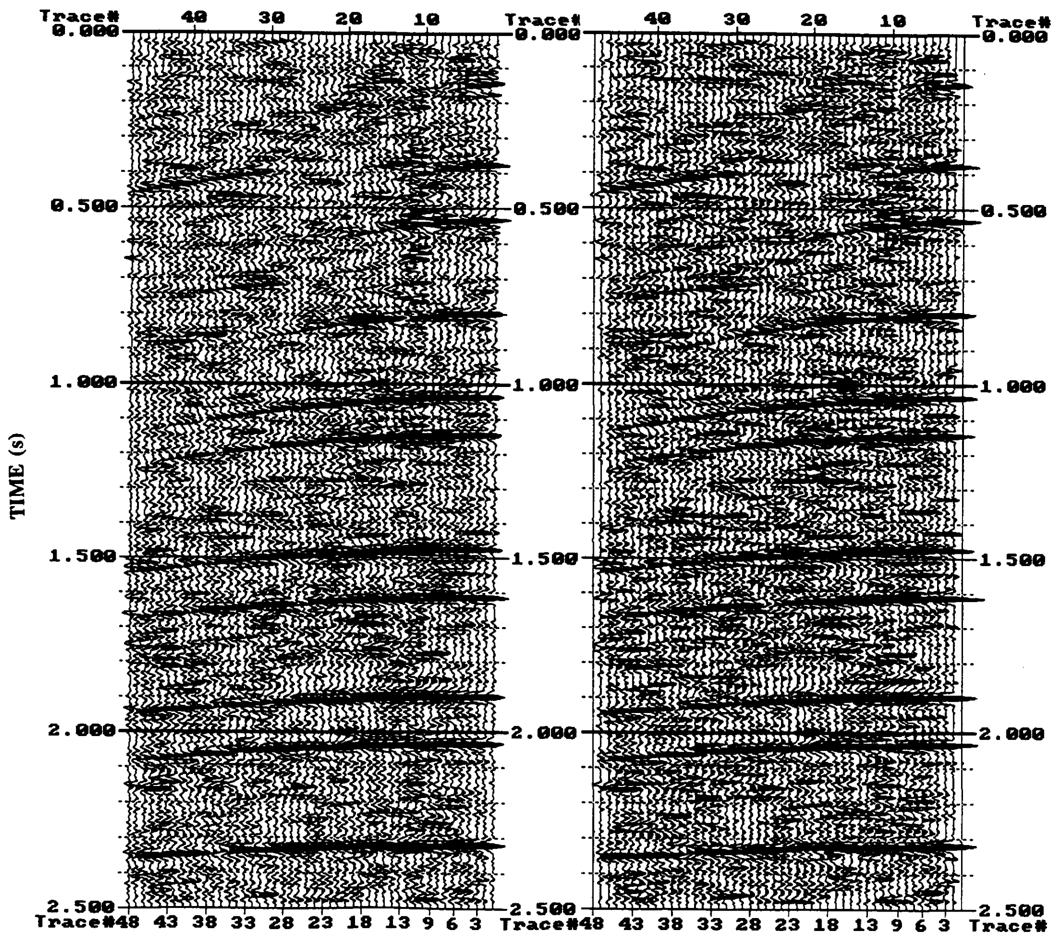

Figure 2.14 Synthetic shot gather with random noise and bad trace added a) after weighted median *f-k* dip-reject filter of ± 4 ms/trace; b) after weighted α-trim filter ($\alpha=0.25$) of Figure 2.13 a).

as can be observed by the rejection of the larger amplitude noise glitches (Fig. 2.14). The bad trace has been almost completely removed and not smeared as in figure 2.13b). Figure 2.14 b) is the mean of the weighted, sorted data values after rejecting the top and bottom half of the sorted data within the filter box. Figure 2.15 is the *f-k* transform of synthetic shot gather (Figure 2.13a) with random noise added. Figure 2.16 is the same *f-k* transform after application of the *f-k* dip reject filter. Figure 2.16 is the *f-k* transform of the synthetic shot gather after application of the weighted median filter.

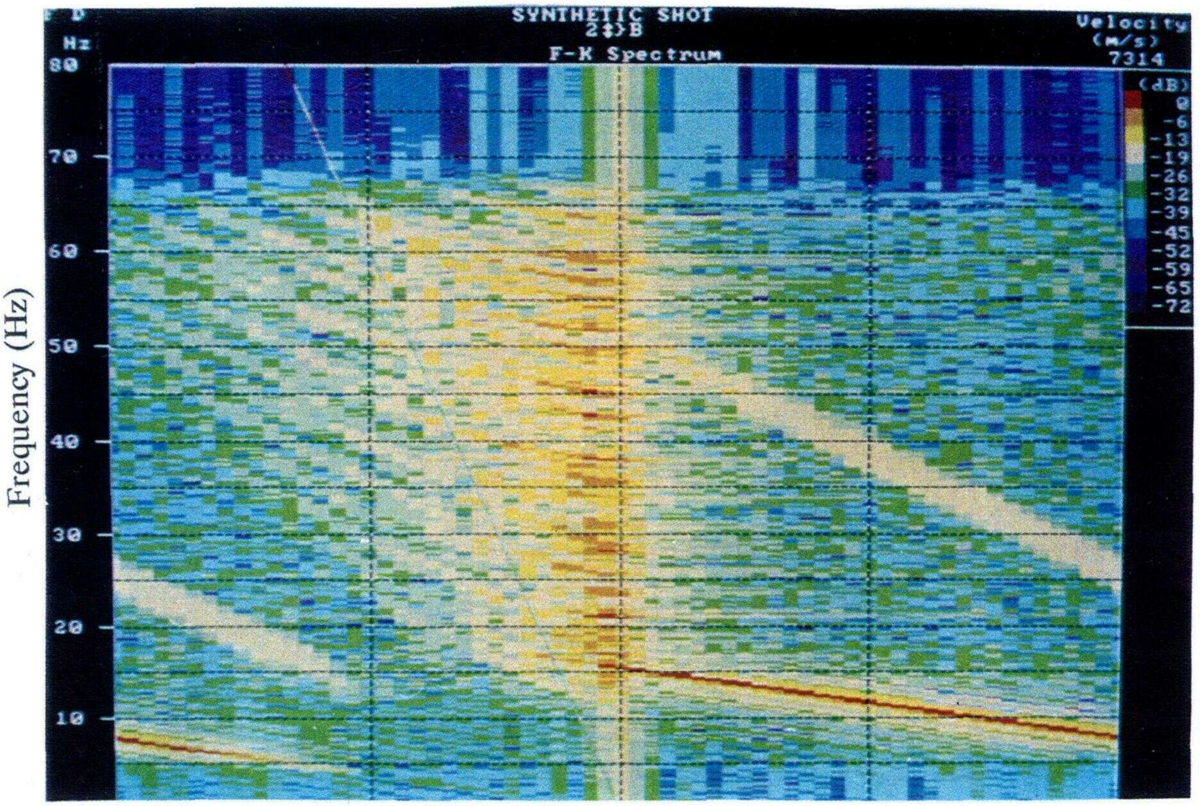

Figure 2.15 f-k transform of synthetic shot gather with random noise added (f-k of Figure 2.13 a)).

In order to quantitatively estimate the reduction in random noise and degree of auto editing of trace 11, the outputs of the α-trim filter were cross-correlated with the original signal-only synthetics. The cross-power spectrum, computed as the Fourier transform of the result of cross-correlation, was divided by the cross-power spectrum of the noise-only synthetics after application of their respective α-trim filters. An average amplitude of the cross-power spectra was picked and the results are shown in Figure 2.18 for the relative S/N cross-power spectrum versus various α-trim values.

Generally speaking, the S/N improvement of random noise is better for the mean filter($\alpha = 0$) than for the median ($\alpha = 0.5$) but the bad trace edit for the median is superior to that of the mean. A summary of the characteristics of these two extreme values of the weighted α-trim mean filter is shown in Table 2.1.

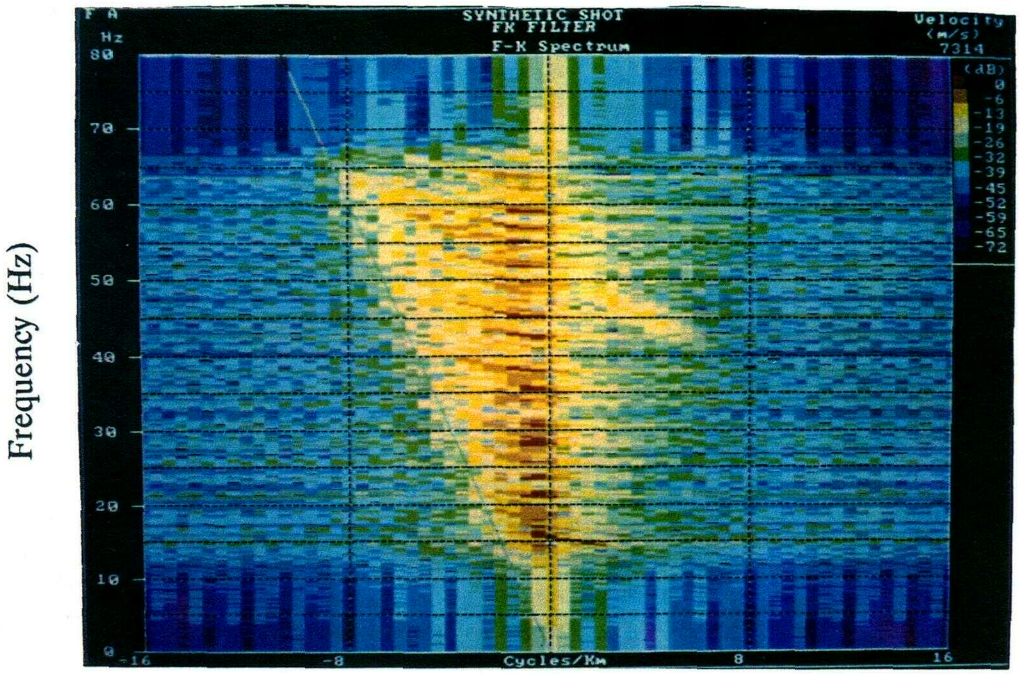

Figure 2.16 f-k transform of synthetic shot gather with random noise added after f-k filtering (f-k of Figure 2.13 b)).

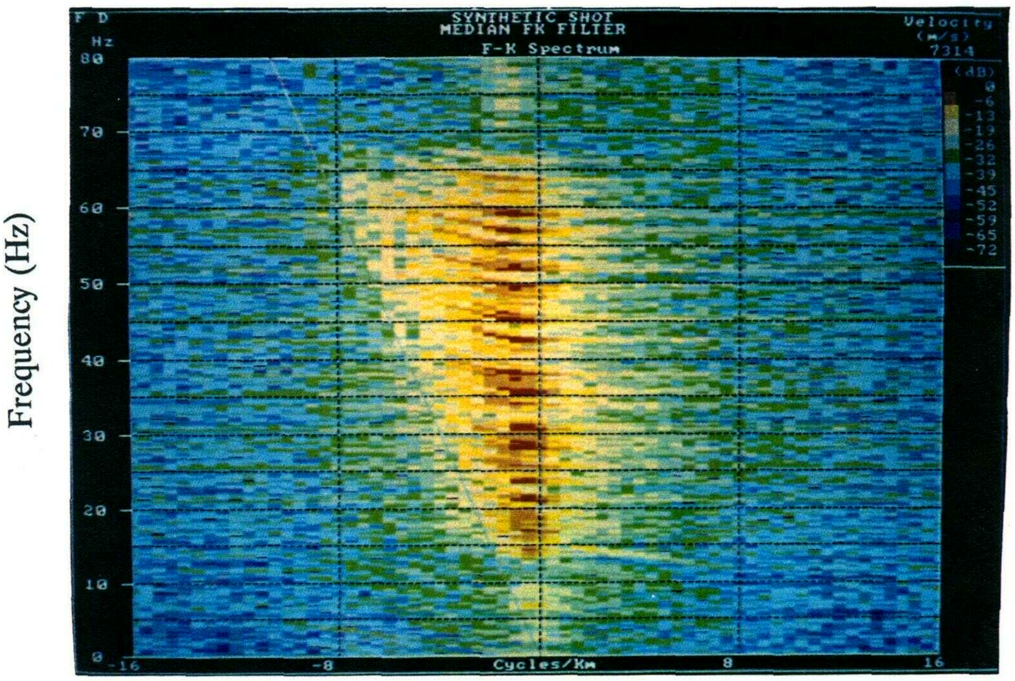

Figure 2.17 f-k transform of synthetic shot gather with random noise added after median f-k filtering (f-k of figure 2.14 a)).

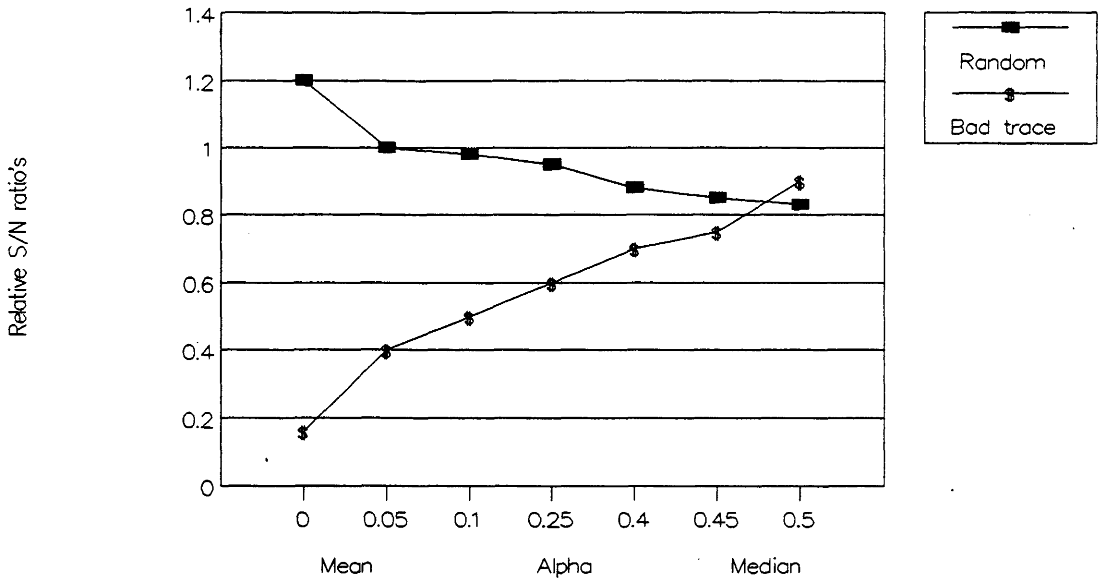

Figure 2.18 S/N ratios for α-trimmed mean filter of synthetic shot gather.

	MEAN (α=0.0)	MEDIAN (α=0.5)
Performance	linear	non-linear, data dependent
Random noise	reduced*	somewhat reduced
Spatially aliased noise	smeared	removed*
Noise spikes	smeared	removed*
Bad trace edits	smeared	removed*
Transfer function	smooth*	irregular

Table 2.1 Summary of the characteristics of the weighted α-trim mean filter.

* Note: These characteristics are generally accepted as what is desirable in most seismic data processing applications. A compromise in output attributes must be made when choosing the value of α. For example, if random noise outside the bandwidth of the signal is to be reduced, a value of $\alpha=0$ might be optimal.

2.4.3 Springbank example

A real data example is applied to P-SV data (Line FS90-1) acquired by the University of Calgary field school in August 1990 from Springbank, Alberta (Twp 25, Rge 3W5). A P-SV shot gather is displayed in Figure 2.19 a) after spherical divergence, low-pass filtering (60 Hz, rolled off at -72 dB/octave) and RMS trace scaling. The trace interval is 30 m.

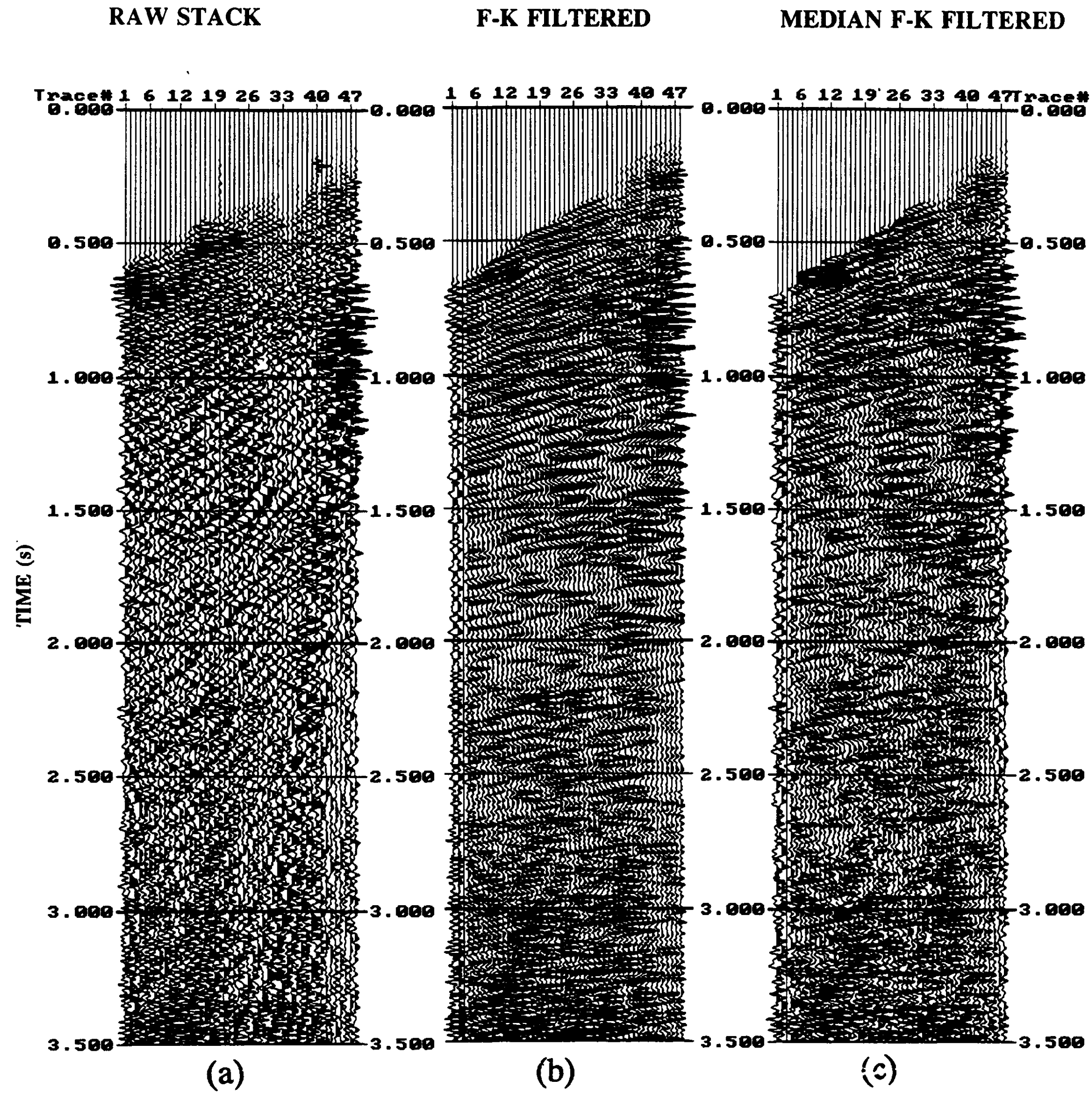

Figure 2.19 Shot point 168 a) raw unfiltered b) *f-k* filtered (reject > ± 4 ms/trace) c) median *f-k* filter (reject > $\pm$ 4ms/trace).

Three types of noise can be recognized on the input shot gather: noise glitches caused by dead traces (traces 20 & 40), ground roll with a velocity of 200 m/s, and near-surface refracted reverberations with a velocity of 1470 m/s. The spatial filters were applied after corrections for initial statics and velocities were made. Dips greater than ± 4 ms/trace dips were rejected in Figure 2.19 b) and c).

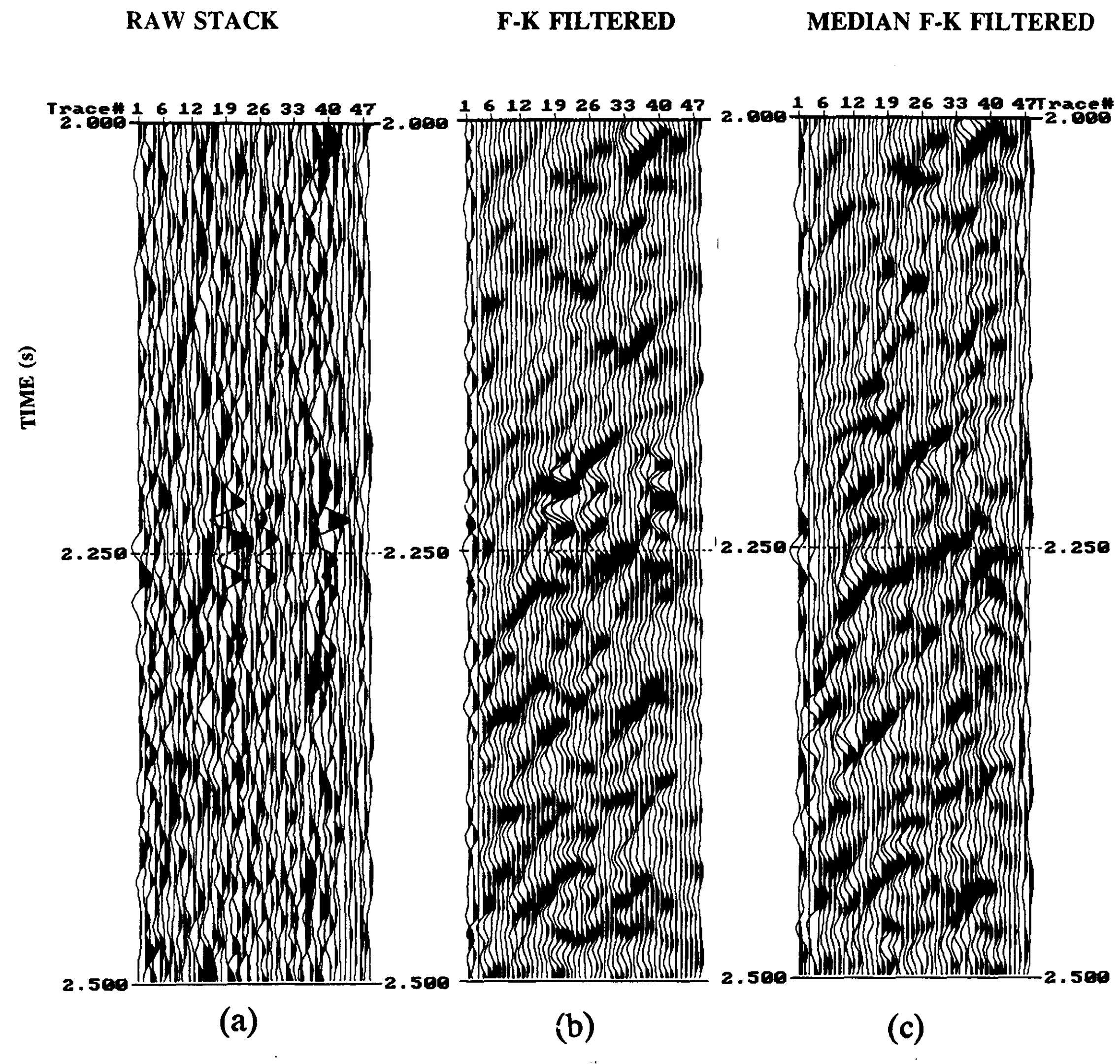

Figure 2.20 Shot point 168 of figure 2.17 with exaggerated vertical scale a) raw gather b)f-k filtered shot c) median f-k filtered shot.

The frequency edges in the *f-k* domain were tapered with a 2-D moving average filter with a size of 30% of the Nyquist frequency (5 by 150 point window smoother). The time-domain operation requires a taper to be applied to the edges of each shot gather as the 13-trace 2-D matrix of filter coefficients rolls on and off the data. This was achieved by adding back 100% of the original trace when the 2-D box was centred at the first trace, with the additional part gradually reduced to 0% when the data box was completely filled. The weighted median process for all 62 shot gathers was completed in the cpu (ie. without the array processor commonly used for conventional *f-k* filters) on an IBM 3081 with a virtual time of 6 hours and the conventional *f-k* was processed with the use of an FPS-190L array processor in only 30 minutes.

Figure 2.19 b) demonstrates the smear of an *f-k* filter. The noise glitches indicative of a bad trace on traces 20 and 40 (offsets 600 m and 1200 m respectively) are spread over approximately 5 traces. The limited smearing is due to the smoothing of the frequency domain cut-offs, which tends to limit the spatial size of the time-domain operator. The *f-k* weighted median filter shows similar dip-reject capabilities but completely edits the bad traces (Figure 2.19 c)). Shown exaggerated in Figure 2.20 is an aliased surface wave dipping from trace 18 (2.00 s) to 1 (2.35 s). The *f-k* filtered result leaves residual negative dips where the noise wraps around to the pass range of the filter (refer section 1.2.2 or 2.4.4). However, the median *f-k* filter completely removes this aliased dipping event as demonstrated in Figure 2.20 c).

The data were further processed, after each pre-stack filter application, using the parameters and sequence outlined in Table 2.2. The two-window deconvolution process was performed before applying these pre-stack filters because divide-by-zero errors occurred in the array processors as a result of the data-dependent editing by the median *f-k* filter.

Each data set was processed with the final statics and velocities obtained from the unfiltered data set to maintain consistency. Only the residual trim statics between stacks might be different due to the correlation models dissimilarities after differing pre-stack filters. Figure 2.21 shows a sample common offset stack between shot point numbers 145 and 152. The *f-k* weighted median filter (Figure 2.21 c) demonstrates dip-rejection characteristics similar to those of the *f-k* filter (Figure 2.21 b), yet there is less noise smearing. Primary events after the median process are better imaged after the mean *f-k* application (ie. at the time of 1.5 s.) particularly on the near offsets. The final P-SV common-depth-point (CDP) stacks are displayed in Figures 2.22 to 2.26. Generally, the median processed data improve the signal-to-noise ratio by removing noise glitches and attenuating aliased noise consistently. This process

DEMULTIPLEX
GEOMETRIC SPREADING COMPENSATION
    $1.0 * e^{0.0007\,t}$
[OPTIONAL PRE-STACK FILTER]
SPIKING DECONVOLUTION
    2 windows, 120 ms operator 1.0% prewhitening
REVERSE POLARITY OF TRAILING SPREADS
TRACE EQUILIZATION
APPLY FINAL P-WAVE SOURCE STATICS
INITIAL VELOCITIES
APPLY HAND STATICS FROM COMMON RECEIVER PLOTS
AUTOMATIC SURFACE CONSISTENT STATICS
    Correlation window from 800 to 3200 ms
    Maximum shift of + or - 36 ms
CDP STACK
CONVERTED-WAVE REBINNING
    Vp/Vs ratio of 2.08 independent of depth
VELOCITY ANALYSIS
NORMAL MOVEOUT
FIRST BREAK MUTE
    distance 525 m, time 550 ms
    distance 2880 m, time 1980 ms
TRACE SCALING
    Mean amplitude of 2000
    Windows 0-800, 600-1600, 1400-3400 ms
CDP TRIM STATICS
    Correlation window from 200-3200 ms
    Maximum shifts + or - 20 ms
STACK
    offsets 30-2400 m
BANDPASS FILTER
    Zero-phase, 8-38 Hz
RMS GAIN
    Mean amplitude of 2000
    Window 400-3200 ms

Table 2.2 Processing sequence and parameters for the Springbank, P-Sv data.

does not leave the impression of a mixed or smeared section as in the case of the mean *f-k* filter, but honours the overall character of the original un-filtered section.

The spatial filters were applied also as a post-stack process to the section in

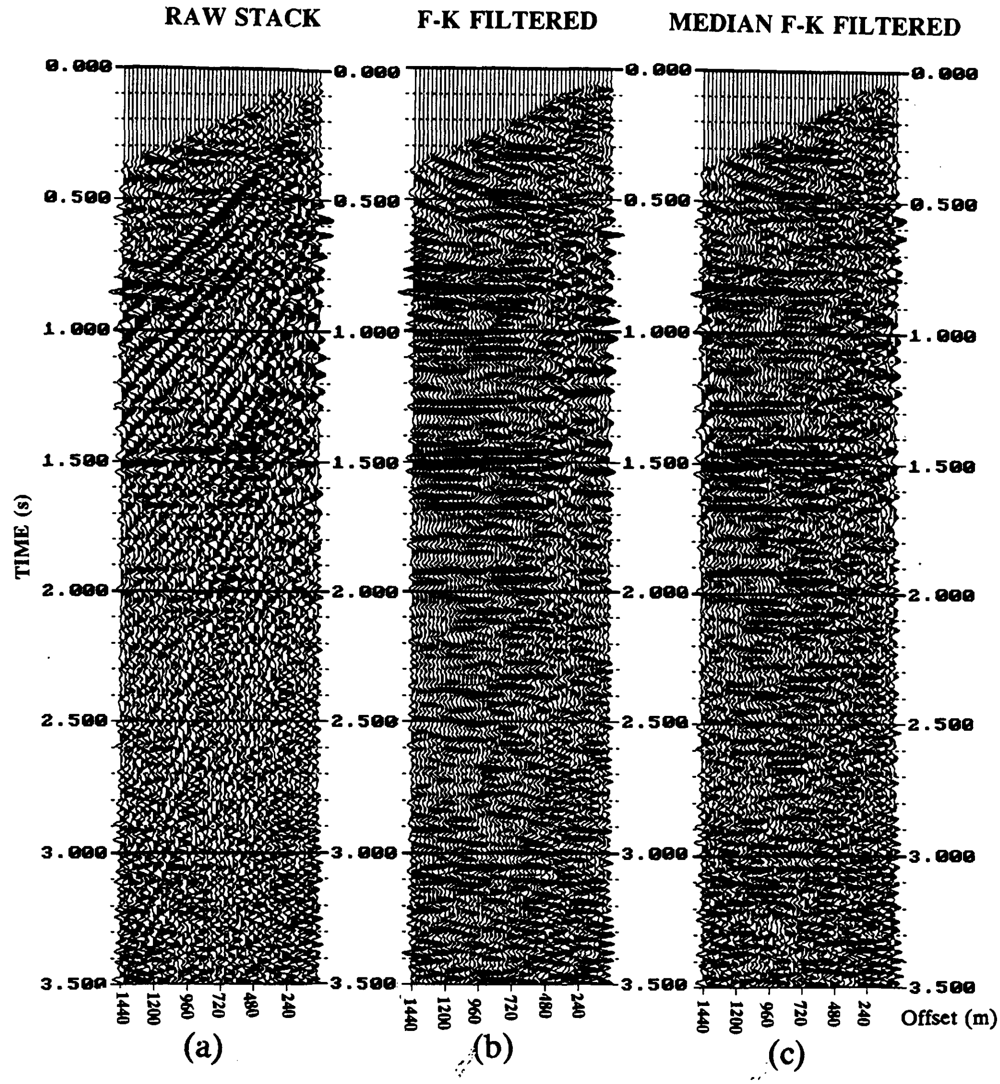

Figure 2.21 Common offset stacks for Springbank P-SV data a) no pre-stack spatial filtering b) *f-k* filtered c) weighted median *f-k* filtered.

Figure 2.22. When applied post-stack, these filters require only a fraction of the computer time required for pre-stack applications, but post-stack processing is not as desirable in terms of signal-to-noise improvement. Pre-stacking processes such as trim statics, power stacking (weighting traces by cross-correlation coefficients) or residual NMO do not have the benefit of the cleaner pre-stack filtered shot gathers or the improved correlation model.

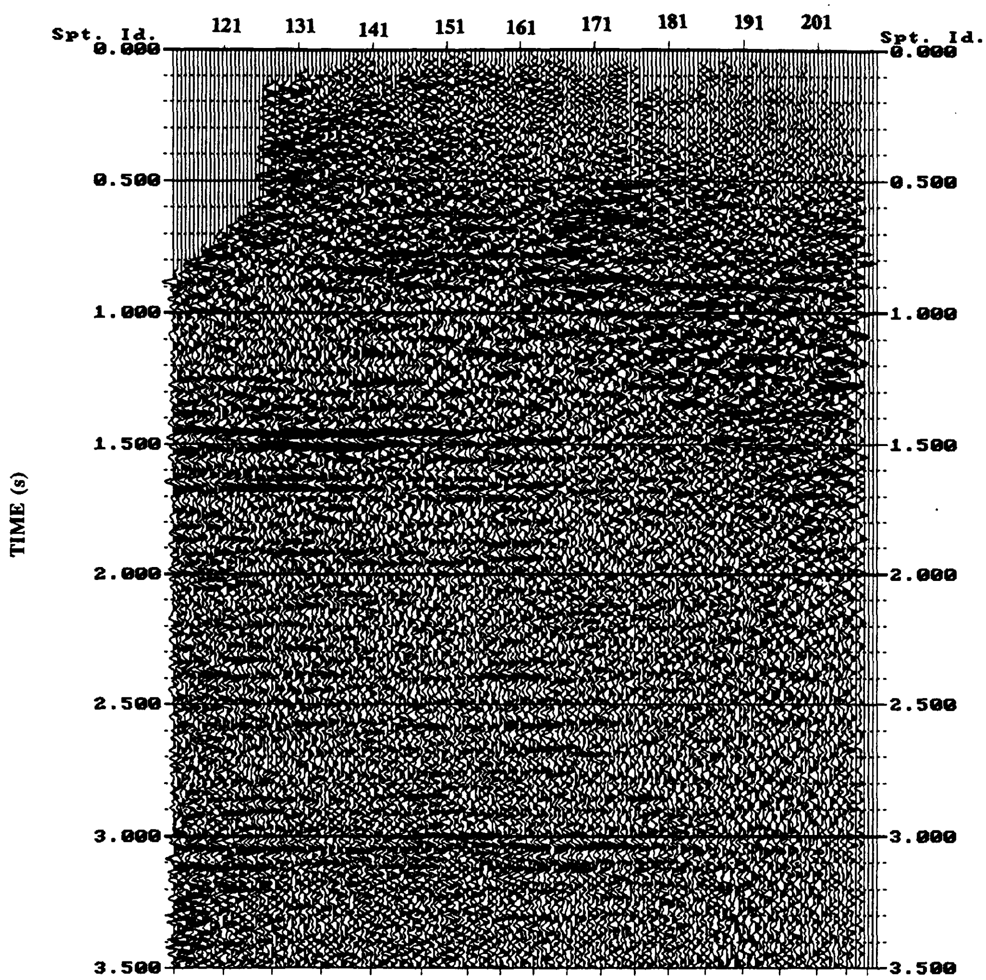

Figure 2.22 Final stack for Springbank FS90-1 P-SV data with no spatial filtering.

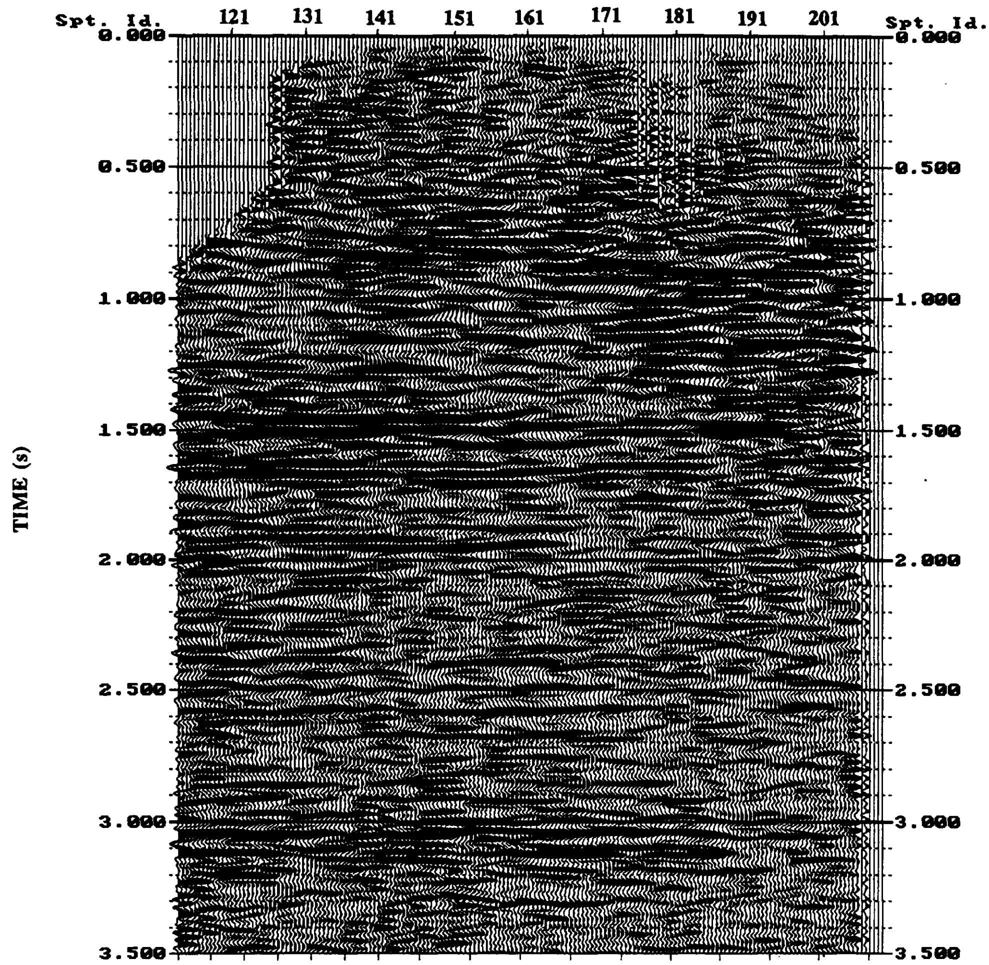

Figure 2.23 Final stack for Springbank FS90-1 P-SV data with post-stack *f-k* filter (reject dips > ± 4 ms/trace).

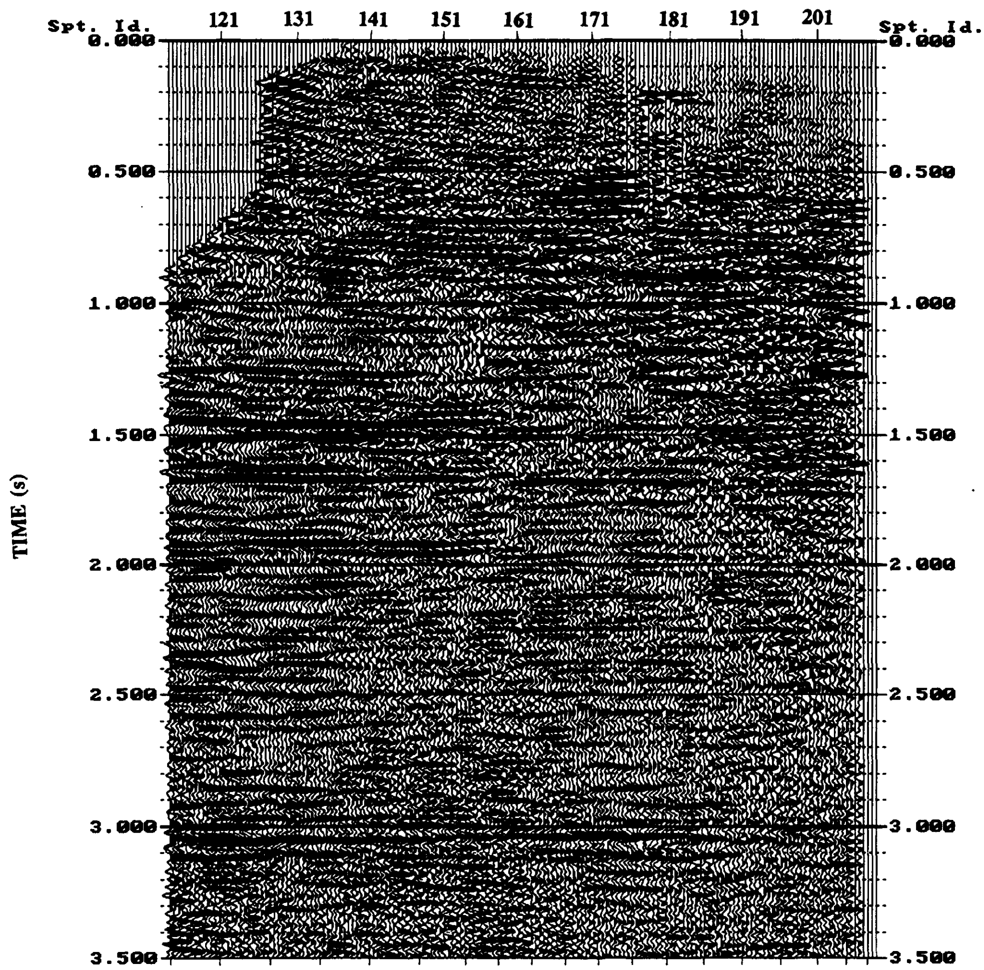

Figure 2.24 Final stack for Springbank FS90-1 P-SV data with pre-stack *f-k* filter (reject dips > $\pm$4ms/trace after NMO).

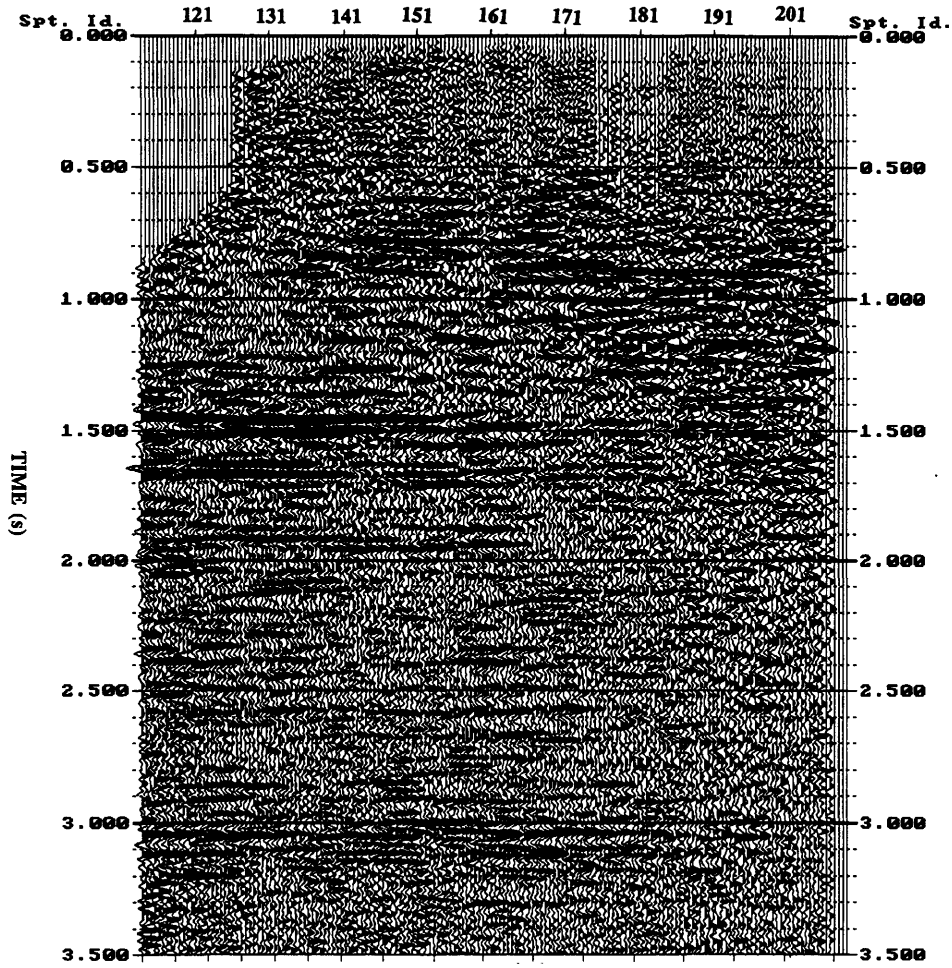

Figure 2.25 Final stack for Springbank FS90-1 P-SV data with post-stack median *f-k* filter (reject dips > $\pm$4 ms/trace).

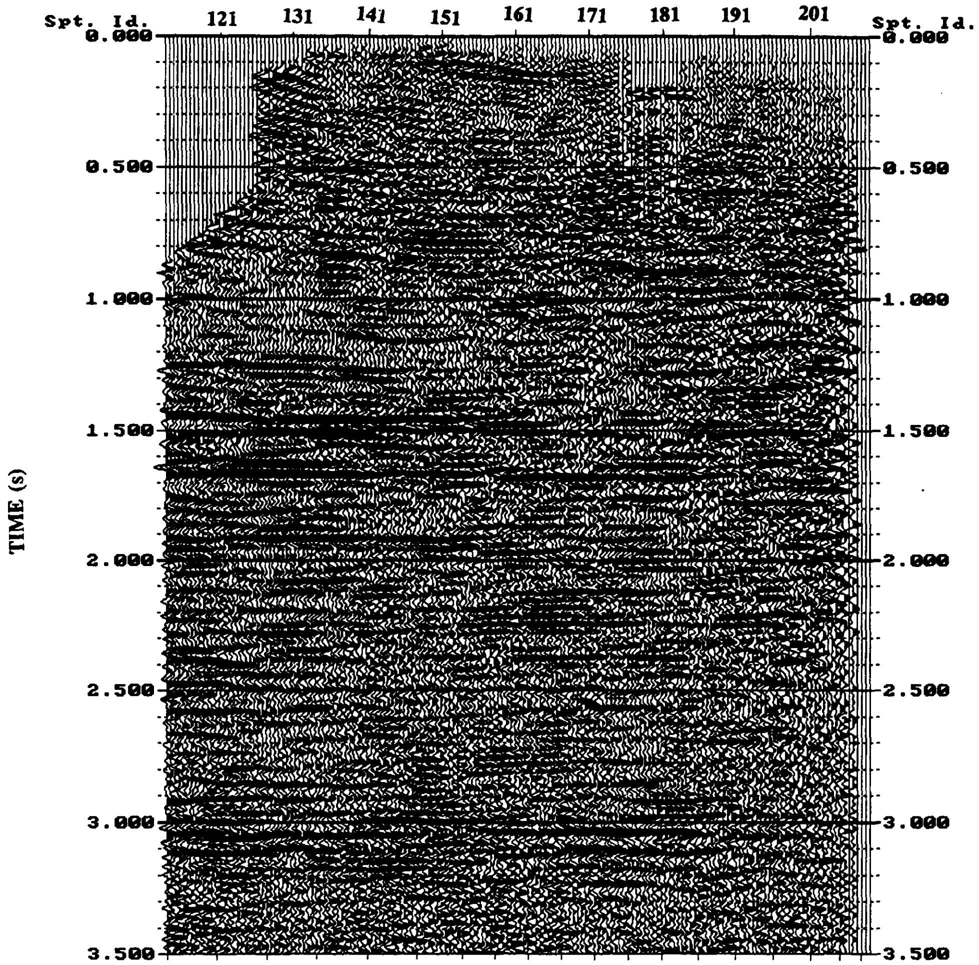

Figure 2.26 Final stack for Springbank FS90-1 P-SV data with pre-stack median *f-k* filter (reject dips > ± 4 ms/trace after NMO).

Chapter 3 RAYLEIGH WAVE DISPERSION

3.1 Introduction

Rayleigh waves are surface waves which exhibit retrograde elliptical ground motion in the vertical plane through the source and receiver. They have an evanescent character (their amplitude decays with depth below a certain frequency-dependent value). Rayleigh waves decrease in amplitude by a factor $r^{-½}$ from the source, where r is the distance travelled. The amplitudes of body waves in a homogeneous medium decay at a rate of r^{-1} which is faster than Rayleigh waves. This means that at large distances, Rayleigh waves would carry more energy than body waves. Their phase velocities, which are generally frequency-dependent, are related to the propagation parameters of the near-surface layers, primarily shear-wave velocities and thicknesses.

The propagation of Rayleigh waves is extremely complex and a great deal of literature has been devoted to the subject, particularly within the realm of earthquake seismology (Landisman *et al.*, 1969). The analysis of dispersive surface waves can provide detailed crustal shear-wave velocity information (Brune and Dorman, 1963; Nolet, 1977). More recently, spectral analysis of surface waves has been used to determine elastic moduli profiles of engineering sites (Hiltunen and Woods, 1989; Nazarian and Stokoe, 1989; Rix *et al.*, 1990).

The dispersive quality of ground roll in exploration seismology has been known for some time (Dobrin *et al.*, 1951; Tolstoy and Usdin, 1953; Mooney and Bolt, 1966; Nolet and Panza, 1976; Al-Husseini *et al.*, 1981). Recent attempts have been made to invert the dispersion characteristics of Rayleigh and Love waves for near-surface lithology (Russell, 1987; Gabriels *et al*, 1987; Song *et al*, 1989; Wattrus, 1989; Yuan and Nazarian, 1990). Often, these inversions are used for static corrections of shear-wave reflection sections (Mari, 1984; Szelwis and Behle, 1987). A second application is to phase-match dispersive noise trains to compress and remove them from the shot record and to improve the output reflection section. This has been done for ice-break noise in arctic seismic shot records (Beresford-Smith and Rango, 1988), guided waves in marine data processing (Yilmaz, 1987), and general ground roll removal on pre-stack shot records (Saatçilar and Canitez, 1988;

Herrmann and Russell, 1990; Glangeaud, 1990).

The estimation and inversion of Rayleigh waves is not done routinely to remove ground roll because of the complexity of dispersion characteristics due to rapidly varying lithologic parameters and the relatively high Poisson's ratio found in the unconsolidated alluvium usually present in the near-surface layers.

3.2 Theory

Dziewonski and Hales (1972) define phase velocity as the instantaneous velocity of plane waves at a given frequency:

$$c(\omega) = \frac{dx}{dt} = \frac{\omega}{k(\omega)}, \tag{3.1}$$

and the group velocity as the velocity of transmission:

$$u(\omega) = \frac{x}{t} = \frac{d\omega}{dk} = c(\omega) + k(\omega)\frac{dc(\omega)}{dk(\omega)}. \tag{3.2}$$

The approximation of surface waves as sums of plane waves is generally valid at large distances from the source (Aki and Richards, 1980). In exploration seismology, this distance is usually considered to be 4 or 5 times the thicknesses of the guided wave channel (Waters, 1978).

To understand the propagation and dispersion of Rayleigh waves, we first look at the physical composition of Love waves (SH-wave) which are less complex and easier to interpret. This theory is then extended to the more complex Rayleigh waves which are composed of both vertical (P-wave) and radial (SV-wave) component ground motion.

3.2.1 Love waves

First, consider the simple case of a Love wave in a layer of thickness, h, overlying an isotropic elastic half-space. The derivation follows that of Aki and Richards (1980) and is included here for completeness. The propagation of plane SH-waves can be described by the two-dimensional wave equation:

$$\nabla^2 u = \frac{\partial^2 u}{\partial x^2} + \frac{\partial^2 u}{\partial z^2} = \frac{1}{\beta^2} \frac{\partial^2 u}{\partial t^2} \quad , \tag{3.3}$$

where $u(x,z,t)$ is their displacement. If the body force is zero, then

$$\begin{aligned} \nabla^2 u_y &= \frac{\ddot{u}_y}{\beta^2} && z>h, \\ \nabla^2 u_y &= \frac{\ddot{u}_y}{\beta'^2} && 0<z<h, \end{aligned} \tag{3.4}$$

where u_y is the displacement in the transverse horizontal direction and β is the shear-wave velocity. Within this layer we have both upgoing and downgoing waves so the displacement

$$u'_y = C' e^{ik(x+s'z)-i\omega t} + F' e^{ik(x-s'z)-i\omega t} \tag{3.5}$$

with $s' = \sqrt{\frac{1}{\beta'^2} - \frac{1}{c^2}}$ where c is the Love-wave phase velocity and β is the shear-wave phase velocity. Similarly, in the substratum which only has a downgoing wave:

$$u_y = C e^{ik(x+sz)-i\omega t} \tag{3.6}$$

where $s = \sqrt{\frac{1}{\beta^2} - \frac{1}{c^2}}$. Applying the boundary conditions, namely continuity of stress (σ_{yz}) and displacement (u_y) at the interface $z=h$ and zero traction ($\sigma_{yz}=0$) at the free surface $z=0$ gives:

$$\begin{aligned} & \frac{\beta^2}{\rho} \frac{\partial u_y}{\partial z} = 0 && z=0 \ , \\ u'_y = u_y, \quad & \frac{\beta'^2}{\rho'} \frac{\partial u_y}{\partial z} = \frac{\beta^2}{\rho} \frac{\partial u_y}{\partial z} && z=h \ . \end{aligned} \tag{3.7}$$

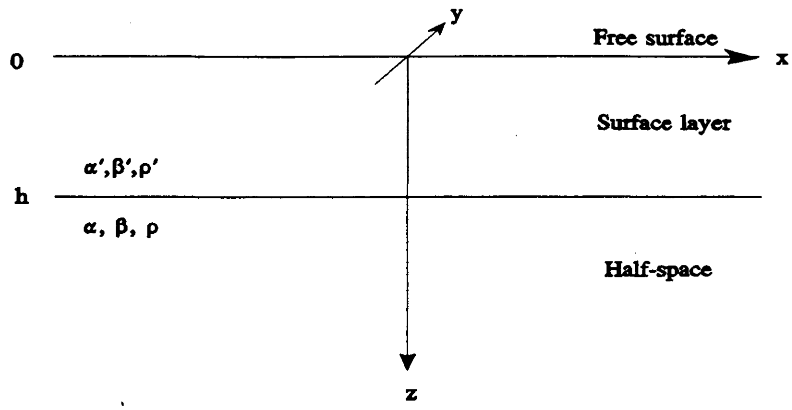

Figure 3.1 Simple model consisting of a layer over a half-space.

The free-surface condition $\partial u/\partial z=0$ at $z=0$ means $C'=F'$. Then, substituting equation 3.5 and 3.6 into these boundary conditions gives:

$$2C'\cos\left(\omega h\sqrt{\frac{1}{\beta'^2}-\frac{1}{c^2}}\right) = Ce^{i\omega h\sqrt{\frac{1}{\beta^2}-\frac{1}{c^2}}},$$
$$2iC'\mu'\omega\sqrt{\frac{1}{\beta'^2}-\frac{1}{c^2}}\sin\left(\omega h\sqrt{\frac{1}{\beta'^2}-\frac{1}{c^2}}\right) = \mu\omega\sqrt{\frac{1}{\beta^2}-\frac{1}{c^2}}Ce^{i\omega h\sqrt{\frac{1}{\beta^2}-\frac{1}{c^2}}}. \tag{3.8}$$

The nontrivial solution $(C,C'\neq 0)$ is found by setting the determinant of the coefficient matrix equal to zero. This gives:

$$\tan\left(\omega h\sqrt{\frac{1}{\beta'^2}-\frac{1}{c^2}}\right) = \frac{i\mu\sqrt{\frac{1}{c^2}-\frac{1}{\beta^2}}}{\mu'\sqrt{\frac{1}{\beta'^2}-\frac{1}{c^2}}} \tag{3.9}$$

where $\mu=\beta^2/\rho$ is the rigidity modulus. For eq. (3.9) to be physically realizable,

$\beta' \leq c \leq \beta$. Note also that the numerator is positive imaginary (ie. $\beta > c$) and this means that the wave is an evanescent wave. Note the left-hand side is multivalued and the right-hand side is single-valued. Eq. (3.9) must be solved graphically for c by plotting the right-hand and left-hand sides versus $h\sqrt{\frac{1}{\beta^2}-\frac{1}{c^2}}$. The roots of the equation occur where the two sides of the equation intersect. Within the range $\beta_1 \leq c \leq \beta_2$ there is a finite number of branches to tan(ω...) consequently, for real c, a finite number of normal mòdes. This gives a relation between c and ω, the roots of eq. (3.9), for certain n (or normal mode) that is unique to the fixed parameters ρ, β and h. This leads to a more general equation

$$\omega h\sqrt{\frac{1}{\beta'^2}-\frac{1}{c^2}}+n\pi = \tan^{-1}\left(\frac{i\mu\sqrt{\frac{1}{c^2}-\frac{1}{\beta^2}}}{\mu'\sqrt{\frac{1}{\beta'^2}-\frac{1}{c^2}}}\right), \tag{3.10}$$

where n is the normal mode ($n = 0,1,2,...$).

3.2.2 Rayleigh waves

We consider the simple case of an half-space with a plane wave travelling in the x direction as shown in Figure 3.2. The displacements u_x and u_z and the normal stresses σ_z and shear stresses τ_{xz} can all be derived from a scalar potential ϕ and a vector potential ψ. These potentials are obtained as solutions of the wave equations

$$\begin{aligned} \nabla^2\phi &= \frac{1}{\alpha^2}\frac{\partial^2\phi}{\partial t^2}, \\ \nabla^2\psi &= \frac{1}{\beta^2}\frac{\partial^2\psi}{\partial t^2}. \end{aligned} \tag{3.11}$$

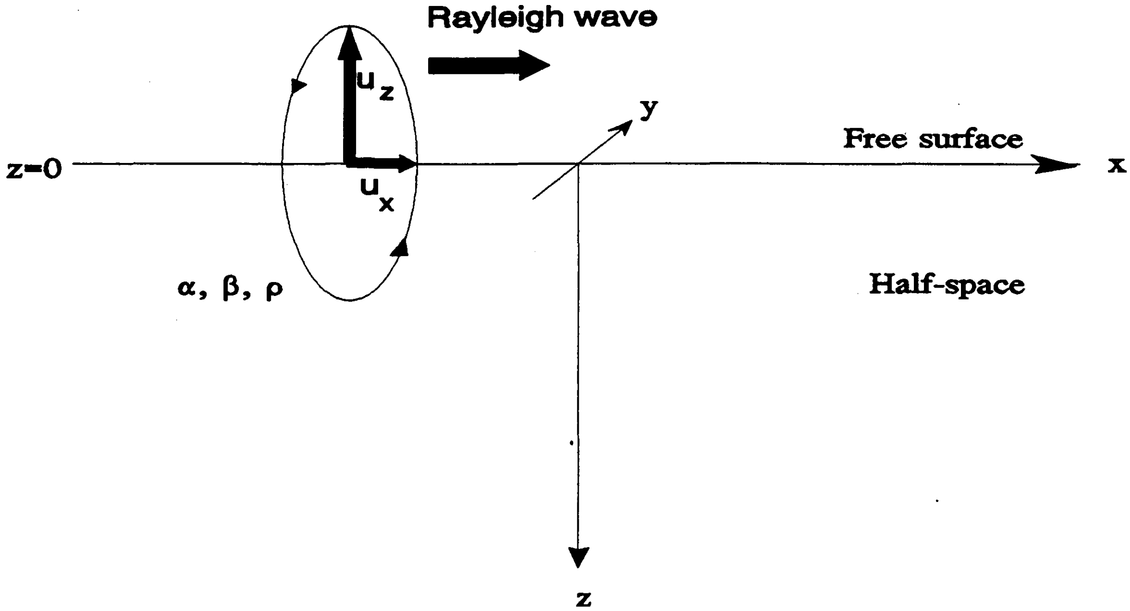

Figure 3.2 Isotropic, homogeneous half-space model with Rayleigh wave.

Assuming plane waves, the potentials can be taken as

$$\begin{aligned} \phi &= Ae^{(ikx-\sqrt{k^2-k_\alpha^2}\,z-i\omega t)} \\ \psi &= Be^{(ikx-\sqrt{k^2-k_\beta^2}\,z-i\omega t)} \end{aligned} \tag{3.12}$$

where $k = \omega/c$, $k_\alpha = \omega/\alpha$ and $k_\beta = \omega/\beta$. The displacements are related to these potentials as

$$\begin{aligned} u_x &= \frac{\partial\phi}{\partial x} - \frac{\partial\psi}{\partial z}, \\ u_z &= \frac{\partial\phi}{\partial z} + \frac{\partial\psi}{\partial x}, \end{aligned} \tag{3.13}$$

the normal stress as

$$\sigma_z = \lambda\nabla^2\phi + 2\mu\frac{\partial^2\phi}{\partial z^2} + 2\mu\frac{\partial^2\psi}{\partial x\partial z}, \tag{3.14}$$

and shear stress as

$$\tau_{xz}=\mu\left(2\frac{\partial^2\phi}{\partial x\partial z}+\frac{\partial^2\psi}{\partial x^2}-\frac{\partial^2\psi}{\partial^2 z}\right) . \tag{3.15}$$

Applying the boundary conditions at the free surface ($z=0$), ie. that normal and shear stresses equal zero, and substituting in the equations for the potentials gives:

$$\begin{aligned}(\frac{2}{c^2}-\frac{1}{\beta^2})A-\frac{2i}{c}\sqrt{\frac{1}{c^2}-\frac{1}{\beta^2}}B &= 0 ,\\ \frac{-2i}{c}\sqrt{\frac{1}{c^2}-\frac{1}{\alpha^2}}A-(\frac{2}{c^2}-\frac{1}{\beta^2})B &= 0 ,\end{aligned} \tag{3.16}$$

which can be solved by setting the determinants of the coefficients A and B equal zero. This leads to an expression relating the phase velocity, and compressional (α) and shear velocities (β) as:

$$\left(\frac{c}{\beta}\right)^6-8\left(\frac{c}{\beta}\right)^4+\left(24-16\frac{\beta^2}{\alpha^2}\right)\left(\frac{c}{\beta}\right)^2-16\left(1-\frac{\beta^2}{\alpha^2}\right)=0 \tag{3.17}$$

(Al-Husseini *et al*, 1981). This demonstrates that the non-dispersive Rayleigh wave velocity is a function of shear and compressional velocities only. Poisson's ratio σ is defined as

$$\sigma=\frac{1}{2}\frac{1-(\beta/\alpha)^2}{1+(\beta/\alpha)^2} \tag{3.18}$$

and the relationships of c/α (V_S/V_P), c/β (V_R/V_P), and σ are depicted in Figure 3.3. This information is useful in predicting reasonable Rayleigh and/or shear velocities when only the compressional velocities are known.

When there are multiple near-surface layers, the Rayleigh waves are dispersive similar to the Love wave

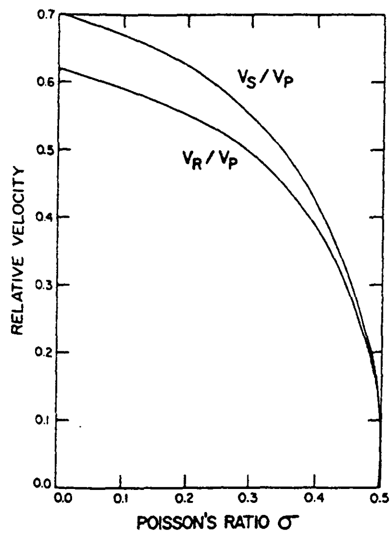

Figure 3.3 Velocity ratios as a function of Poisson's ratio (after Knopoff, 1952)

model previously derived in section 3.2.1, except that they are polarized in the x-z plane (Figure 3.2). From the displacement eq. (3.13) and the solutions of the coefficients given by eq. (3.16) we can derive the displacements. Both u_x and u_z decay exponentially with depth. At the free surface ($z=0$), they become

$$u_x = i\frac{c}{2\beta^2}Ae^{i\omega(\frac{x}{c}-t)}$$
$$u_z = \sqrt{1/c^2-1/\alpha^2}\left(-1+\frac{\sqrt{1/c^2-1/\beta^2}}{\sqrt{1/c^2-1/\alpha^2}}\right)Ae^{i\omega(\frac{x}{c}-t)} \, . \tag{3.19}$$

Therefore, a particle at the free surface describes an elliptical path which is vertically polarized (in the x,z plane). The x direction motion lags behind the z direction motion by 90°, which means the motion is retrograde.

3.2.2.1 Eigenvalue problem for surface waves

The determination of c_n and the displacements can be rewritten as an eigenvalue problem. The displacement of a surface wave propagating in the x direction with amplitude dependent on depth (z) is

$$u = L(z)e^{ikx-\omega t}. \tag{3.20}$$

Substituting this into the 2-D wave equation (3.3) we get

$$\frac{d^2L}{dz^2} = -\omega^2 s^2 L. \tag{3.21}$$

This can be written as a first-order differential equation in the matrix form:

$$LU = \lambda U. \tag{3.22}$$

For Love waves (Aki and Richards, 1980):

$$\frac{d}{dz}\begin{pmatrix} l_1 \\ l_2 \end{pmatrix} = \begin{pmatrix} 0 & \mu^{-1} \\ k^2\mu-\omega^2\rho & 0 \end{pmatrix}\begin{pmatrix} l_1 \\ l_2 \end{pmatrix} \tag{3.23}$$

where ρ is density, ω is angular frequency, k is wavenumber ($k=\omega/c$), μ is the rigidity modulus ($\mu=\beta^2/\rho$), l_1 is the horizontal displacement eigenfunction, and l_2 is the horizontal stress eigenfunction.

Similarly, for Rayleigh waves:

$$\frac{d}{dz}\begin{pmatrix} r_1 \\ r_2 \\ r_3 \\ r_4 \end{pmatrix} = \begin{pmatrix} 0 & -k & \mu^{-1} & 0 \\ k\lambda(\lambda+2\mu)^{-1} & 0 & 0 & (\lambda+2\mu)^{-1} \\ k^2\zeta-\omega^2\rho & 0 & 0 & -k\lambda(\lambda+2\mu)^{-1} \\ 0 & -\omega^2\rho & k & 0 \end{pmatrix}\begin{pmatrix} r_1 \\ r_2 \\ r_3 \\ r_4 \end{pmatrix} \tag{3.24}$$

where $\zeta=4\mu(\lambda+\mu)/(\lambda+2\mu)$, λ is a Lame constant, and μ, ω and ρ are as above. r_1 is the radial displacement eigenfunction, r_2 vertical displacement eigenfunction, r_3 radial stress eigenfunction, and r_4 vertical stress eigenfunction which are all functions of ω, k, and z. ρ, λ, and μ are functions of depth (z). The boundary conditions for both types of waves are displacement eigenfunctions that disappear when $z=\infty$ and stress eigenfunctions that vanish at the free surface $z=0$.

The propagator matrix method of Thomson (1950) and Haskell (1953) can be applied to a stack of homogeneous layers over a half-space. Matrix equations 3.24 and 3.25 are generalized as

$$\frac{df(z)}{dz}=A(z)f(z)\ , \tag{3.25}$$

where $f(z)$ is a column vector and $A(z)$ is an nxn matrix ($n=2$ for Love waves and $n=4$ for Rayleigh waves). The detailed mathematics for the solution of these matrices is given for Rayleigh waves by Abo-Zena (1979).

3.3 Dispersion modelling

To understand the effects of near-surface lithology on the dispersion of ground roll, a simple near-surface model was established based on the refraction analysis of the Springbank data (Figure 3.4). The matrix method is used to integrate the Rayleigh-wave equation (3.14), and assumes that the model is represented by a stack of homogeneous isotropic layers (Takeuchi and Saito, 1972; Schwab and Knopoff, 1972). These methods require further refinements at the higher frequencies needed in exploration seismology (Abo-Zena, 1979), specifically, when the thickness of a layer is greater than several wavelengths. Recently, public domain algorithms have been made available to calculate phase velocity versus frequency or dispersion curves for multiple layers in the near-surface (Doornbos, 1988).

The model parameters density, thickness, and P- and S-wave velocities for the shallow layers of Figure 3.4 were perturbed by a factor of 20% to demonstrate their importance in effecting the dispersion of ground roll. Figures 3.5 and 3.6 show only a minimal dependence of dispersion on P-wave velocities and densities. A thicker propagation layer causes a steeper dispersion curve (Figure 3.7) and thinner layers cause the curves to move to higher frequencies. In the limit of an infinitely thick layer, relative to wavelength, a non-dispersive phase velocity-frequency curve will result. Furthermore, these curves are bounded at lower frequencies by the underlying S-wave velocities and at higher frequencies by the surface wave propagating matrix velocities (Figure 3.8 and 3.9). Note also that for limited low-frequency response of geophones the primary modes of dispersive surface waves may not be observed resulting in higher frequency or higher modes of the same velocity bound dispersion curve (Mooney and Bolt, 1966). Clearly, the shape of the dispersion curve is primarily dependent on the near-surface shear-wave velocities and thicknesses.

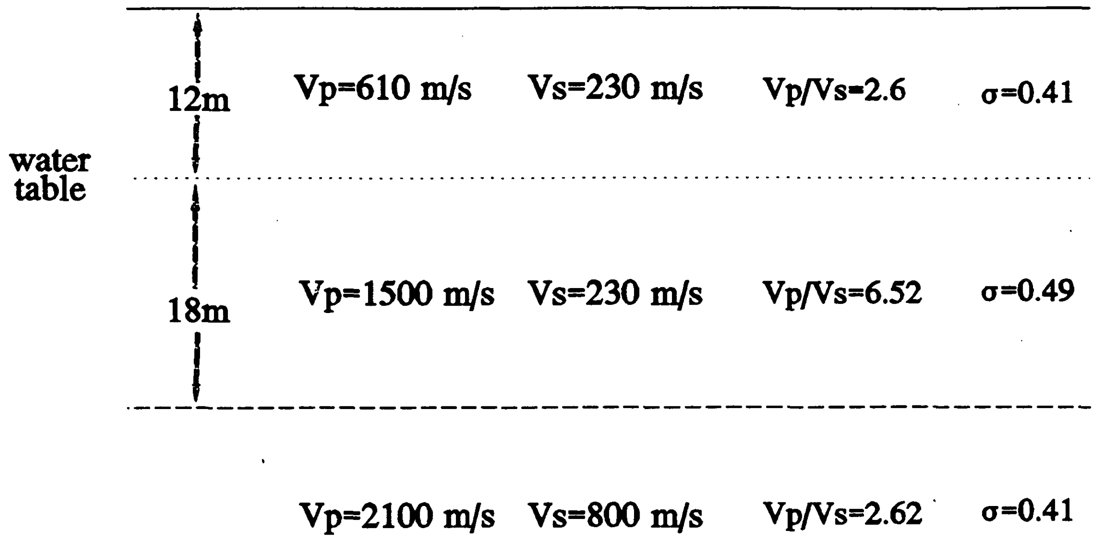

Figure 3.4 Springbank near-surface model.

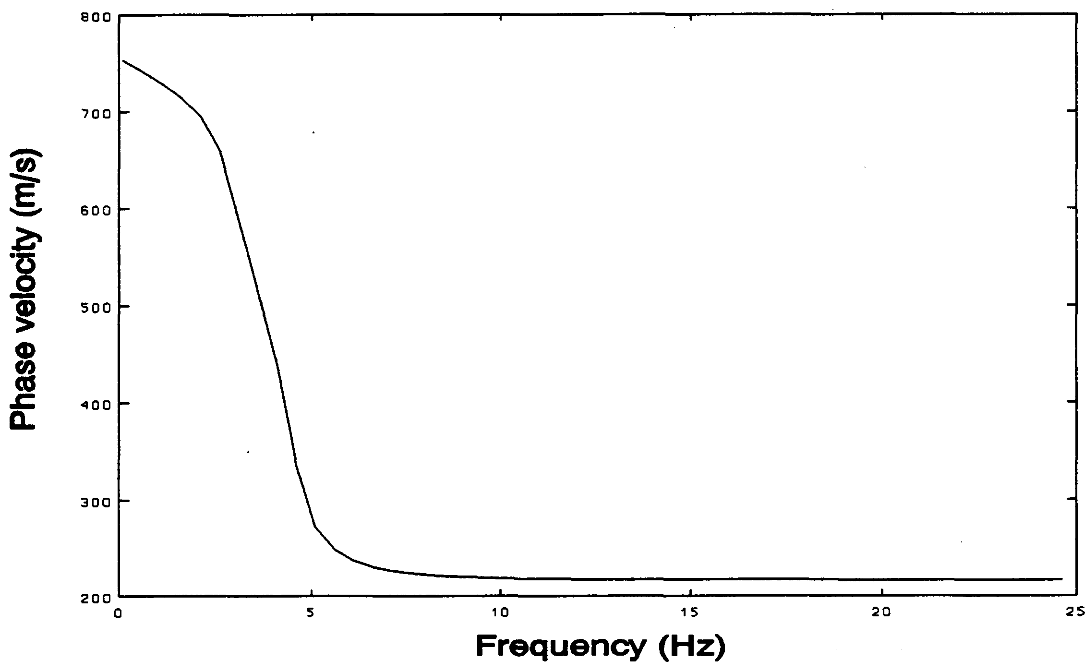

Figure 3.5 Rayleigh wave dispersion curves for varying densities ($\rho = \pm 20\%$). Note the dispersion curves for differing densities are almost identical.

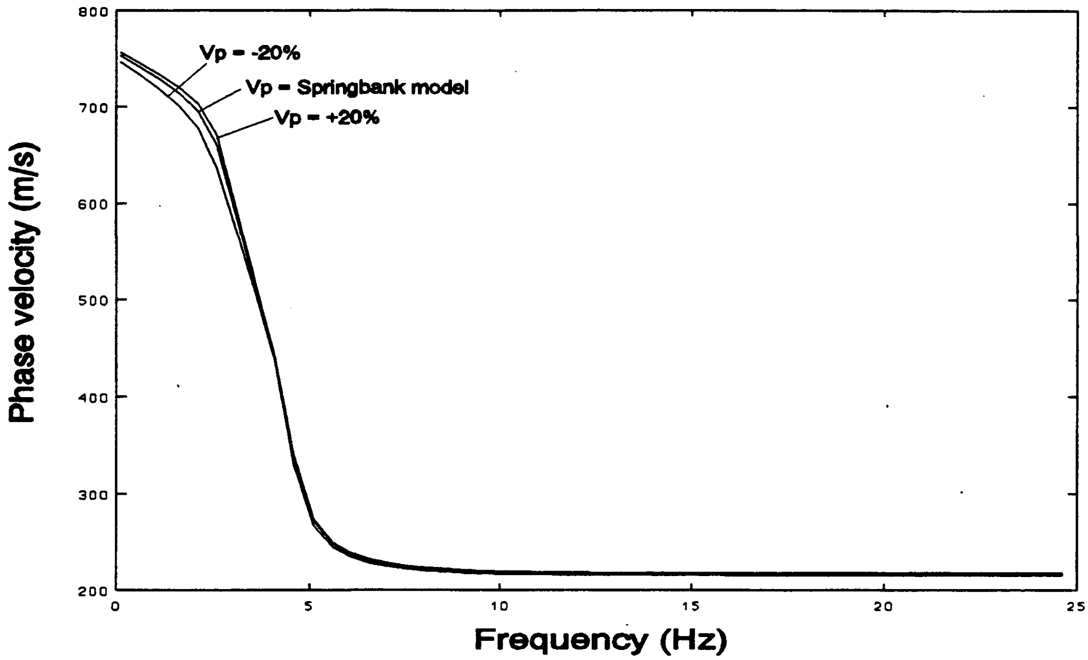

Figure 3.6 Rayleigh wave dispersion curves for varying P-wave velocities.

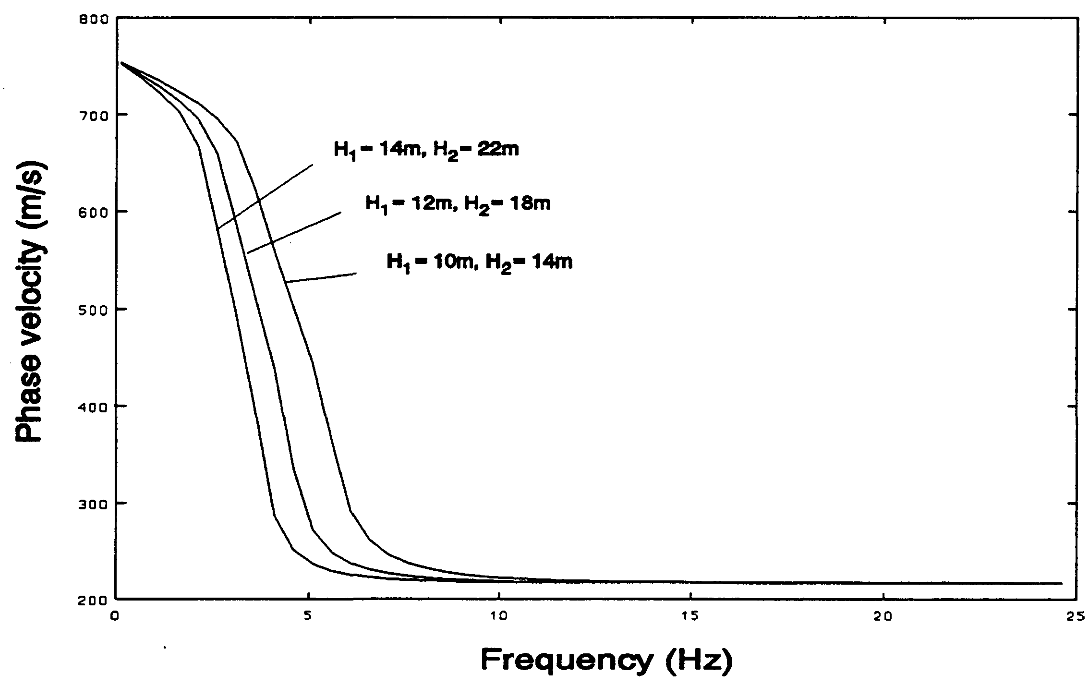

Figure 3.7 Rayleigh wave dispersion curves for varying near-surface thicknesses.

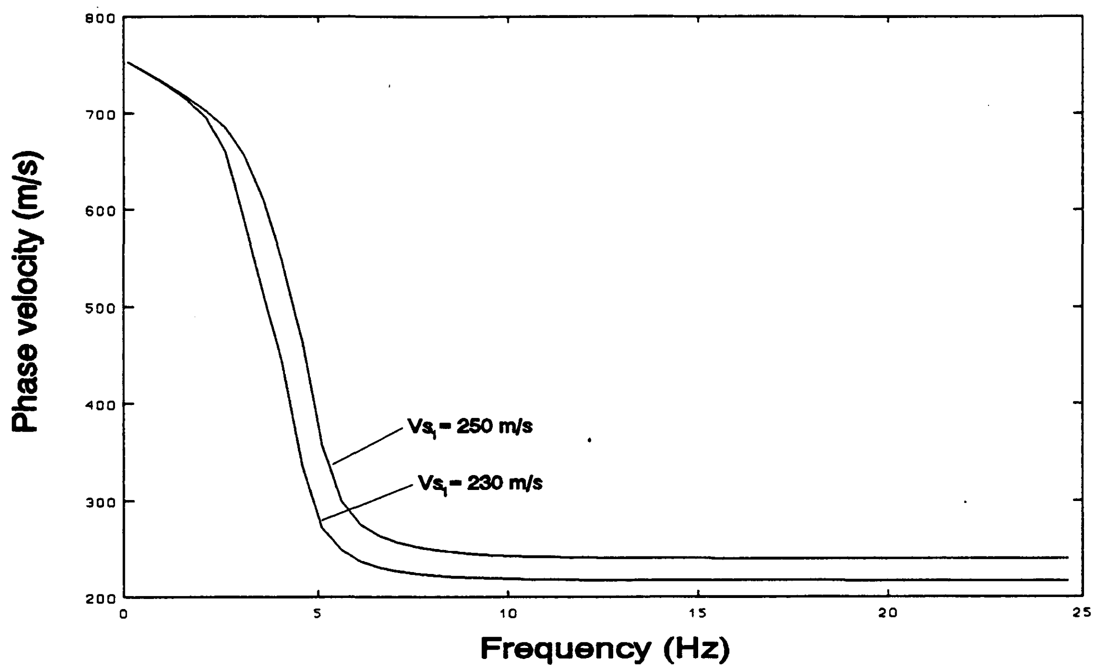

Figure 3.8 Rayleigh wave dispersion curves for varying S-wave velocity in the first layer.

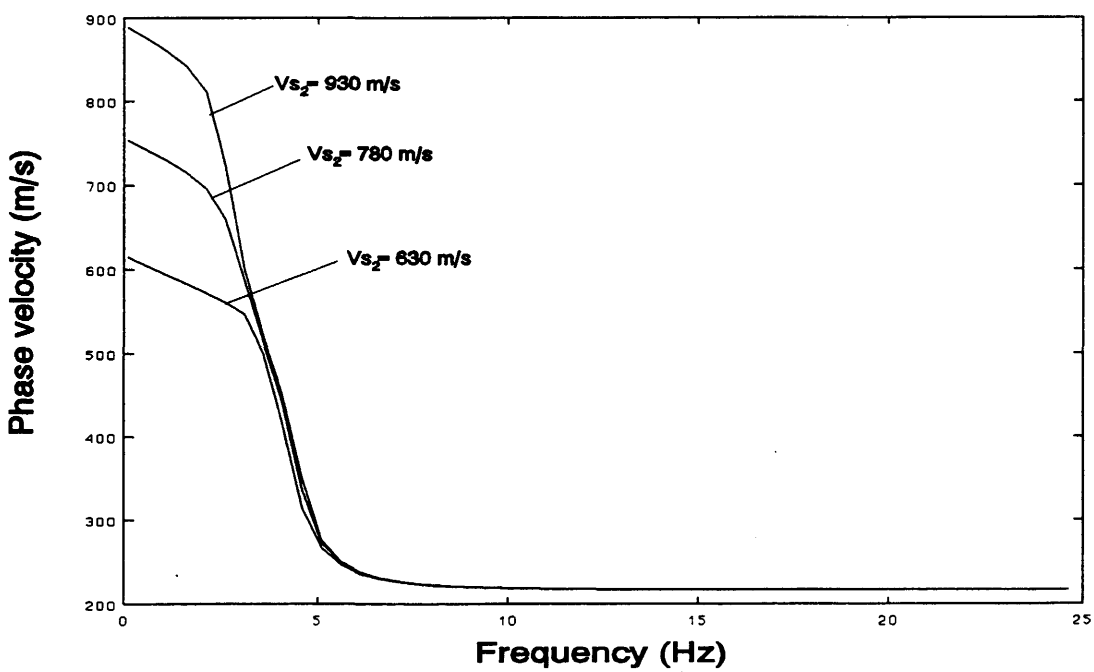

Figure 3.9 Rayleigh wave dispersion curves for varying S-wave velocity in the second layer.

3.4 The ω-p transform

Transforming a shot gather to the frequency-slowness (ω-p) domain enables a direct analysis of the dispersion curves (McMechan and Yedlin, 1981). This process makes use of the complete shot gather by first doing a slant stack. A slant stack involves summing along lines across the shot record at various dips or velocities (p or ray parameter) and intercept times (τ). This slowness-time intercept transform (referred to as τ-p) is followed by a 1-D Fourier transform over τ to get frequency, ω. In this new domain (ω-p), dispersion curves for the Rayleigh wave normal mode and higher modes are directly observable in principle.

A few difficulties with this analysis can impede direct estimation of the dispersion curves. These include low signal-to-noise ratio, aliased linear noise, limited bandwidth of the raw data, and rapid variation in shear velocities or thicknesses of the near-surface layers.

3.4.1 Theory

Only by assuming a single propagating mode can the phase velocity be determined directly from the phase of the 2-D Fourier transform. Generally, there can be an infinite number of wavenumber (k) solutions or modes to the equation of motion for Rayleigh waves (Gabriels *et al*, 1987). Therefore, a more robust method to isolate individual normal modes of propagation is required.

As previously discussed, a linear moveout correction is applied to the data as:

$$\tau = t - px \tag{3.26}$$

where p is the slowness vector or ray parameter ($p = \sin\theta / v$), x is the offset, and t is time. τ represents the linearly moved out time or intercept of the slanted path. Next, the data are summed over the offset axis as:

$$S(x,\tau) = \sum_x p(x, t+px) \tag{3.27}$$

where $S(x,\tau)$ is a plane wave with ray parameter p. By repeating this process over a range of p and summing over the offset, a complete slant-stack gather consisting of all the dip components of the time-offset gather is obtained.

Figure 3.10 provides a graphical representation of this process. The zero-offset point, A, of a reflection hyperbola in an offset gather is summed along a horizontal path ($1/V=0$ or $V=\infty$) to a point A'. By tilting the line of summation and decreasing the intercept time, the hyperbola is intersected at a point B. The Fresnel zone or point-of-tangency about this point determines the amplitude and distinction of the point B' in the τ-p domain. This Fresnel zone gets larger at higher velocities, deeper events and lower frequencies (Yilmaz, 1987). The steepest necessary path for this hyperbola is the asymptote $p=1/V$, which corresponds to horizontal rays. A linear event such as a refracted event or non-dispersive ground roll (event D) should map into a single point (D').

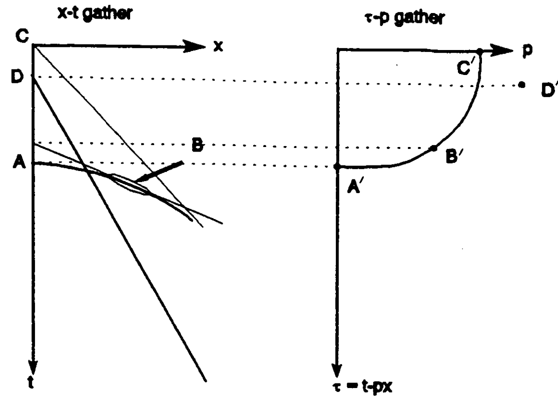

Figure 3.10 Mapping an x-t gather to the τ-p domain.

The phase difference between two stations, in the same plane as the source, is represented by $k_m(\omega)\Delta x$, where Δx is the distance between stations. If $k_m(\omega)$ is identified correctly, the phases of a propagating mode can be aligned and summed at a maximum. Equation 3.1 can be re-written as

$$k_m(\omega)=\frac{\omega}{c_m(\omega)}=\omega p(\omega) \tag{3.28}$$

where $p_m = 1/c_m$ is slowness. The slant stacking wavefield transformation of McMechan and Yedlin (1981) yields these modes directly by first mapping the data to τ-p, and then by way of a Fourier transform in τ to ω-p. If the slowness is approximately a linear function of frequency, the ground roll is linearly modulated. The frequency band of the desired compression operator can then be measured directly.

3.4.2 Application to Synthetic Data

Based on a model of the Jumping Pound area, three two-component full wavefield shot gathers were generated to show the dispersive qualities of Rayleigh waves. The software package, VESPA written by Sierra Geophysics, and based on the matrix method for the solution of a number of thin horizontal homogeneous layers (Aki and Richards, 1980), was used. Vertical and radial component shot gathers were output to SEG-Y tapes to be processed with a standard seismic processing package. The specific parameters are listed in section 1.5.1.2.

Figures 3.12 to 3.14 are the true amplitude shot gathers, after applying a bandpass filter (4-20 Hz), with 30 m trace interval and far offset of 1440 m. Figures 3.15 to 3.17 are the ω-p transforms of these shot gathers after applying amplitude compensation ($r^{1/2}$), slant stacking from 0 to 8000 ms/trace at the maximum offset of 1440 m (80 ms/trace increment), and 1-D Fourier transform in τ.

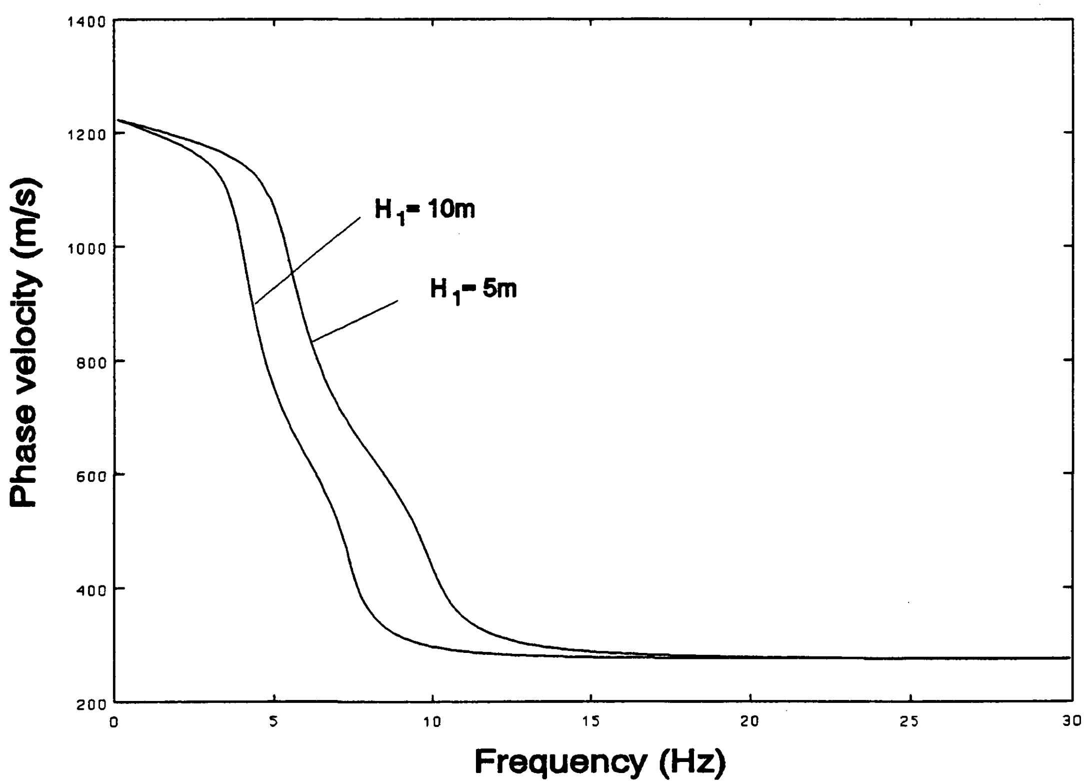

Figure 3.11 Jumping Pound model Rayleigh wave dispersion curve

The vertical components depict a larger-amplitude surface wave than the radial component. Furthermore, they are 90° out of phase; peaks on the radial component records occur at the zero crossings of the vertical component records. The results of spatial undersampling are shown in Figure 3.12, where the Rayleigh wave is seen at a negative dip (A). The corresponding waves in Figure 3.13 (Δx = 10m) are not aliased. Aliasing of surface waves occurs when $\Delta x \leq \beta_{min}/2f_{max}$ (Mari, 1984). In terms of the τ-p transform, Turner (1990), suggests that in order to avoid aliasing $\Delta x \leq 1/(2p_{max}f_{max})$ where p_{max} is the maximum slowness value. For the data in Figure 3.13 the maximum slope without aliasing for a 20 Hz wavelet is 3.6 s linear moveout at the maximum offset (x=1440 m) or 400 m/s. The minimum velocity required for the ω-p dispersion analysis is 295 m/s (β in the first layer). The lower velocity bounds of the dispersion curve are in fact found at the higher frequencies (refer Figure 3.11). Therefore, if β<295 m/s, the maximum spatial sampling required to avoid aliasing is 7.3 m ($\Delta x \leq 7.3$). However, aliasing in τ-p is the constructive summation of the directions that occur each time one period of the signal is skipped:

$$p(f)=p_{true}+n/\Delta x f \tag{3.29}$$

where n=0,1,2...

Velocities between 1500 m/s (Δt = 0.97 s) and 150 m/s (Δt = 3.5 s at 530 m) can be observed that are indicative of dispersive surface waves. Theoretically, the slope of the first mode of the dispersion curve occurs at approximately 4 to 9 Hz (Figure 3.11) within the velocity bounds 295-1300 m/s. On the ω-p plot 295 m/s is trace 63 and 1300 m/s is trace 14 as depicted in Figures 3.15 to 3.17. Figure 3.17, for the thin shallow layer (5m) shows that the theoretical dispersion curve (Figure 3.11) moves to higher frequency with similar slope, within the same velocity bounds.

These transforms would be difficult to interpret with additive noise on the shot record. Further, lateral changes within the spread would render this method invalid because we are assuming flat homogeneous layers within a spread length by using a multitrace transform. In section 4.3.3 the ω-p transform is applied to a real shot record from the nearby Springbank area. While this method of estimating near-surface parameters is ideally suited to shallow marine sediments (McMechan and Yedlin, 1981) or to remove guided waves in shallow water marine surveys (Yilmaz, 1987), it may not be useful for near-surface inversions for land seismic surveys.

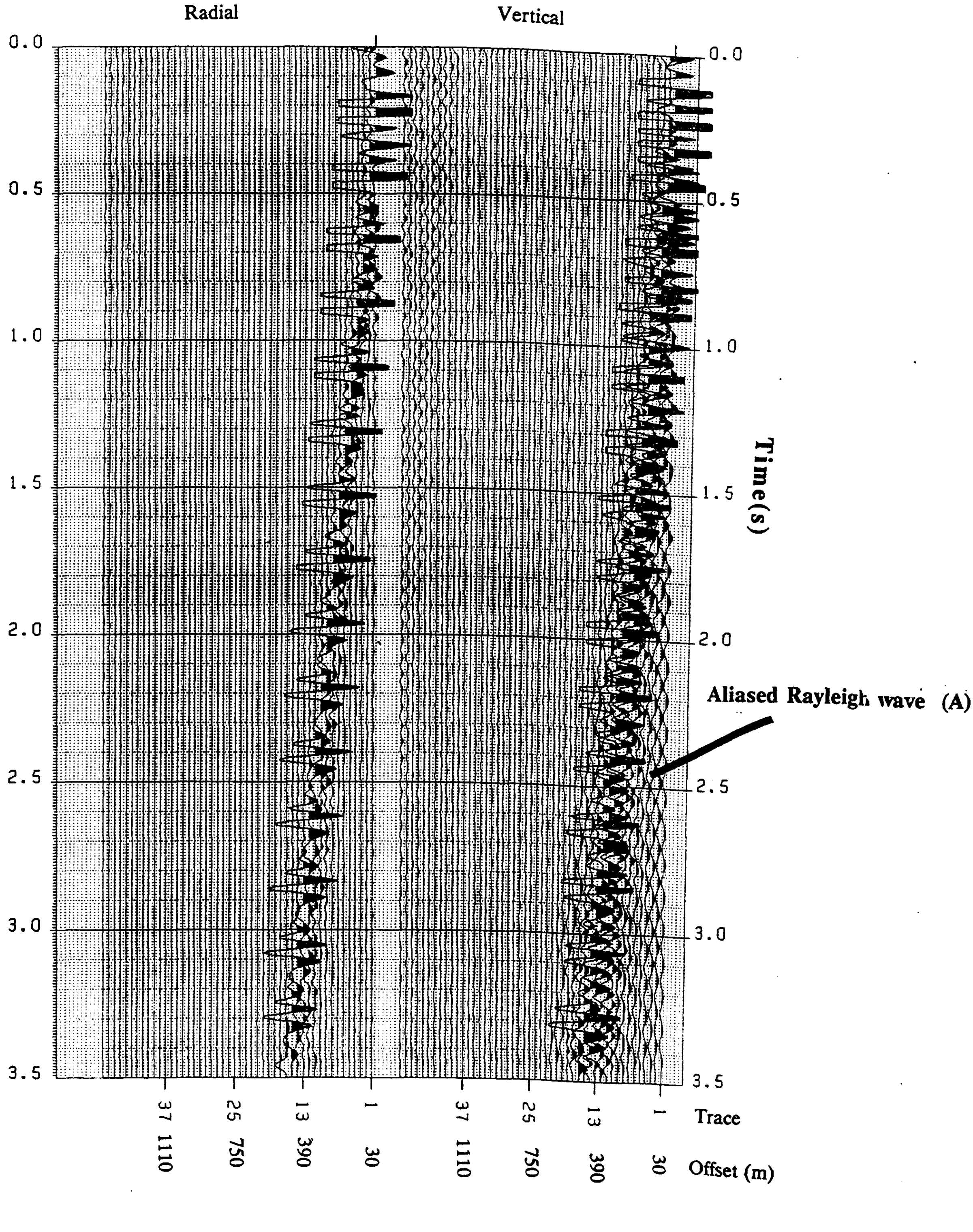

Figure 3.12 Jumping Pound model synthetic gather (Table 1.1).

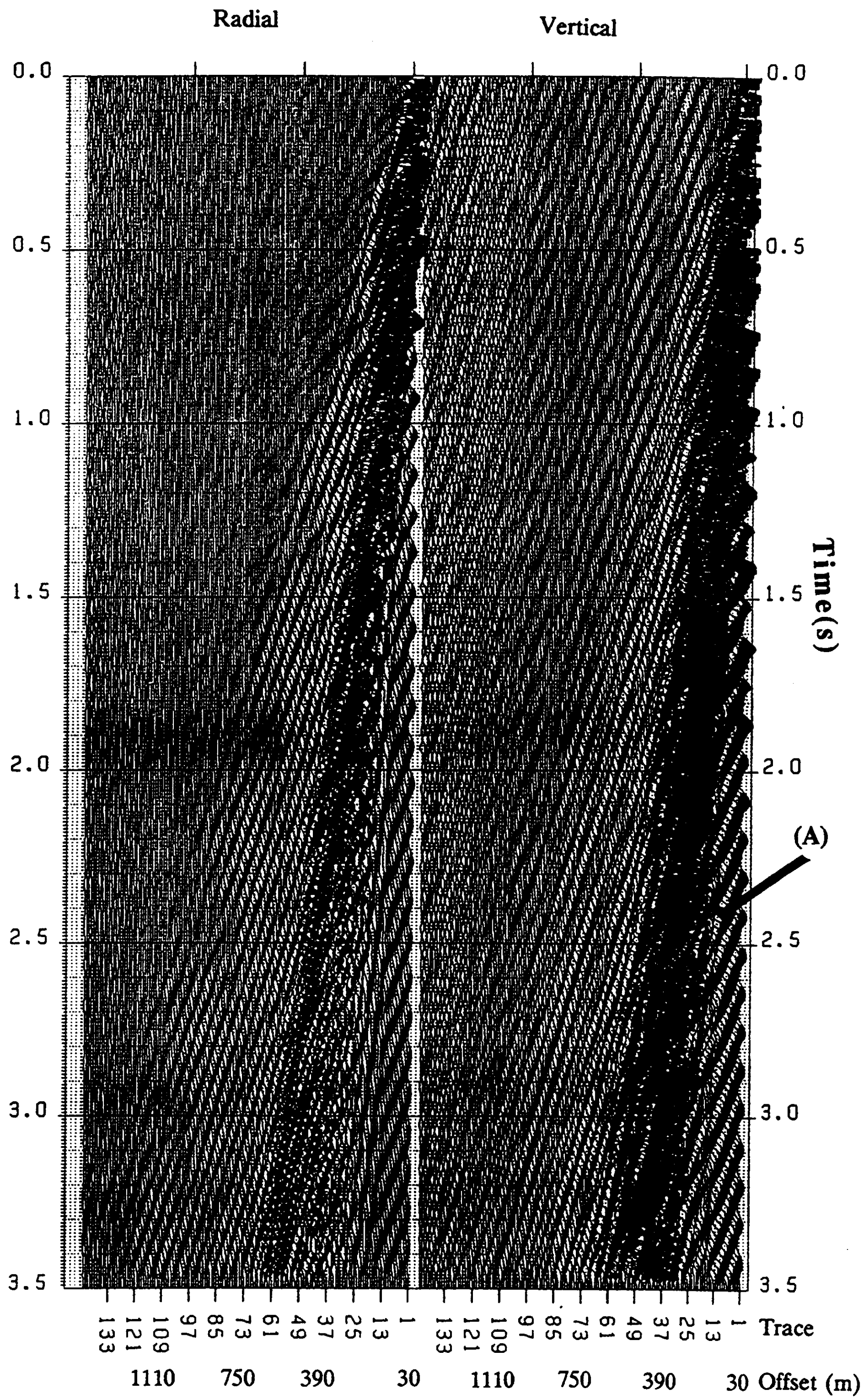

Figure 3.13 Jumping Pound model synthetic gather (Table 1.1) with 10 m group interval.

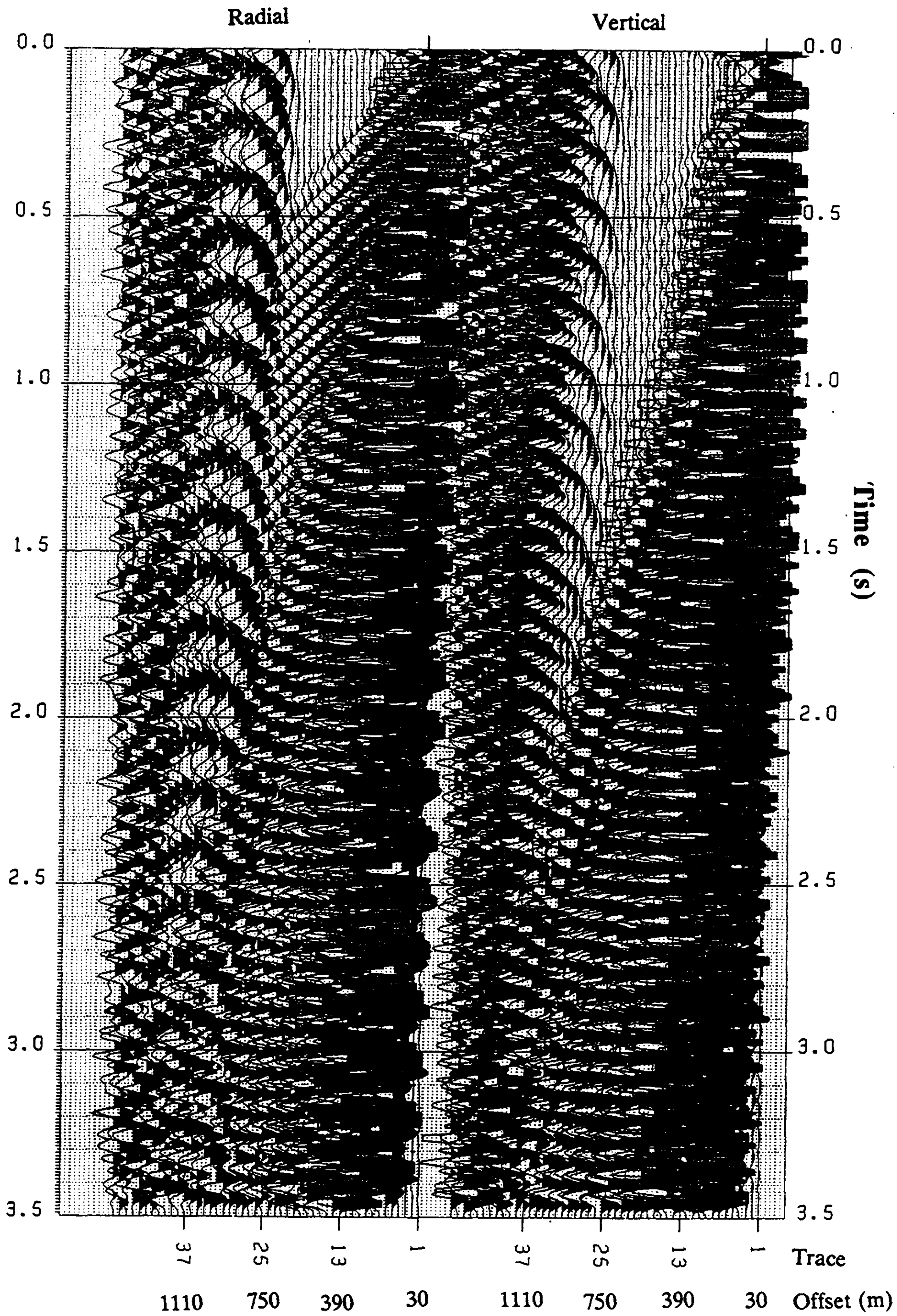

Figure 3.14 Jumping Pound model synthetic gather (Table 1.1) with a first layer thickness of only 5 meters.

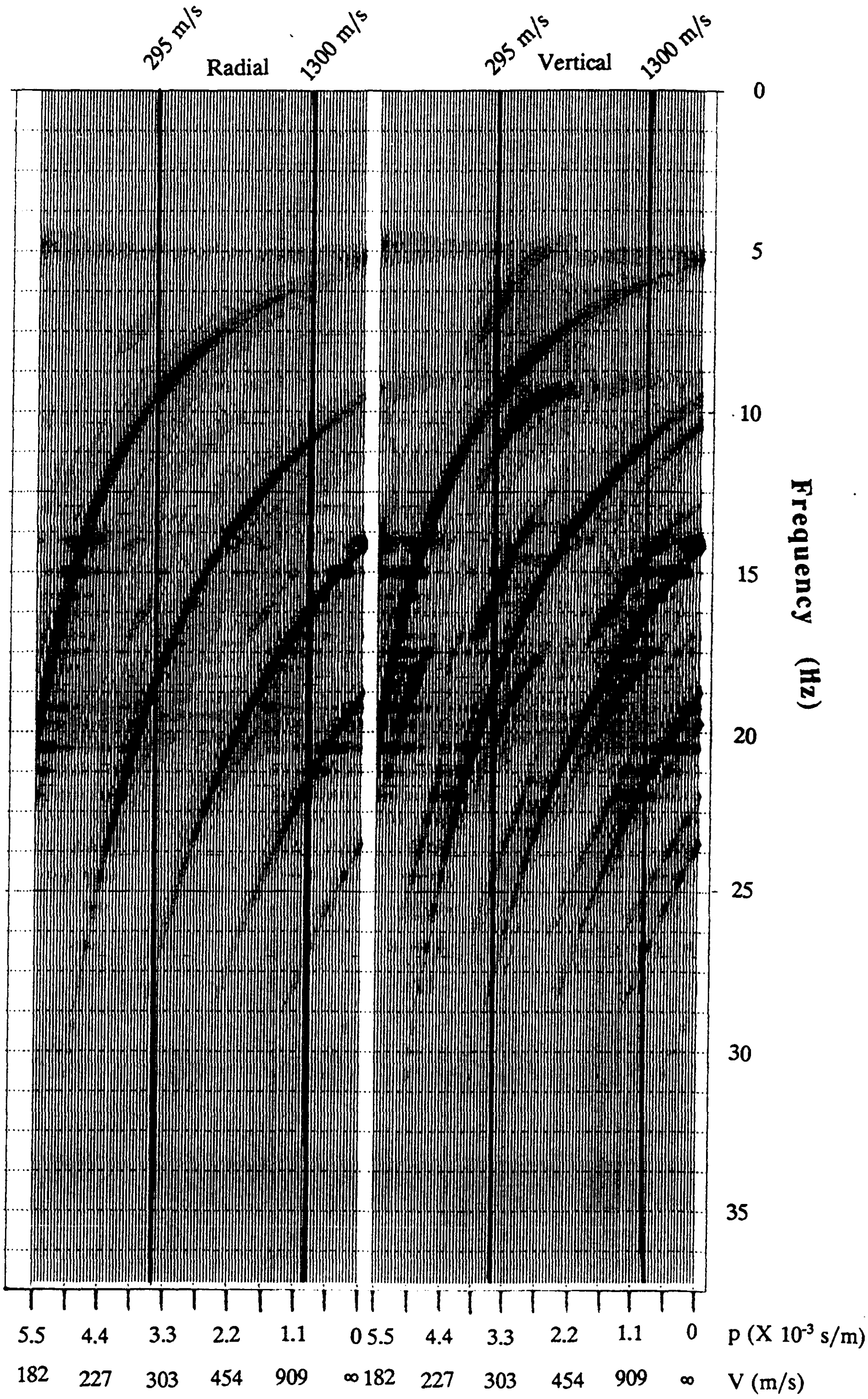

Figure 3.15 ω-p transform of the Jumping Pound model synthetic gather shown in Figure 3.12 showing dispersion curves and aliased residuals.

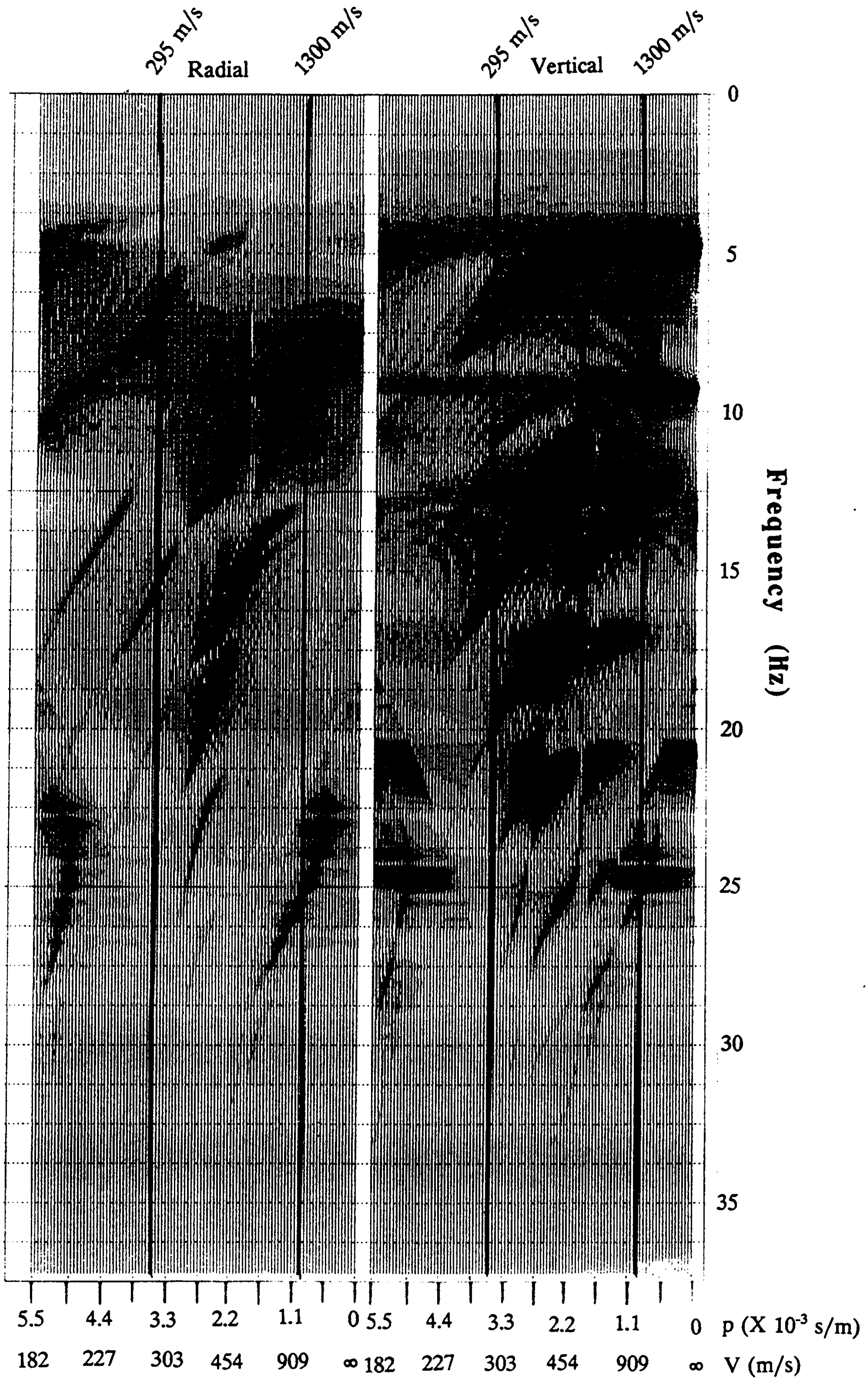

Figure 3.16 ω-p transform of the Jumping Pound model synthetic gather shown in Figure 3.13 with 5 m trace spacing.

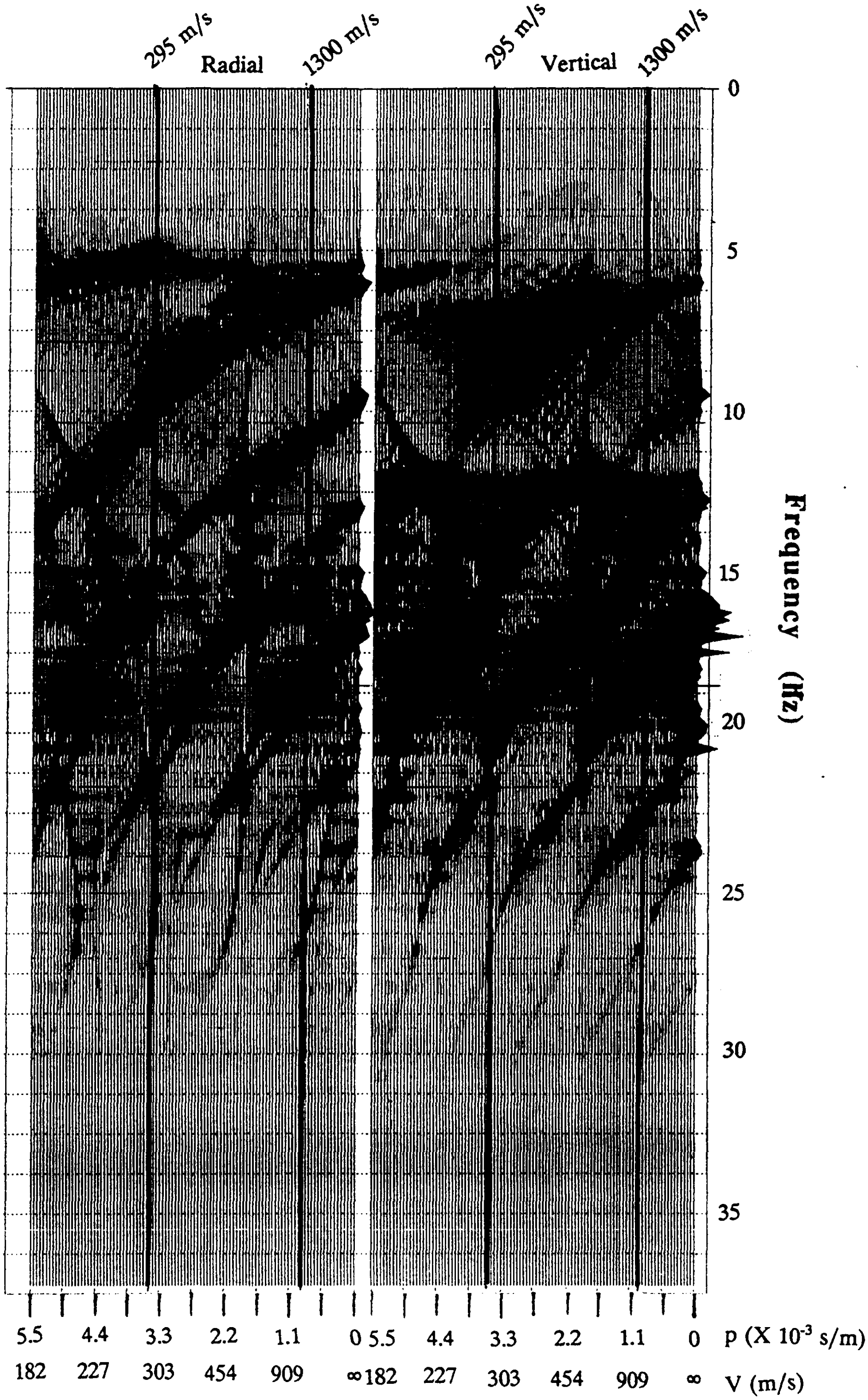

Figure 3.17 ω-p transform of Jumping Pound model synthetic gather in Figure 3.13.

Chapter 4 RAYLEIGH-WAVE FILTERING

4.1 Introduction

Earthquake seismology has historically considered surface waves as very useful signals in defining earth structure as well as seismic source mechanisms (Herrin and Goforth, 1977). Many of the techniques used in the treatment of Rayleigh waves have been developed in the context of global seismology. In earthquake seismology, the objectives are to isolate a dispersed surface wave mode from background noise consisting of body waves or secondary surface waves due to multipath transmission (Takeuchi and Saito, 1972). In exploration seismology, the surface waves are viewed as noise while the body waves are the desired signal. Some of the methods commonly used in earthquake seismology to enhance surface waves have been successfully applied in exploration seismology to remove ground roll (Saatçillar and Canitez, 1988; Herrmann and Russell,1990) and flexural ice waves (Beresford-Smith and Rango, 1988) from conventional records. The basis of these methods is in the development of a compression filter to collapse the dispersed surface waves (Boer et al, 1977).

4.2 Phase-matched filter

Based on the near-surface model and an approximate density of 2.2 gm/cm^3, the dispersion curve (Figure 4.1) was calculated using the procedures described in section 3.3.2. If the slope of the dispersion curve can be approximated by a line, a very simple phase-matched filter can be used to compress the dispersion to a bandlimited spike. A linear frequency-modulated wavelet *l(t)* is given by

$$\begin{aligned} l(t) &= \cos(\omega_c t + \frac{\Delta\omega}{2T} t^2), & -\frac{T}{2} \le t \le \frac{T}{2} \\ &=0, & \textit{otherwise.} \end{aligned} \tag{4.1}$$

where T is the time length of the wavelet, ω_c is the carrier frequency and $\Delta\omega$ is the modulation bandwidth (after Saatçilar and Canitez, 1988).

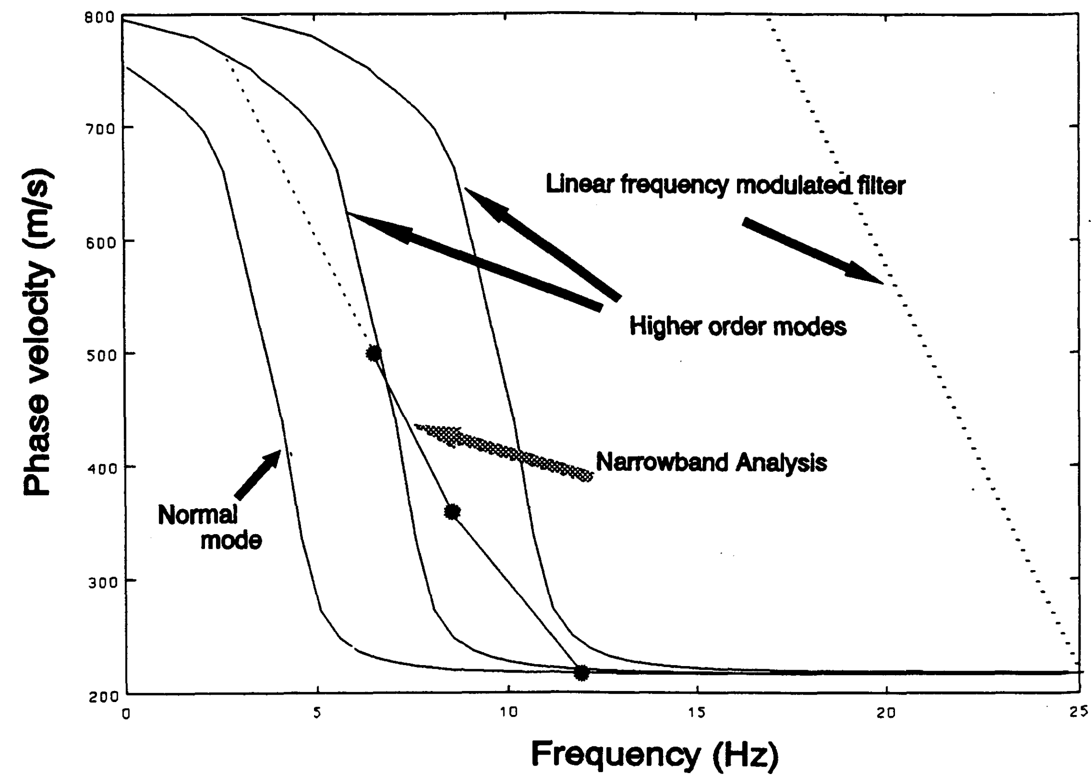

Figure 4.1 Dispersion curve for Springbank near-surface model

The Fourier transform of *l(t)* is given by:

$$L(\omega)=|A_L(\omega)|e^{-i(\phi_0+\phi(\omega))}, \tag{4.2}$$

where

$$\phi(\omega)=\frac{-\Delta\omega T}{2}(\frac{\omega_c-\omega}{\Delta\omega})^2 \tag{4.3}$$

$A_L(\omega)$ is the amplitude spectrum and ϕ_0 is the initial phase. The implied initial phase for the wavelet given by eq. (4.1) is $\phi_0=-\pi(2\omega_c-\omega)T/8$ (Aldridge, 1992). This means the phase is zero and the wavelet has a relative maximum at the half duration time ($T/2$). The desired matched filter, *mf(t)*, will compress the linear frequency modulated (LFM) wavelet defined in eq. (4.1) to a single spike at the half duration time by matching the phase dispersion. The wavelet *mf(t)* is simply a time reversed, time-delayed, and scaled version of the LFM wavelet given as:

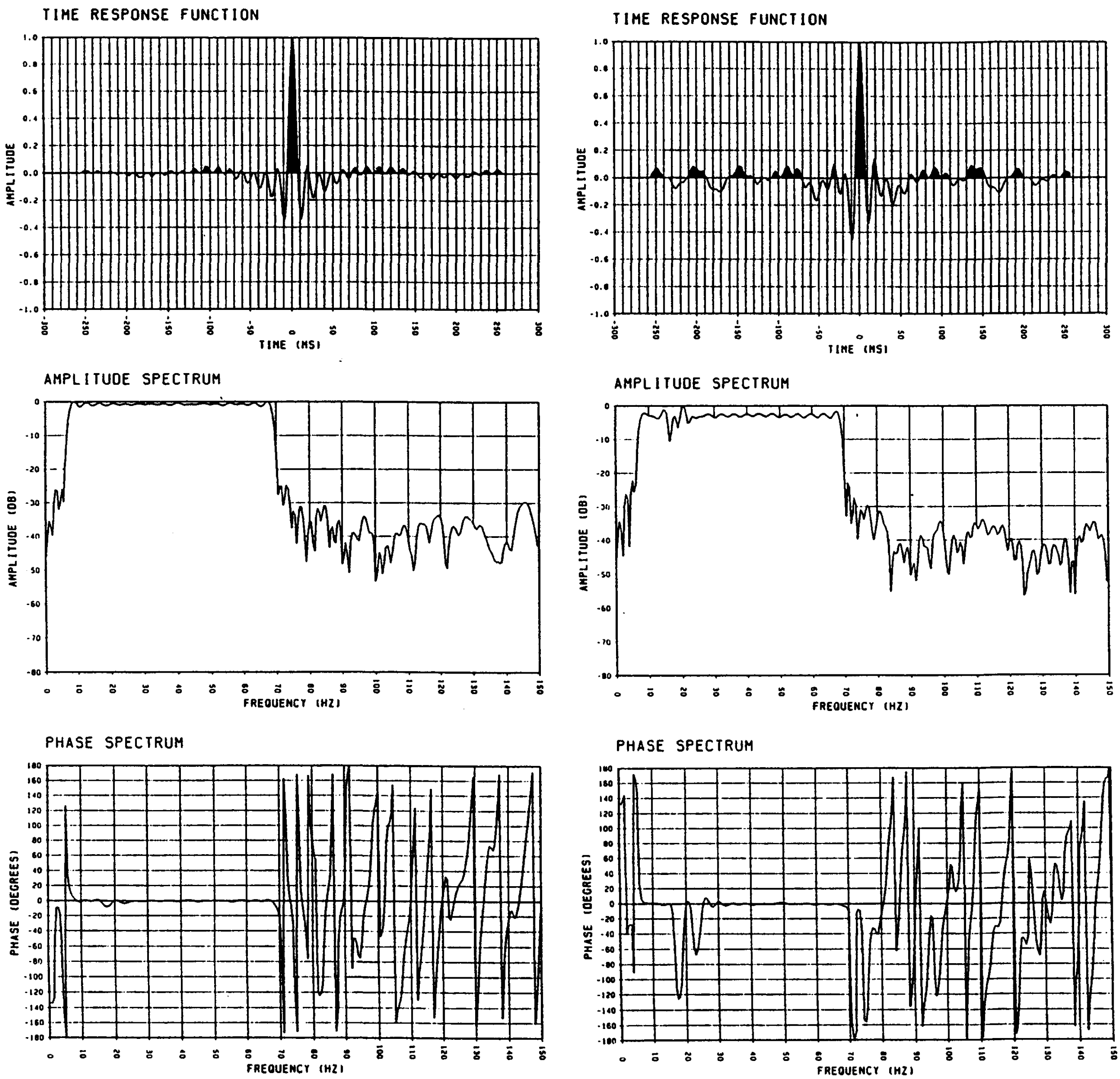

(a) (b)

Figure 4.2 LMF filter with amplitude spectrum bandwidth of 8-70 Hz and phase compression over 8-30 Hz a) at 10 m offset and b) at 160 m offset.

$$mf(t) = k * l(\Gamma - t). \tag{4.4}$$

where k is the amplitude and Γ is the time delay. Neglecting the time delay ($\Gamma = 0$) and using unit amplitude ($k = 1.0$) the Fourier transform of the matched filter is where L^* is the complex conjugate of the Fourier transform of l(t) (Turin, 1960).

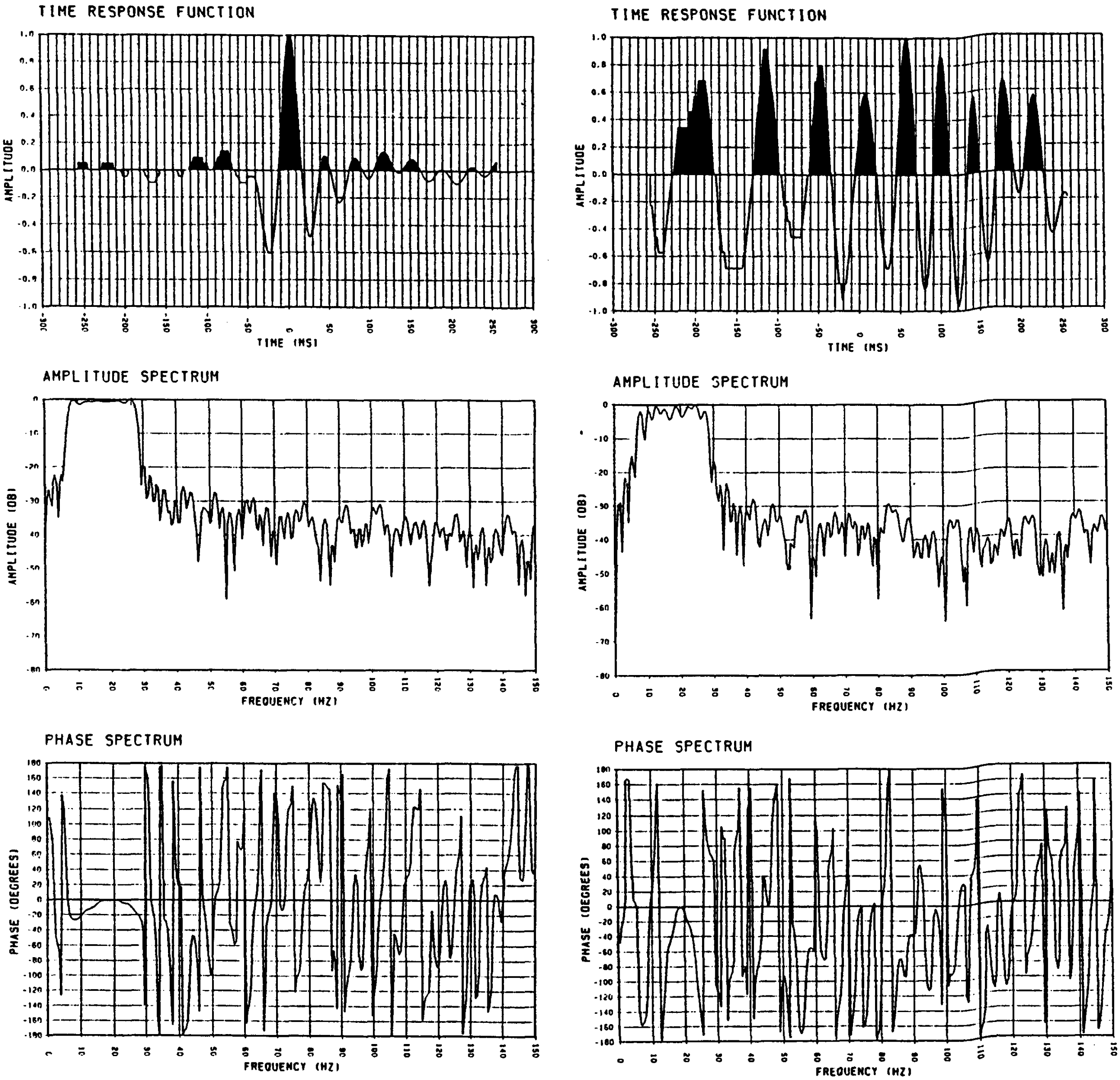

(a) (b)

Figure 4.3 LMF filter operator with frequency bandwidth equal to the bandwidth of the phase a) at 10 m offset, and b) at 160 m offset.

$$MF(\omega)=L^*(\omega)=|MF(\omega)|e^{i[\frac{\Delta\omega T}{2}(\frac{\omega_c-\omega}{\Delta\omega})^2]} \tag{4.5}$$

The matched filter is designed in the frequency domain and its amplitude spectrum is set to unity over the frequency bandwidth of the signal. Outside this bandwidth the amplitude is set to zero. This assures that the inverse application of this filter after multichannel *f-k* or median *f-k* filter does not affect the amplitude spectrum of the data and operates only on the linear phase dispersion within the desired frequency band-limits. Figure 4.2 shows an operator with a phase compression bandwidth of 8-30 Hz but an increased amplitude spectrum of 8-70 Hz. Figure 4.3 depicts an operator with amplitude spectrum equal to the phase spectrum frequency bandwidth (8-30 Hz). These phase spectra depict zero phase at the 1/2 duration frequency. Note that the phase dispersion at the 160 m offset is greater than at the nearer 10 m offset.

4.3 Dispersion Estimation

The ability of the matched filter to compress dispersive linear noise is dependent on accurate dispersion estimation. The phase velocity dispersion curve is primarily dependent on rapidly varying near-surface shear-wave velocities and layer thicknesses. To obtain an accurate estimate, the phase velocity analysis must be performed on a large number of traces. Therefore, the estimate is an average over a distance that is almost equal to the spread length, in most cases. Three methods of dispersion analysis have been implemented to attempt to evaluate the most practical approximation of the phase matched filter. In earthquake seismology, narrowband analysis of multistation cross-correlations can accurately estimate the phase velocity curves within the low-frequency or long-wavelength signals observed (Dziewonksi and Hales, 1972). Shear-wave refraction analysis can deliver an accurate estimate of the near-surface lithology including velocities and thicknesses of the first two or three layers (Russell, 1989; Lawton, 1990). Finally, the wavefield transformation to map the shot gathers directly into a frequency-velocity space where amplitude maxima represent dispersive Rayleigh waves (McMechan and Yedlin, 1981).

In cases where the thicknesses are large relative to recordable frequencies, it has been shown that the normal mode may be outside the frequency range of recorded data. In these cases, the higher modes are represented by the large-amplitude Rayleigh waves observed on the shot records.

4.3.1 Narrowband filtering

For increasing offsets (x) the time duration of the LMF will increase and is limited at low frequencies by the second layer velocity (V_2) and at higher frequencies

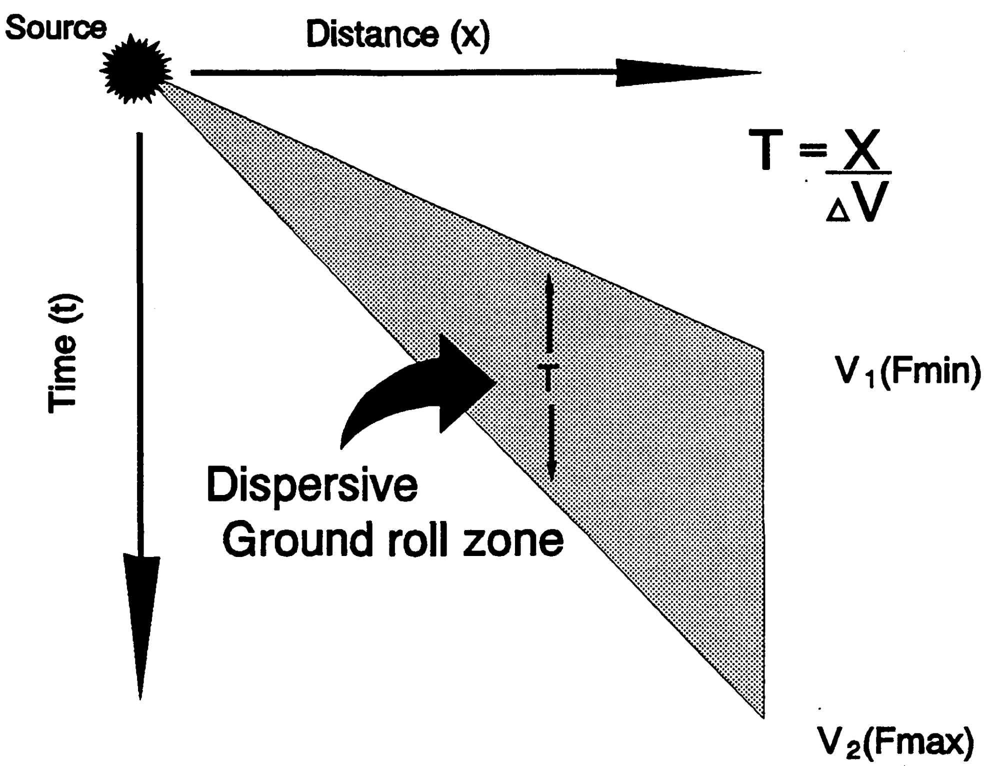

Figure 4.4 Varying time duration of dispersive ground roll zone.

by the propagating layer velocity (V_1). Referring to Figure 4.4, the time duration (T) of the LMF can be expressed as a function of offset and velocity difference (ΔV). If the phase velocity is measured on field records for distinct frequencies obtained by narrowband filtering, it is possible to estimate the dispersion parameters (V_1, V_2, $\Delta\omega$). This method has been used to estimate dispersion curves to invert for near-surface shear-wave thicknesses and velocities (Mari, 1984, Szelwis and Behle, 1987).

To express equation (4.4) in terms of offset becomes

$$MF(\omega)=L^{*}(\omega)=|MF(\omega)|e^{i[\frac{x}{2\Delta V}\frac{(\omega_c-\omega)^2}{\Delta\omega}]} \tag{4.6}$$

where ΔV is the difference in velocity.

The phase velocity dispersion curve can be obtained by measuring the apparent velocities of Rayleigh waves on various narrow band filter panels. This phase velocity analysis is done assuming that phase velocity decreases with frequency At the maximum frequency V_1 and the minimum frequency V_2. Figure 4.1 depicts the result of this analysis of the narrow band filter panels in Figures 4.5.

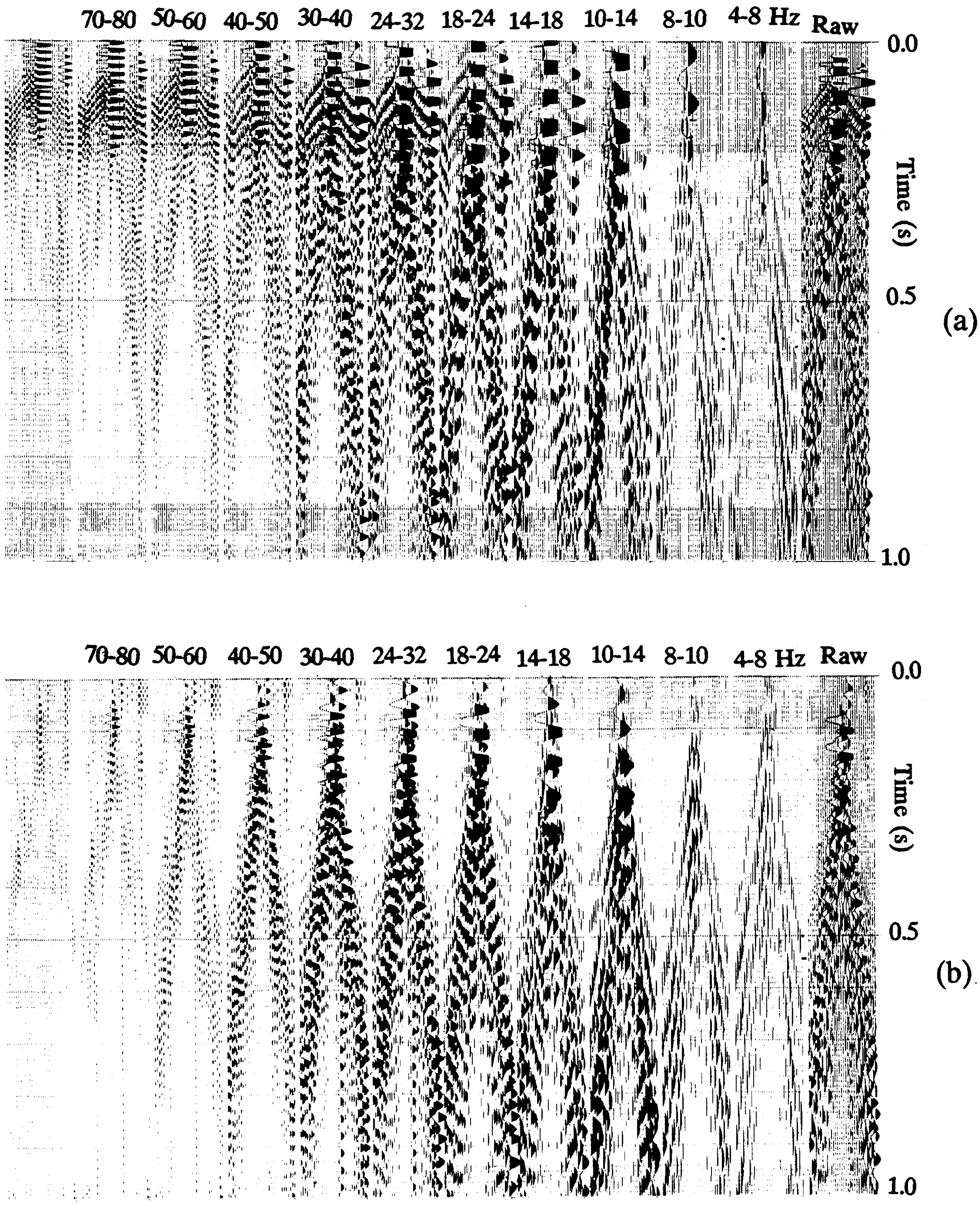

Figure 4.5 Springbank FS91-1 vertical a) and radial b) component, narrow-band, filter panels.

4.3.2 Refraction Analysis

Source-generated shear-wave refractions recorded on the radial channel can be picked on the multicomponent shot records (Lawton, 1990). Typical examples of

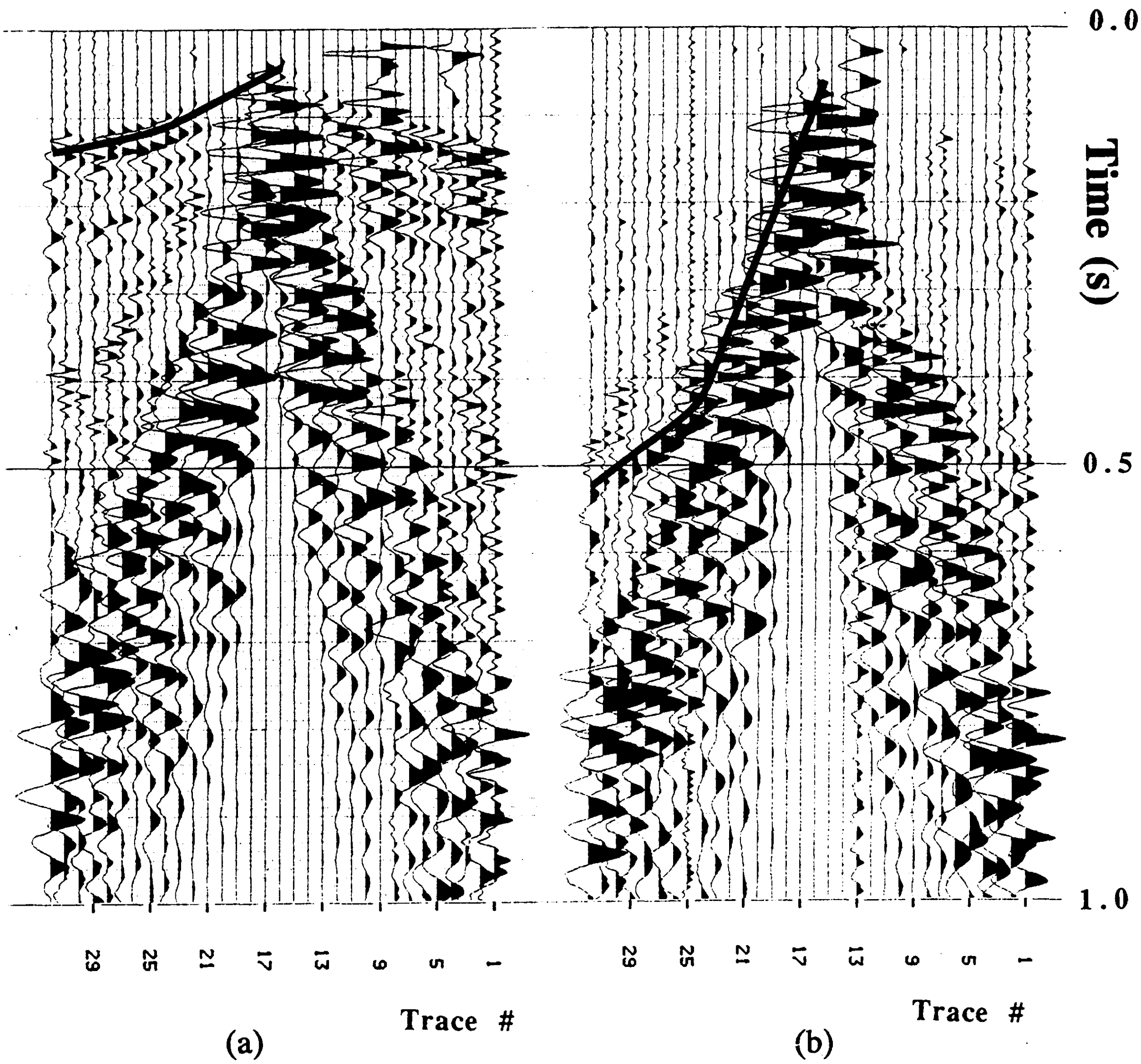

Figure 4.6 FS91-1 shot gather examples a) Vertical component with refracted compressional P-waves b) Radial shear component showing refracted shear waves.

the raw shot gathers used to pick the shear-wave first arrivals are depicted in Figure 4.6. These firstbreak picks can then be interpreted, in this case using the GLI

(Hampson and Russell, 1984) method of inversion. The inverted first breaks and interpreted near-surface models (layer thicknesses and velocities) are shown in Figure 4.7 and 4.8. A general model based on this interpretation was shown in Figure 3.1 in the previous chapter. Near-surface Poisson's ratios are all greater than 0.4, similar to the observations of Lawton (1990) in the nearby area of Jumping Pound, Alberta (Twp 26, Rge 5W5) as shown in Figure 4.9.

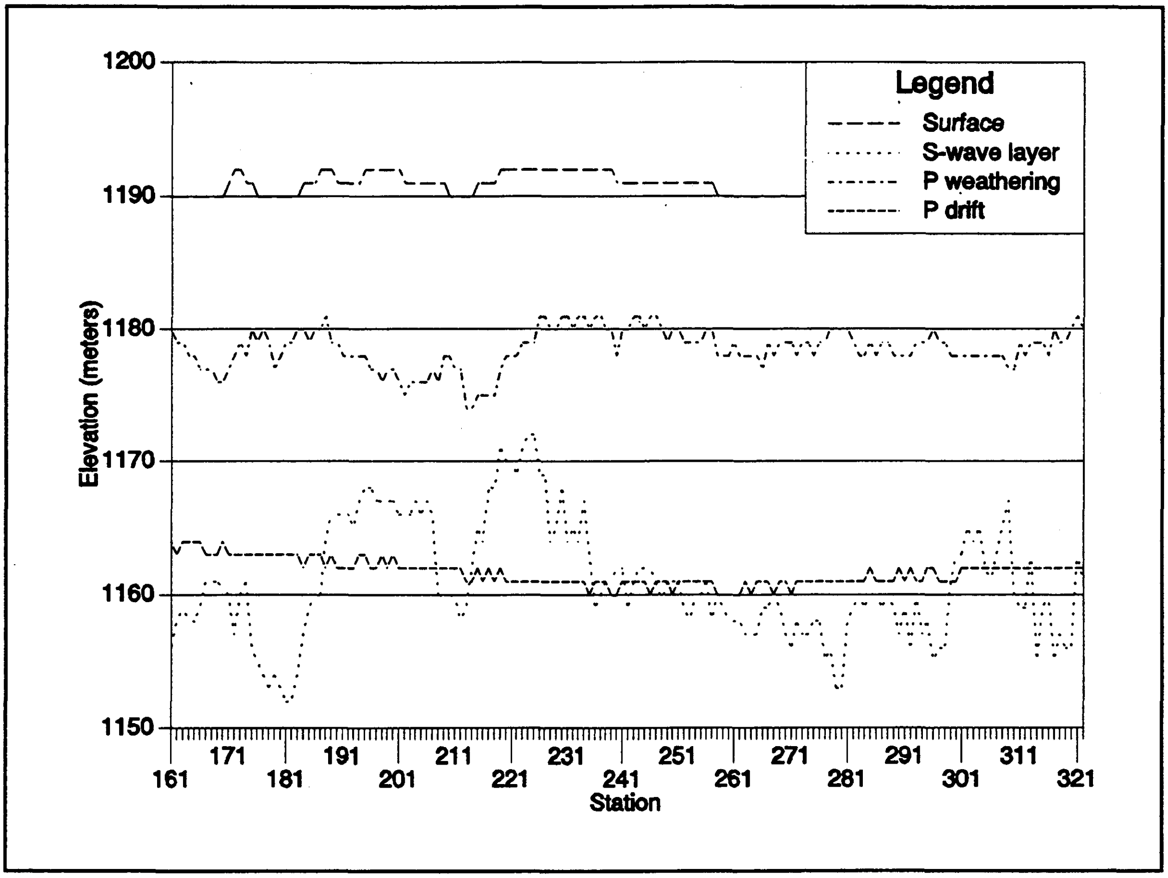

Figure 4.7 Elevations interpreted from refraction analysis for FS91-1 line.

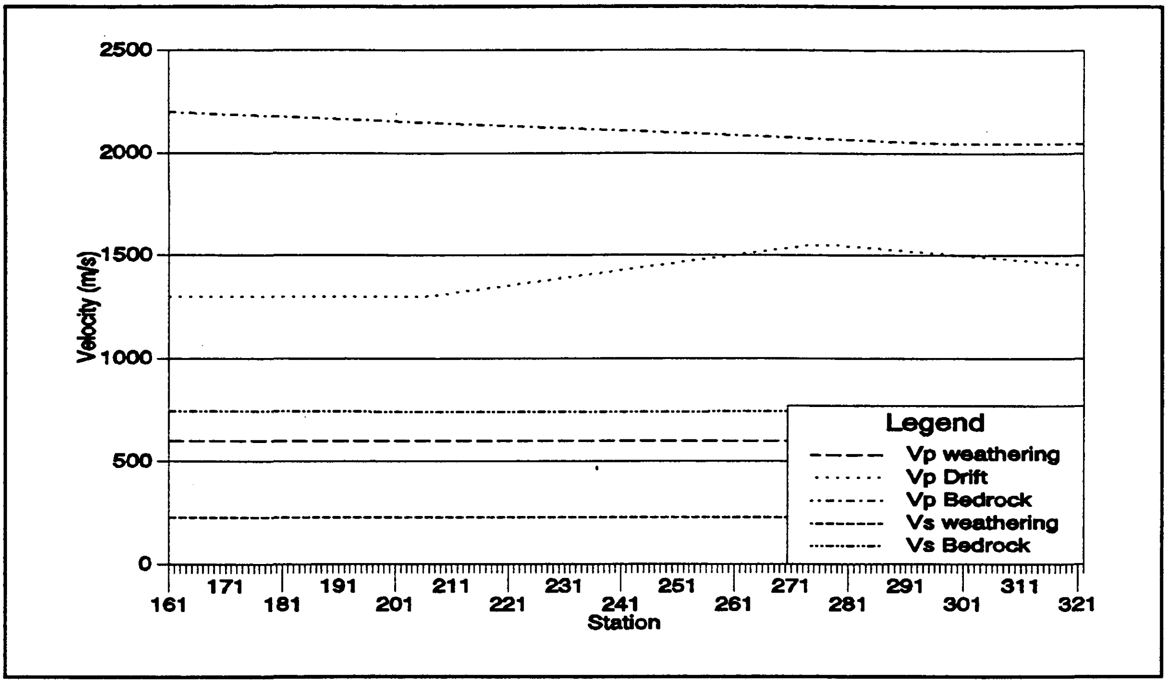

Figure 4.8 Velocities interpreted from refraction analysis of FS91-1 line.

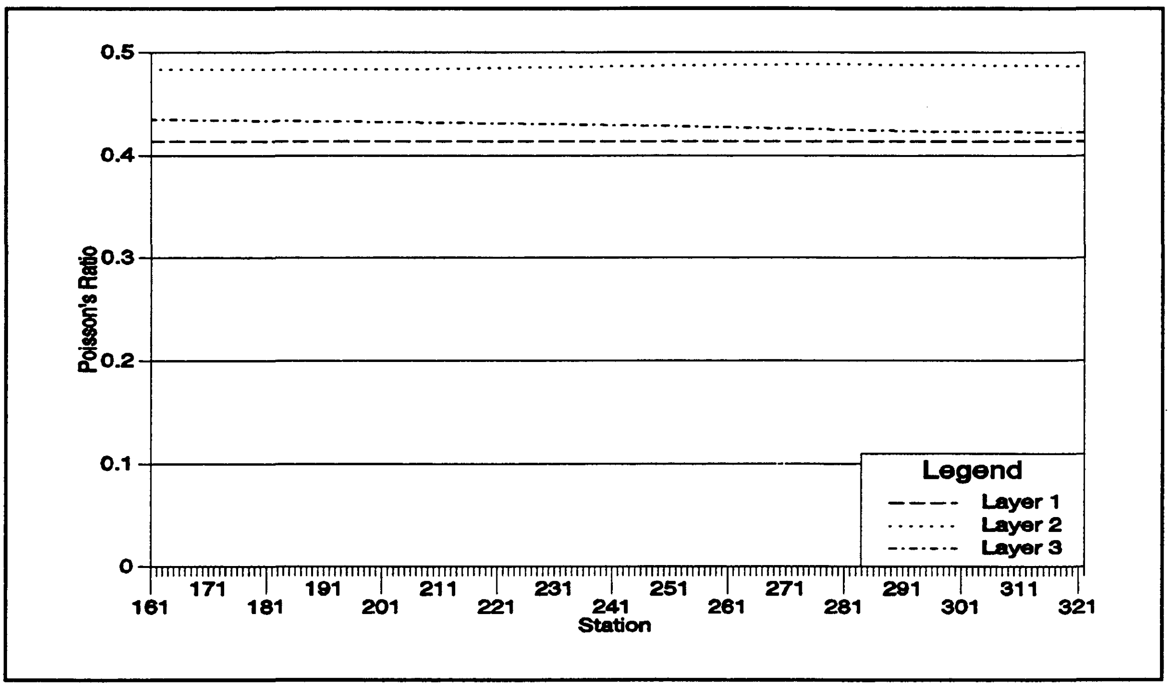

Figure 4.9 Poisson's ratio for the first three refraction layers of FS91-1.

4.3.3 ω-p transform analysis

Three shot gathers, off the ends and at the centre of the receiver spread, are shown in Figures 4.10 (radial component) and 4.11 (vertical component) for the Springbank FS91-1 data set. Note the vertical-component display is plotted at a time scale that is 1.5 times the radial component to approximately align the P-P reflection events with the P-SV events. Single geophones and a surface shot (Betsy seisgun) resulted in significant surface wave energy. The ground-surface elevations (Figure 4.8 and 4.9) were relatively flat over the length of the line, but delays in the refracted arrivals of as much as 20 ms within short distances are indicative of a rapidly varying surficial layer thickness or velocity. The assumption of flat, homogeneous layers within a single spread is required for the ω-p analysis to be useful. The refraction analysis indicates variations in the near-surface shear-wave layer of as much as 15 m within a single shot record spread.

After determining the shear-wave velocity bounds from refraction analysis the shot gathers were transformed to the ω-p domain. A factor of $\sqrt{x}$ was used to compensate for ground roll attenuation. A slant stack from 0-900 ms moveout at 160 m offset ($\Delta p = 10$ ms/trace) was followed by a 1-D Fourier transform in τ to obtain the ω-p stack. This process was applied to both the radial and vertical channels and their subsequent amplitude spectra were summed together to minimize noise (Figure 4.12). Note the ω-p amplitudes for the end on shot gathers (36 and 46) are larger than the split spread gather (41). This is because the maximum offset for shot gather 41 is half (160 m) that of 36 and 46 (320 m). The known shear-wave velocities, on the basis of refraction analysis, are plotted in Figure 4.12. The bandwidth of the ground roll is estimated to be 4-21 Hz on the basis of the narrowband filter panels (Figures 4.5 and 4.6). Based on the near-surface model (Figure 4.1) the normal mode should be seen within the 3-6 Hz range within which very little energy is observed on the ω-p plot. Higher modes within the 12-20 Hz frequency range might be inferred as shown, but a dispersion compression filter could not be designed on the basis of this display because no single amplitude peak within the velocity bounds 230-800 m/s could be isolated.

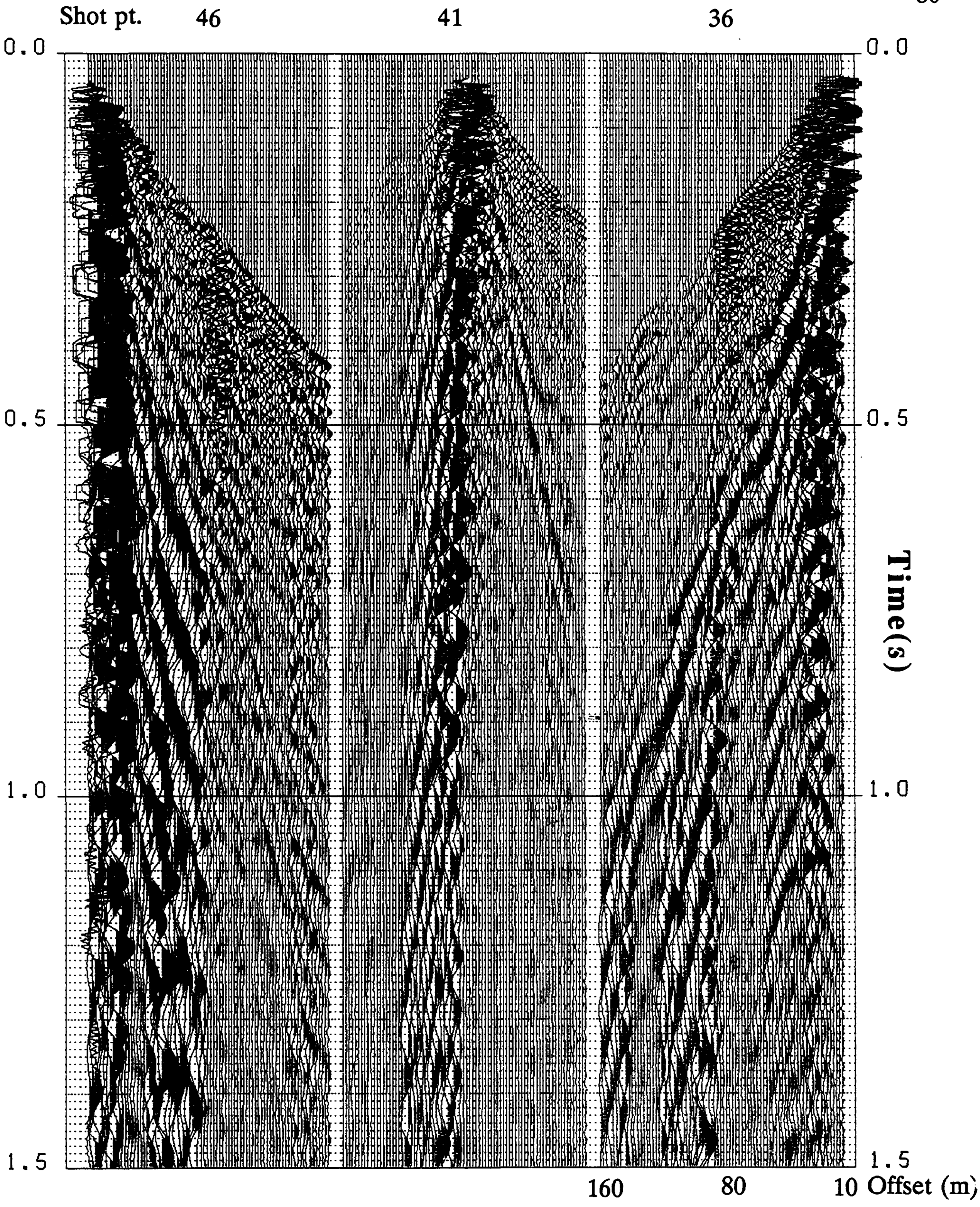

Figure 4.10 FS91-1 Radial component raw shot gathers 36, 41 and 46.

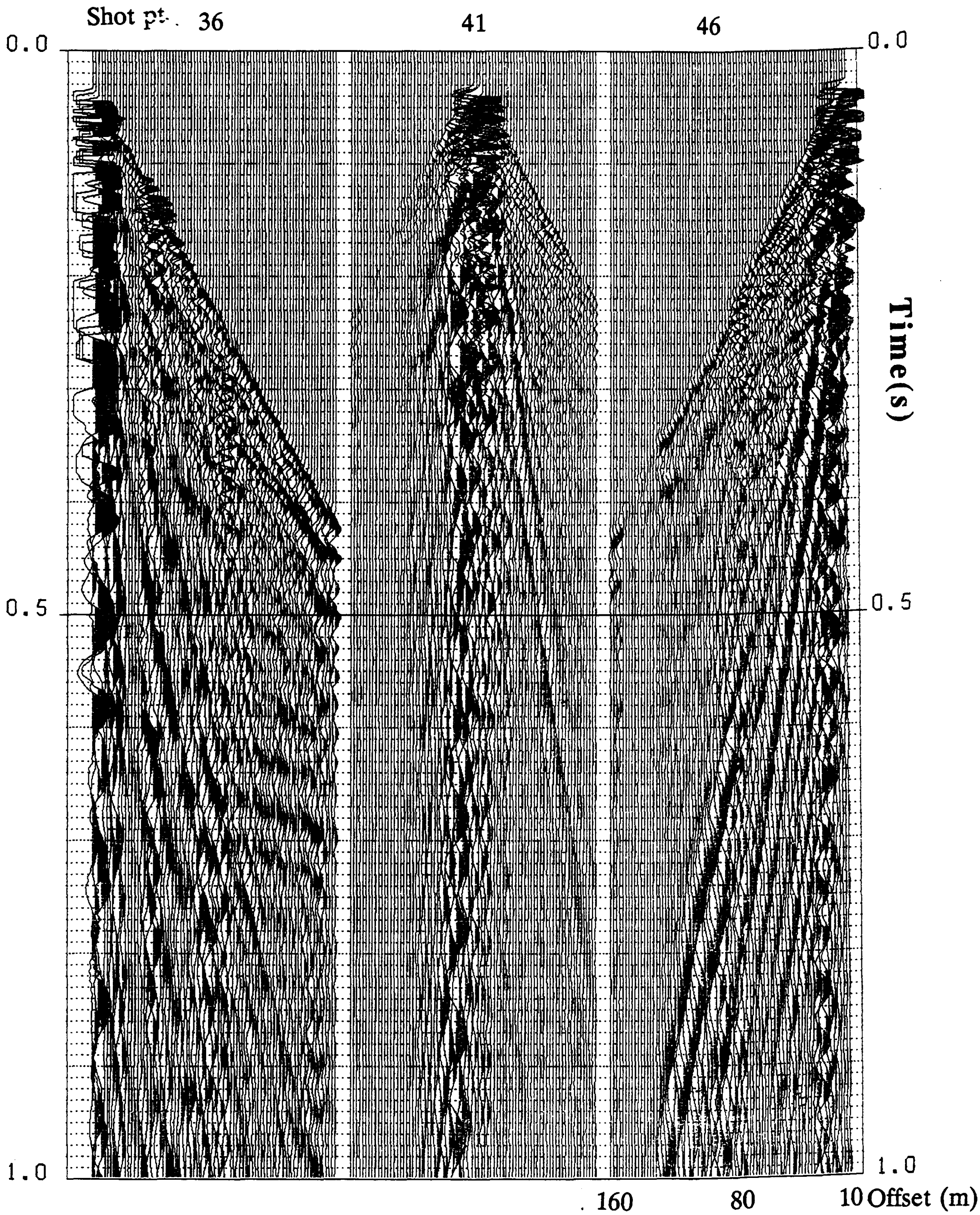

Figure 4.11 FS91-1 Vertical component raw shot gathers 36, 41 and 46.

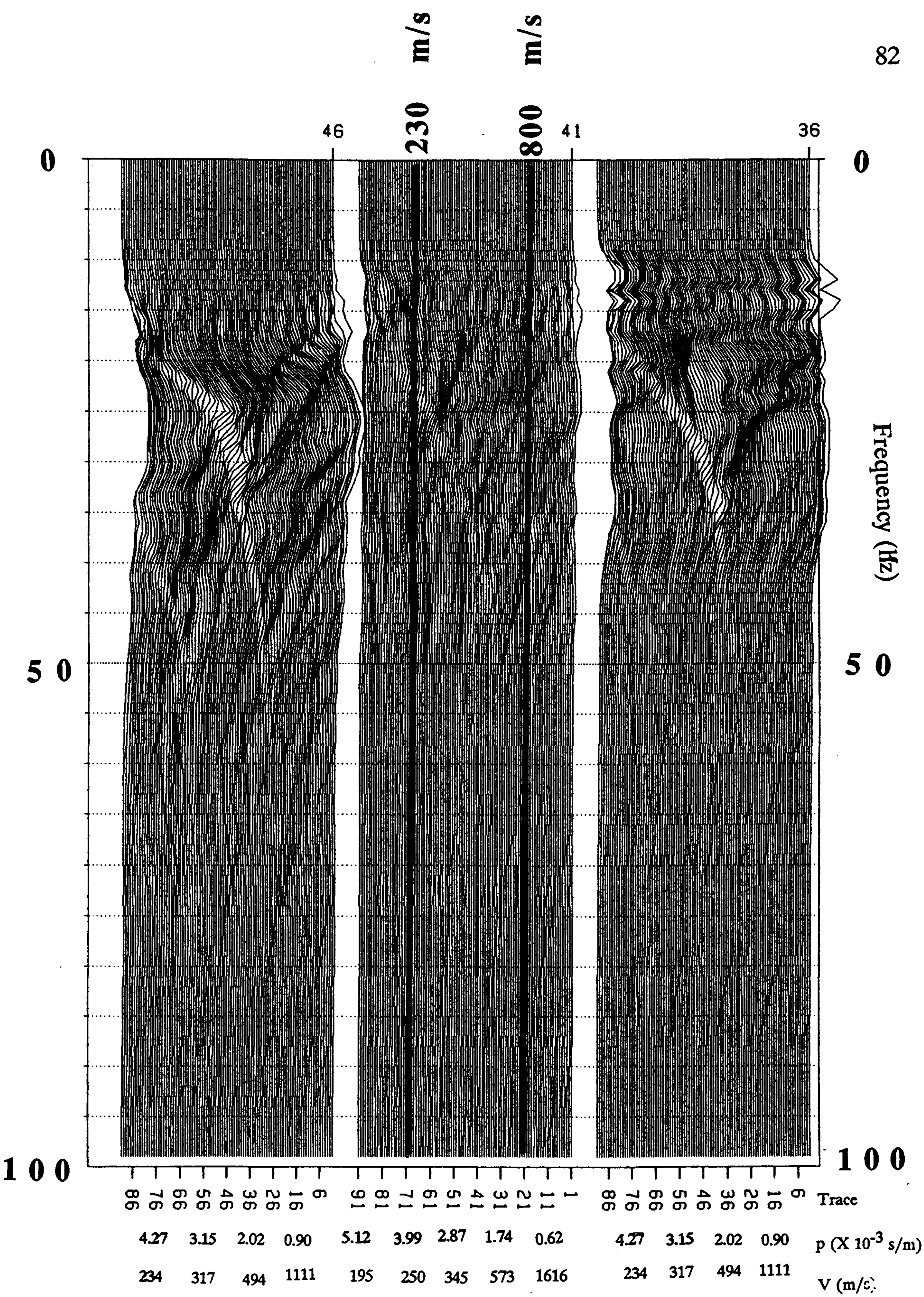

Figure 4.12 ω-p mapping of shot gathers 36, 41, and 46.

4.4 Synthetic data

To investigate the effect of the linear frequency modulated (LFM) compression operator on the multichannel f-k and median *f-k* filters, a synthetic shot gather with LFM surface waves was generated (Figure 4.13). The frequency bandwidth of the ground roll is 8-30 Hz and that of the reflections 10-60 Hz. The four reflection events were generated by inserting spikes at delay times given by the hyperbolic velocity equation using velocities from FS91-1, with an approximate offset varying amplitude and filtered with a 10 to 60 Hz bandpass filter. A LFM, bandlimited wavelet was generated with equation 4.1, with T is given by the difference in velocity as per Figure 4.4. The offset dependent compression operators for each trace within the shot gather are convolved before the multichannel filters (Figure 4.13 (d)). The results of *f-k* and median *f-k* filtering with and without the LFM compression, with a 256 ms maximum length operator, are shown if Figure 4.13. The dispersive surface waves are compressed to a single dipping event without degrading the reflection events. The dip filters were designed to remove dips greater an 8 ms/trace or velocities less than 1250 m/s.

The *f-k* domain results are displayed without compression in Figure 4.14 and with compression in Figure 4.15. By comparing the input *f-k* plot (Figure 4.14 (a)) to the compressed *f-k* plot (Figure 4.15 (a)) it is observed that the compression operator forces the aliased dispersive noise to a single dip of 500 m/s. Also a small portion of the negative dip greater at greater than 25 Hz is moved to the positive dip at lower frequency. The *f-k* filter with or without compression are very similar as observed in both the time domain plots and the *f-k* space. However, dramatic improvements in the ability of the median *f-k* filter to remove the aliased dip can be achieved by applying the compression operator pre-median *f-k*. The median *f-k* filter does not remove positive dip angles greater than 8 ms/trace as effectively as the *f-k* filter. The median *f-k* filter benefits from the surface wave compression primarily due to its ability to remove isolated aliased dips while less effectively removing dispersive aliased dips.

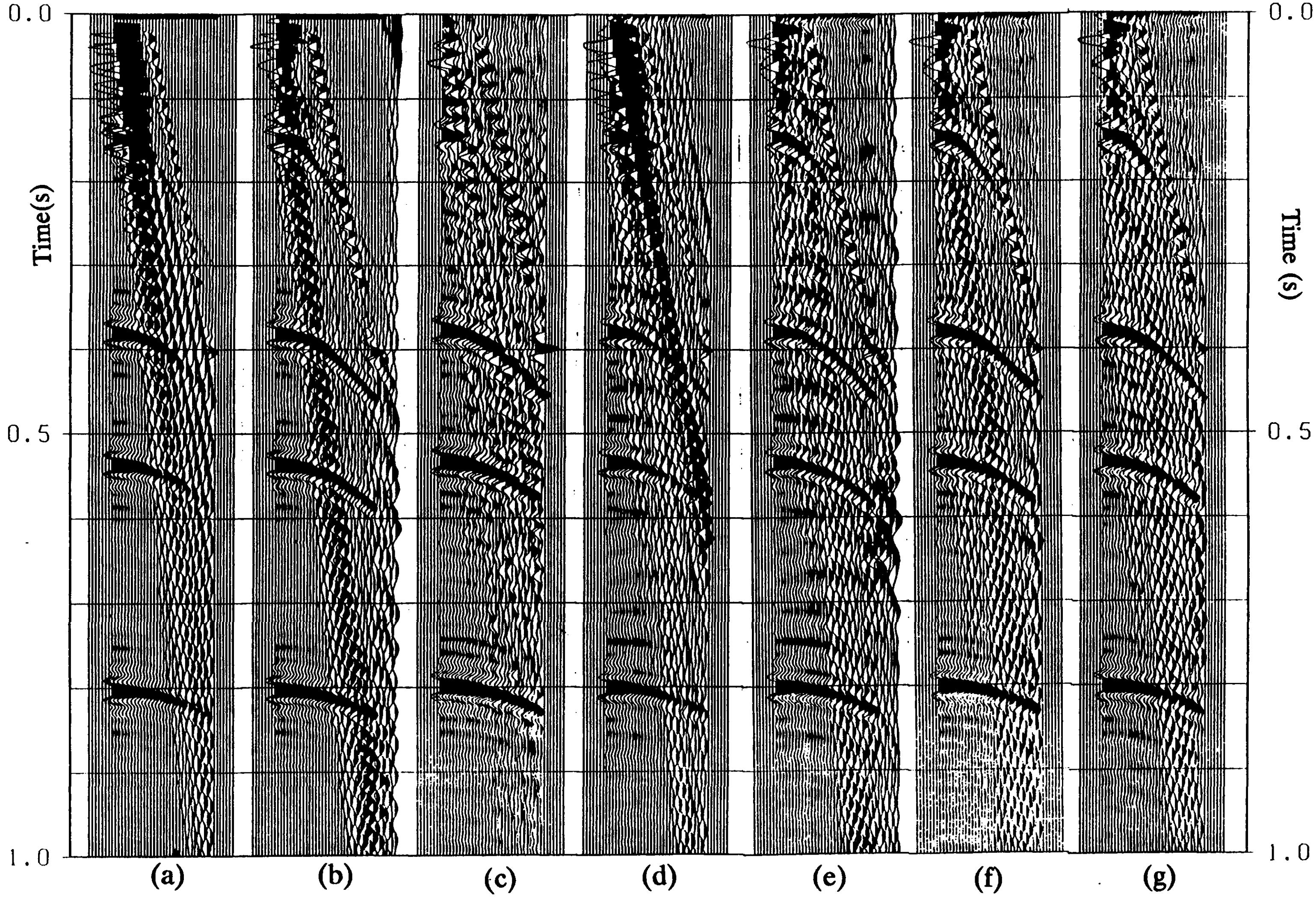

Figure 4.13. Synthetic shot gather with LFM surface waves (8-30 hz). a) input gather, b) after f-k filter, c) after median f-k filter, d) after LFM compression, e) f-k filter applied to d), f) LFM decompression of e), and g) median f-k as in f).

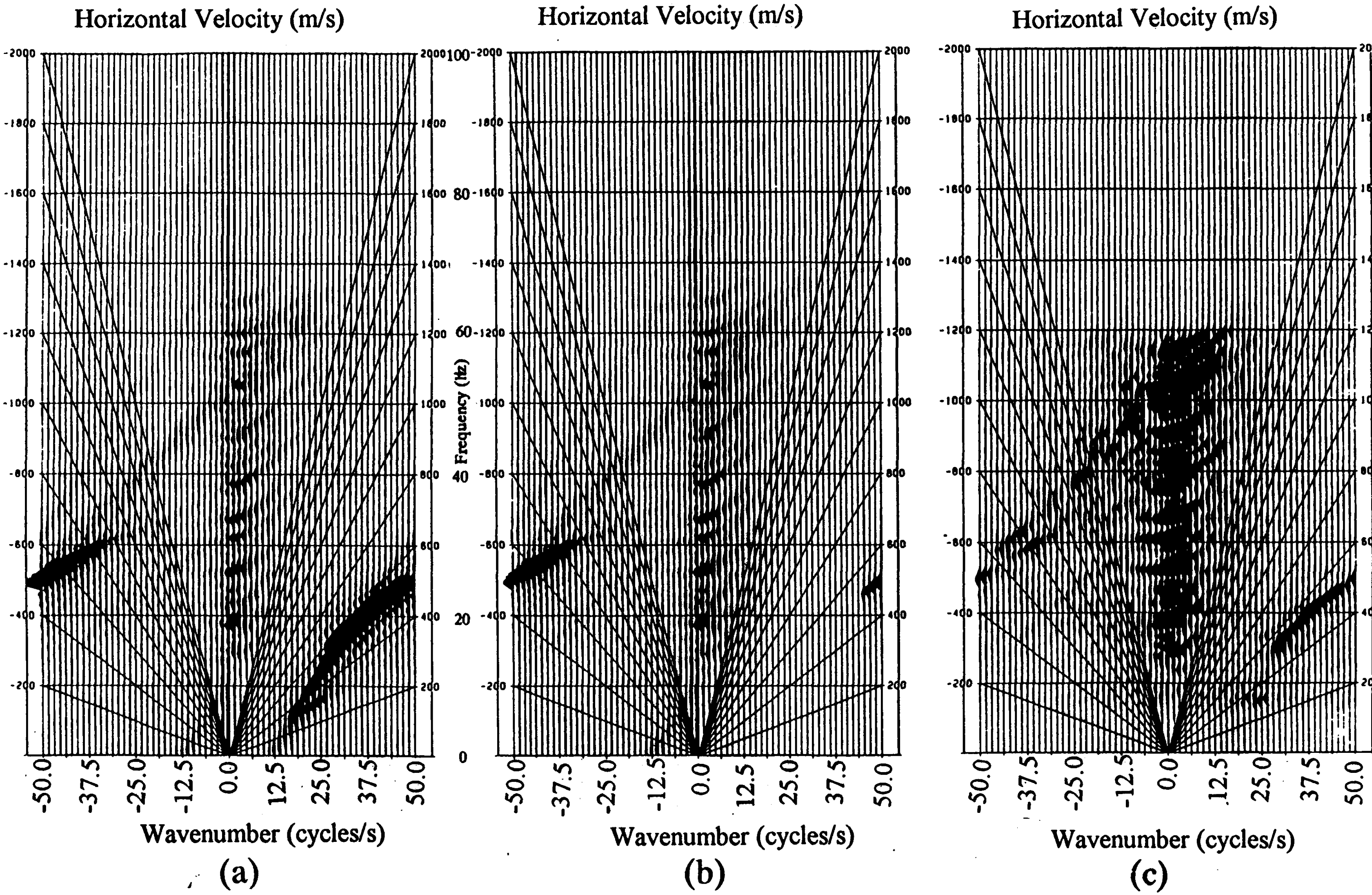

Figure 4.14 f-k transform of synthetic shot gather a) input gather, b) f-k filter (without LMF compression), and c) median f-k (without LMF compression).

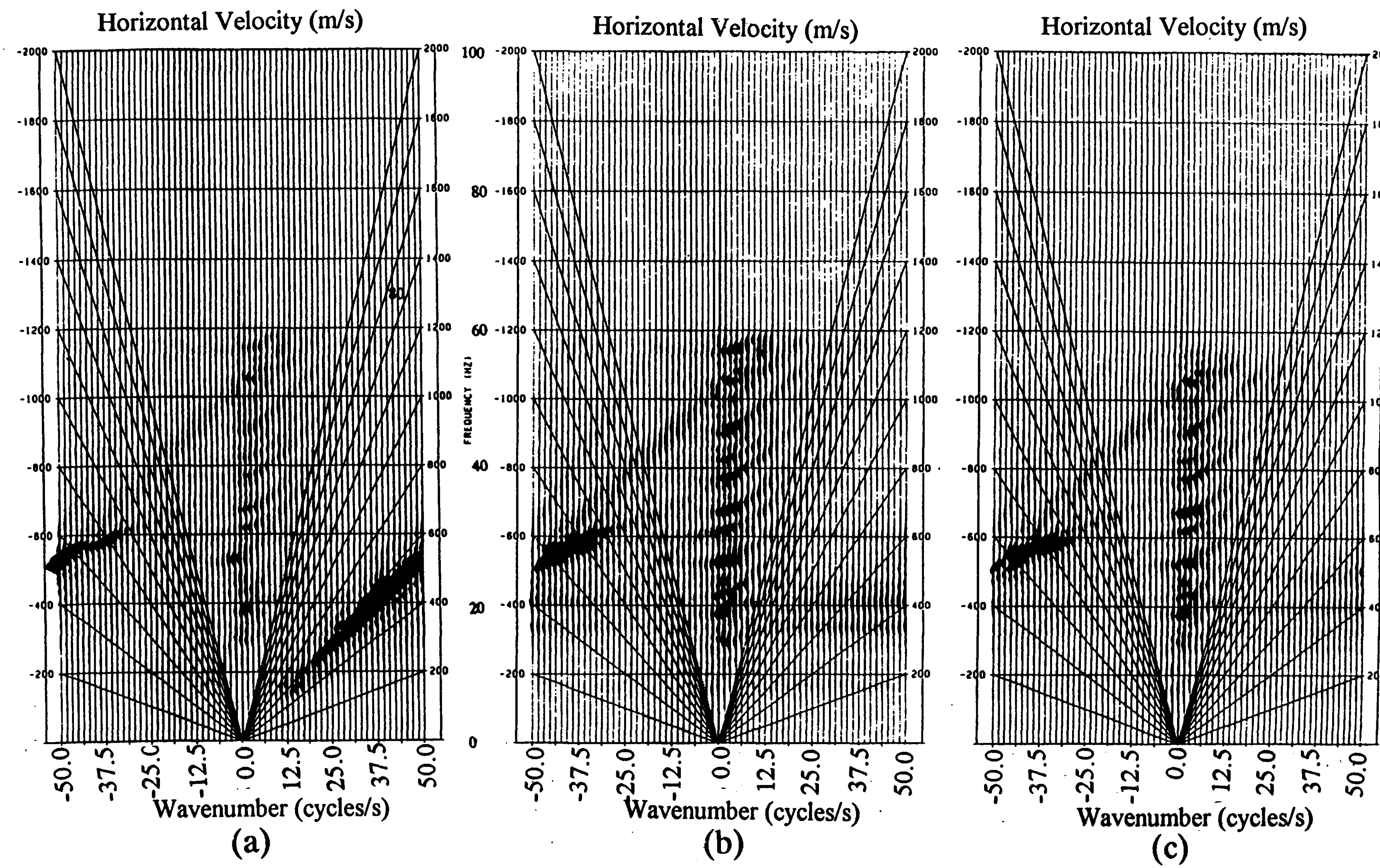

Figure 4.15 f-k transform of synthetic shot gather a) input gather after LMF compression, b) f-k filter (with LMF compression/de-compression), and c) median f-k (with LMF compression/de-compression).

4.5 Real data

Two data sets were used to demonstrate the application of *f-k* filters. The first from Alberta, approximately 30 km west of Calgary, was a shallow section with easily interpreted shear-wave refraction arrivals. The second from Wyoming was a multicomponent dynamite line acquired over a known anti-clinal structure.

4.5.1 Springbank FS91-1

Figure 4.5 and 4.6 show typical P-wave and P-SV wave shot records after applying a series of narrow band filters. The frequency bandwidth of the surface waves on both components is 4-50 Hz. These higher frequencies suggest that higher modes of the Rayleigh waves are present. The S-wave refraction first breaks were reasonably pickable on an interactive workstation. The P-wave and S-wave first breaks were inverted with an interactive GLI refraction analysis package. The refraction interpretation depicted in section 4.3.2. served to improve the reflection static solution as well as infer the near-surface parameters α, β, and layer thicknesses.

After determining the shear-wave velocity bounds from refraction analysis, the shot gathers were transformed to the ω-p domain as described in section 4.3.3. Within the velocity bounds and on the basis of expected linear slopes determined from the dispersion models, an LFM operator was designed as shown in Figure 4.1. Further confirmation of this estimate was gained by measuring the apparent velocities of the surface waves of the narrowband filter panels.

The frequency bandwidth of the data is approximately 4-70 Hz while that of the LFM operator slope is 17 Hz (at 800 m/s) to 25 Hz (at 230 m/s). This means a Δf of 9 Hz and phase velocity bounds of 230 to 800 m/s. The maximum time duration (T) of the dispersive wave train occurs at the maximum offset of 160 m and is simply 280 ms. A 512 ms operator was designed in the frequency domain at each offset and applied as a 1-D cross-correlation time-domain operator. By designing the phase and amplitude spectra independently and then inverse transforming to time (Equation 4.6) the phase-matched filter has passed all signal frequencies while compressing the dispersive waves only over their limited bandwidths (Figure 4.2).

Only the vertical component reflection stacks are shown in Figures 4.16-4.19.

The P-SV data were of such poor quality that it was not instructive to include them in these results. However, as previously demonstrated, the use of the shear-wave data was critical in the estimation of shallow shear-wave velocities and layer thicknesses. Also, the elliptical ground motion of Rayleigh waves can only be identified if both the radial and vertical components are recorded in the field.

After LFM compression, pre-stack filters were applied to reject dips > 8 ms/trace. The LFM operators were flipped in time and again cross-correlated to return the reflection events to their original wavelet spectrum. Figure 4.16 compares the resultant common offset stacks for the unfiltered and pre-stack filtered gathers. The two-component line (FS90-1) indicated primary reflectors should be seen at the Edmonton at 400 ms, an upper detachment at 700 ms, and a lower detachment at 800 ms formations (Lawton and Harrison, 1990).

Four final stacks were made to attempt to image these reflectors and compare the ability of these new hybrid multichannel filters in removing ground roll. Figures 4.17 and 4.18 are vertical component stacks without pre-stack filtering. Figure 4.18 has an inside mute applied which is specifically designed to remove all ground-roll noise with an apparent velocity less than 260 m/s. This only uses data recorded within the optimum window as depicted in Figure 1.1 in the first chapter. The resulting stack is still considerably better than the optimum offset single fold stacks used in shallow reflection engineering by Hunter et al (1984) as it benefits from a fold multiplicity of 16 times at 500 ms.

The results of applying the LFM compression followed by pre-stack *f-k* or median *f-k* filtering (Figures 4.19 and 4.20) are not as good as simply muting the inside traces. This is especially true above 700 ms. However, the median *f-k* result has a higher signal-to-noise ratio than both the unfiltered and pre-stack *f-k* filtered sections particularly at the level of the lower detachment (≈800 ms).

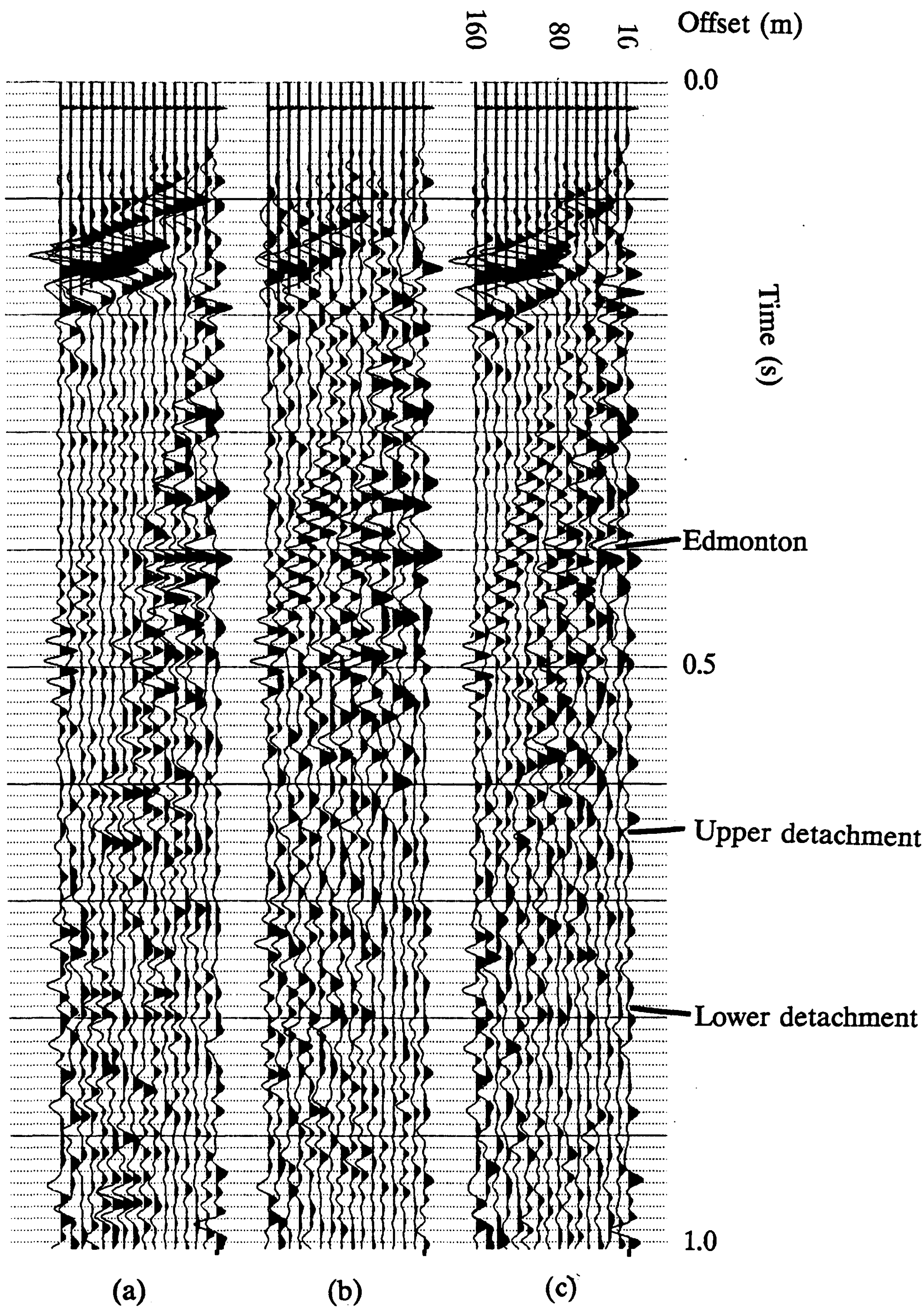

Figure 4.16 Common-offset stacks at station 227, a) after LMF and median f-k filters, b) after LMF and f-k filters and c) conventional stack without filters.

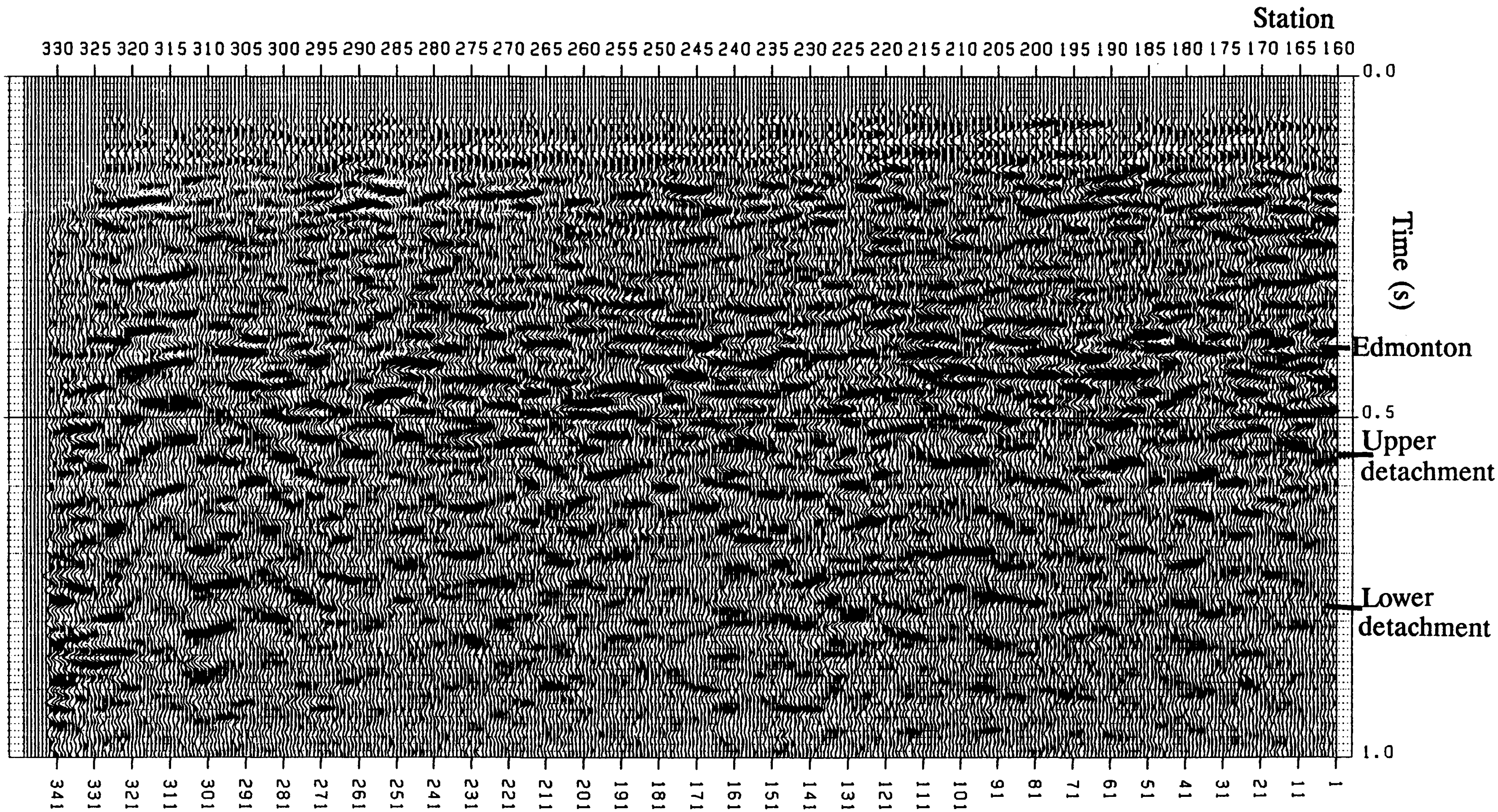

Figure 4.17 Springbank FS91-1 vertical component final stack.

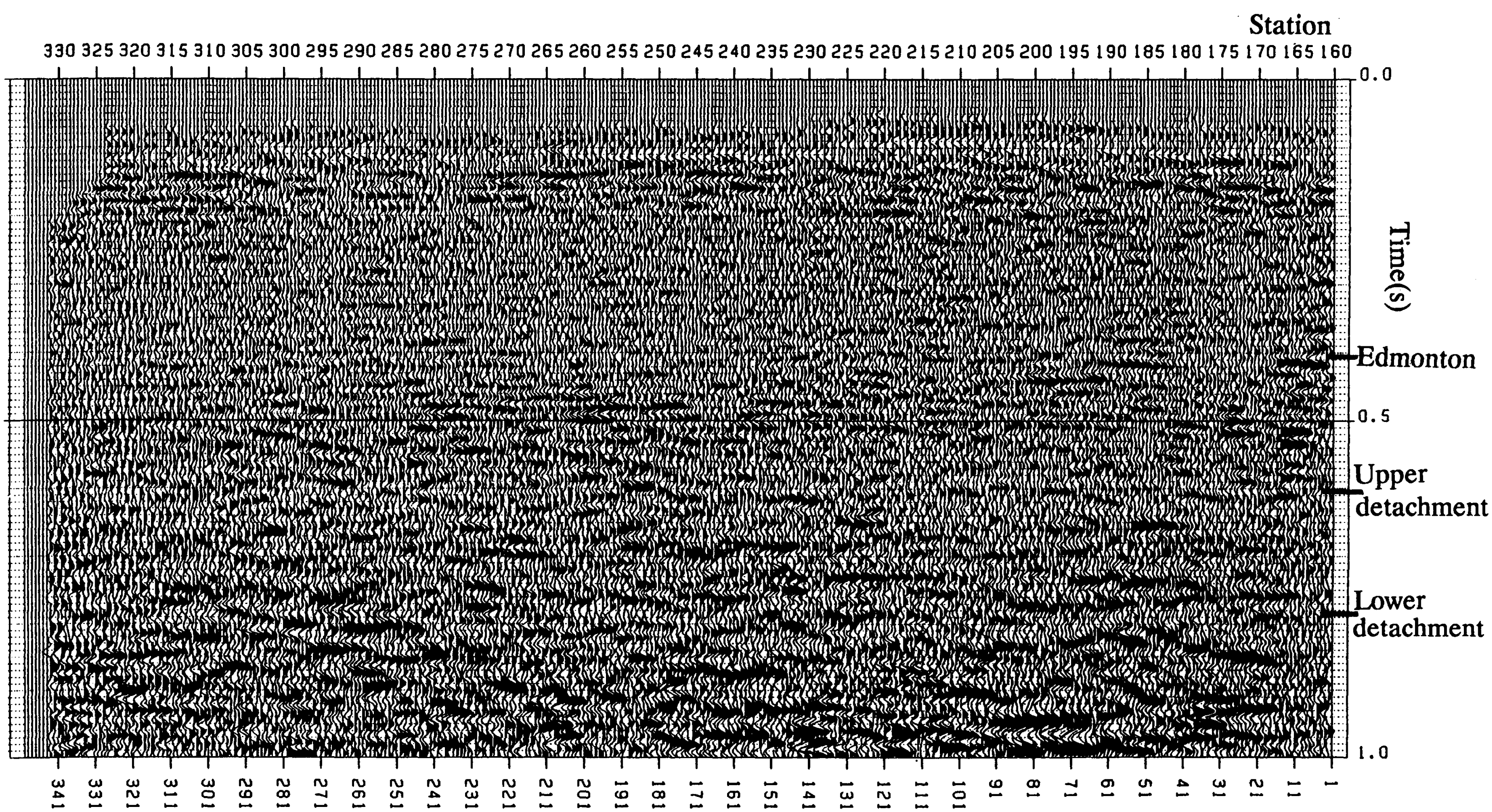

Figure 4.18 Springbank FS91-1 vertical component final stack with inside mute.

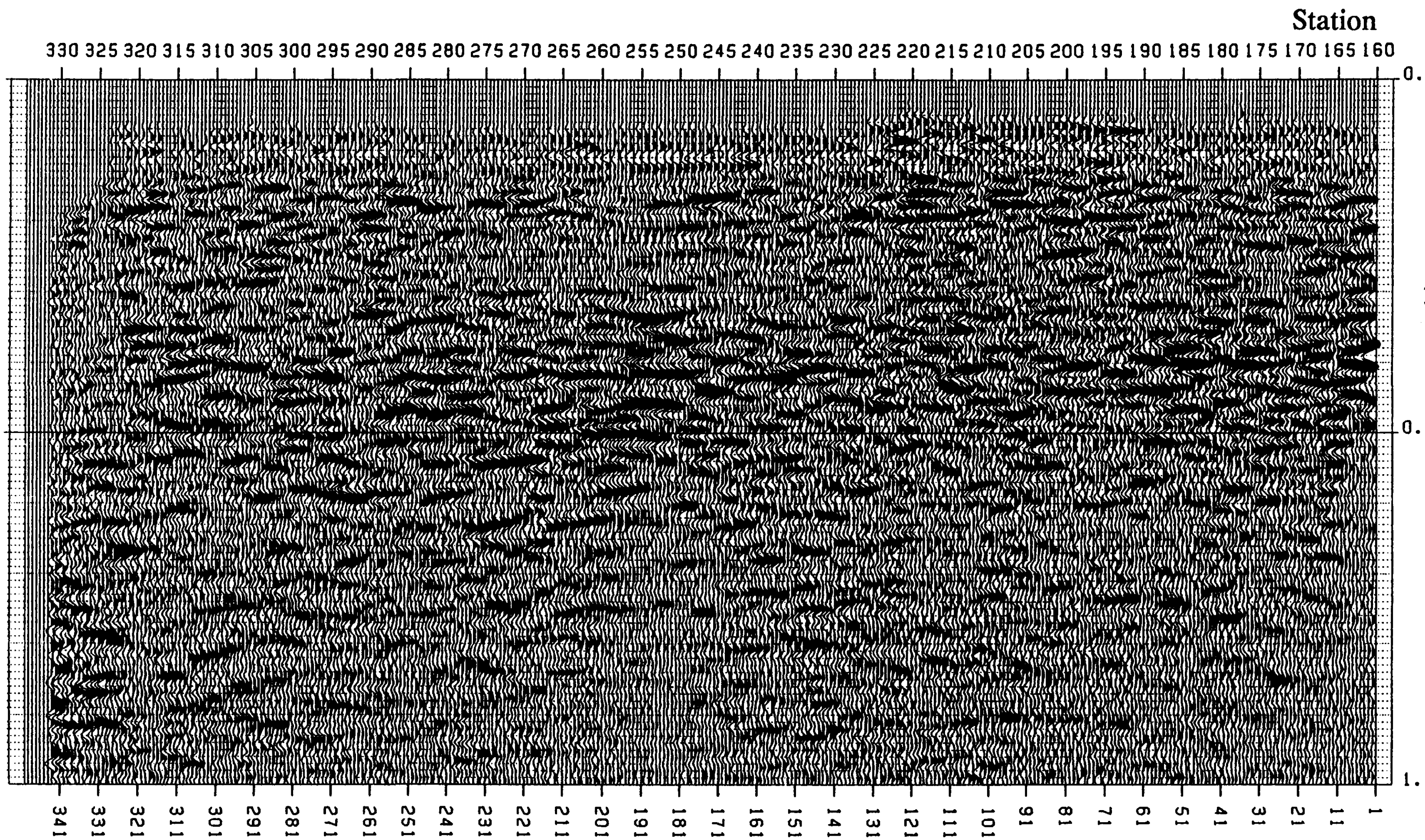

Figure 4.19 Springbank FS91-1 vertical component final stack with LMF compression and pre-stack f-k filters.

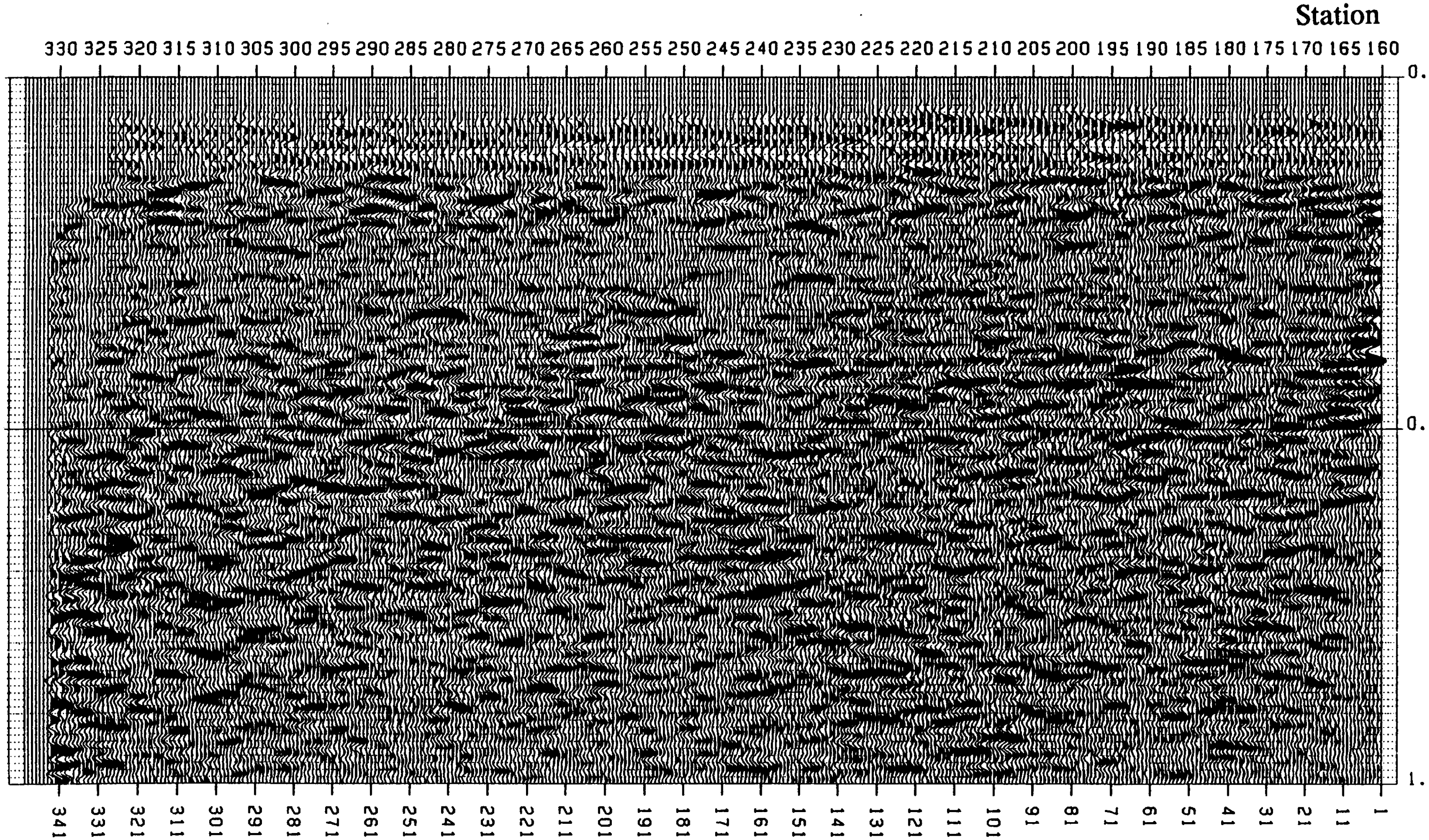

Figure 4.20 Springbank FS91-1 vertical component final stack with LMF compression and pre-stack median f-k filters.

4.5.2 South Casper Creek

The acquisition parameters used in the South Casper Creek survey are summarized in section 1.5.2.3. Typical shot records from the vertical and radial component data are depicted in Figure 4.21. The time scale of the radial component is 1.5 times the vertical component to approximately equate P-P reflections on the vertical component with P-SV reflections on the radial component. Two primary reflectors are indicated at 210 ms (1) and 520 ms (2) on the vertical component shot gather. Note, that the corresponding reflections on the shear-wave or radial component gather are difficult to resolve. The deeper event is no longer within the optimum window above the shear refraction and dispersive ground roll.

The vertical component data were processed using the processing flow shown in Table 4.1. An important step in the processing sequence is the creation of common shot and receiver stacks to hand-pick surface-consistent statics. Due to the presence of significant structure, common-receiver traces from the middle of the line would mis-stack receiver traces from the beginning or end of the line. To correct this problem, time structure is measured from an initial common depth point (CDP) brute stack of the data. The NMO-corrected data were then structurally time corrected to a flat datum by removing the times picked in the CDP stack to create common-receiver and common-shot stacks for residual static picks. This was only done as an off-line process for static resolution.

An average α/β velocity ratio of 2.10 was determined from the time difference of the two primary events mentioned above measured on the P-P wave versus P-SV wave CDP stacks. The radial component data were processed using the processing flow of Table 4.2. Note the additional step of common reflection point rebinning using an asymptotic approximation. Although this was a three-component data set, including the transverse shear component, only the radial component was used in this investigation. Assuming isotropic homogeneous layers, no Rayleigh wave motion or P-SV energy would be observed on the transverse component. Careful observation of the raw records verified this assumption.

The radial component was narrowband filtered to attempt to estimate the LFM compression operator (Figure 4.23). The apparent velocities picked for each narrowband filter panel are shown as a solid black line. The velocity versus frequency

DEMULTIPLEX
GEOMETRIC SPREADING COMPENSATION
    $1.0 * e^{0.0007t}$
[OPTIONAL PRE-STACK FILTER]
SPIKING DECONVOLUTION
    1 windows, 90 ms operator 1.0% prewhitening
REVERSE POLARITY OF TRAILING SPREADS
APPLY FINAL P-WAVE SOURCE STATICS
INITIAL VELOCITIES
APPLY HAND STATICS FROM COMMON RECEIVER PLOTS
AUTOMATIC SURFACE CONSISTENT RECEIVER STATICS
    Correlation window from 300 to 1250 ms
    Maximum shift of + or - 36 ms
CRP STACK
CONVERTED-WAVE REBINNING
    Vp/Vs ratio of 2.10 independent of depth
VELOCITY ANALYSIS
NORMAL MOVEOUT
FIRST BREAK MUTE
    distance 219 m, time 70 ms
    distance 1800 m, time 650 ms
TRACE SCALING
    Mean amplitude of 2000
    Windows 0-1400 ms
CDP TRIM STATICS
    Correlation window from 300-1250 ms
    Maximum shifts + or - 20 ms
STACK
    offsets 0-1800 m
BANDPASS FILTER
    Zero-phase, 12-30 Hz
RMS GAIN
    Mean amplitude of 2000
    Window 300-1250 ms

Table 4.1 Processing sequence and parameters for the South Casper Creek, P-SV data.

points are plotted in Figure 4.22 and marked as "Narrowband estimate". The refracted shear first arrival is embedded within the noisy radial shot record and too difficult to resolve accurately on a surface-consistent basis for GLI refraction analysis.

DEMULTIPLEX
GEOMETRIC SPREADING COMPENSATION
    $1.0 * e^{0.0008t}$
[OPTIONAL PRE-STACK FILTER]
SPIKING DECONVOLUTION
    1 windows, 60 ms operator 1.0% prewhitening
INITIAL VELOCITIES
HAND STATICS FROM COMMON SHOT & RECEIVER STACKS
AUTOMATIC SURFACE CONSISTENT STATICS
    Correlation window from 300 to 1250 ms
    Maximum shift of + or - 24 ms
CDP STACK
VELOCITY ANALYSIS
NORMAL MOVEOUT
FIRST BREAK MUTE
    distance 220 m, time 120 ms
    distance 680 m, time 280 ms
    distance 1200 m, time 560 ms
TRACE SCALING
    Mean amplitude of 2000
    Windows 0-400, 300-900, 700-1000 ms
CDP TRIM STATICS
    Correlation window from 100-900 ms
    Maximum shifts + or - 16 ms
STACK
    offsets 0-1200 m
BANDPASS FILTER
    Zero-phase, 12-70 Hz
RMS GAIN
    Mean amplitude of 2000
    Window 300-900 ms

Table 4.2 Processing sequence and parameters for the South Casper Creek, P-P data.

However, a rough approximation of the refraction velocity suggests a bedrock shear-wave velocity of 1300 m/s.

An initial shallow geology model was assumed to estimate the dispersion curve. The thicknesses and shear-wave velocities were perturbed to obtain a best fit dispersion curve that matched the "Narrowband Estimate". A simple three-layer case

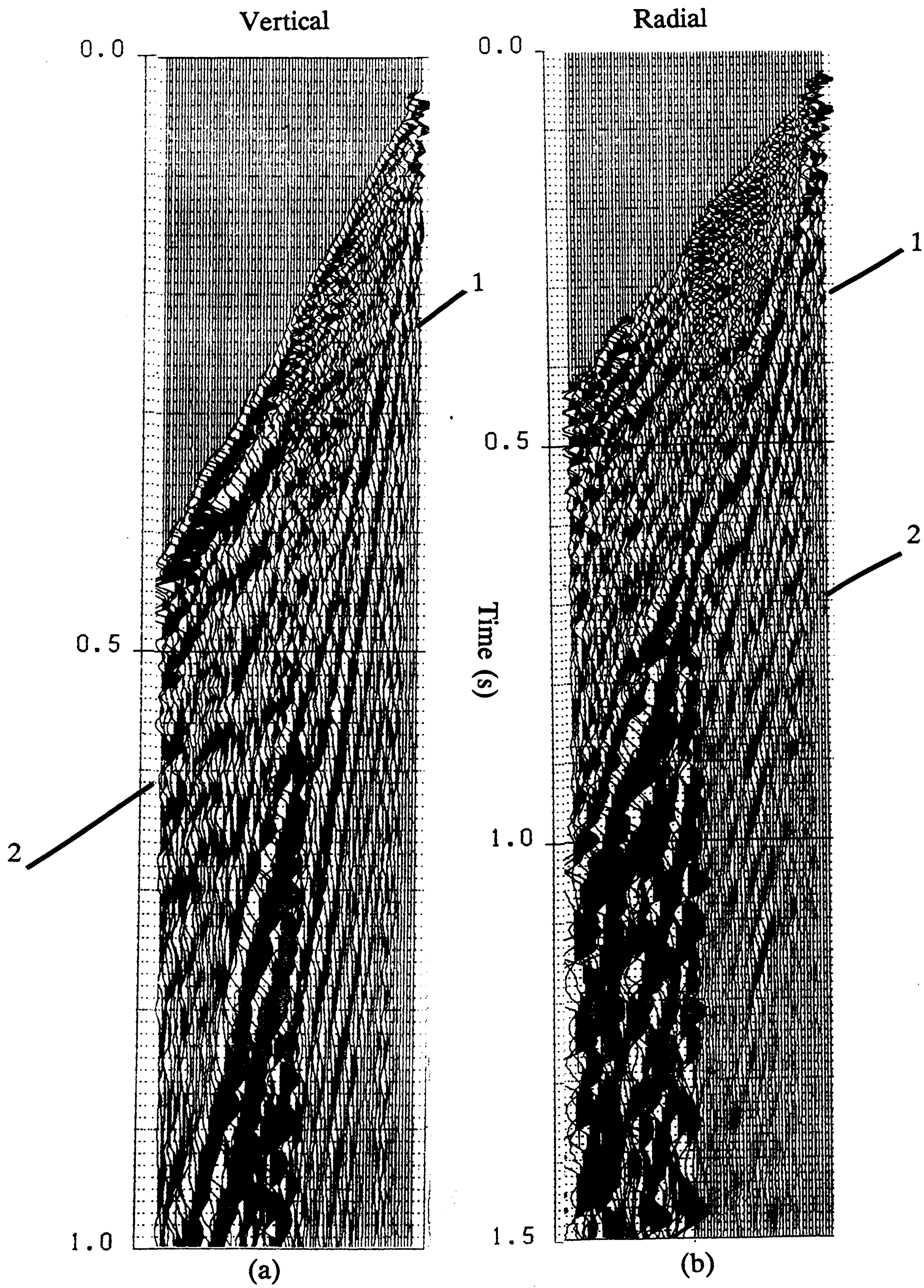

Figure 4.21 South Casper Creek shot gather 41 a) vertical component b) Radial component

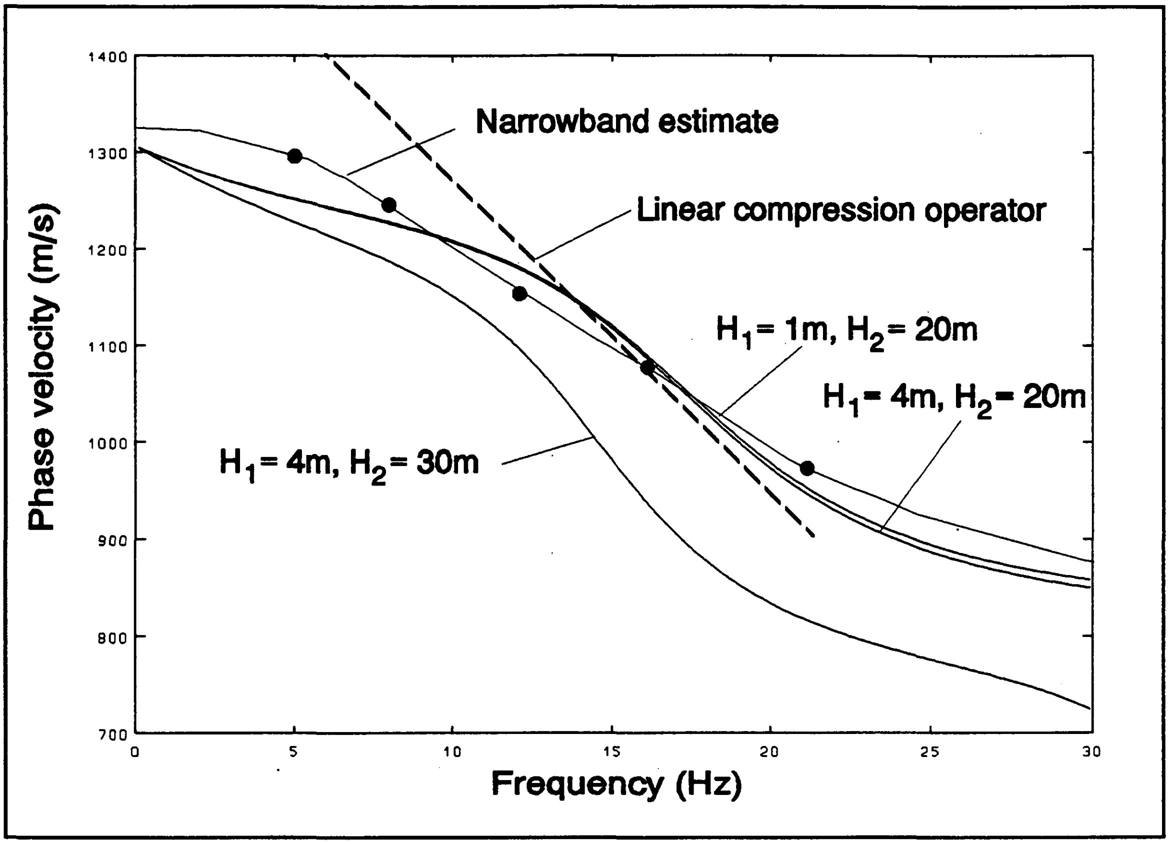

Figure 4.22 South Casper Creek dispersion curve estimate with narrowband filter panels in Figure 4.23.

provided a reasonable fit and realistic geologic model (refer Table 4.3). The P-wave

	Vp (m/s)	Vs (m/s)	Thickness (m)	ρ (gm/cc)
Weathering	600	230	2-5	2.2
Drift	1500	230	20	2.2
Half space	2100	900	∞	2.2

Table 4.3 Velocities used for South Casper Creek near-surface geology model.

velocities and densities have very little effect on the dispersion curve as discussed in section 3.2. The first-layer thickness, whether 1 m or 4m, of a purely guessed low-velocity material, does not effect the dispersion curve dramatically. Very little can be said about the first layer P-wave parameters on the basis of the seismic data. The P-wave direct arrivals could not be observed on the shot records because the first offset was too large. If the velocity ratio is $V_2/V_1=2.16$, the critical distance/depth to first layer ratio is approximately 3.25. This means the minimum depth recorded with a minimum offset of 15 m is approximately 4.6 metres.

The important parameters to consider are shear wave velocities (230 and 900 m/s) and the thickness of the second layer (20 meters). The exact inversion of the dispersion curve is not critical in the design of the LFM compression operator. The operator used for these lines is shown in Figure 4.22 as a dashed line. Figure 4.24 demonstrates the effect of applying this operator to the radial shot gather at various narrowband frequencies. Figures 4.25 b) and 4.26 b) show the application of this operator to the raw vertical and radial shot gathers respectively. These figures also demonstrate the applications of the *f-k* and median *f-k* filters with and without LFM compression. In the case of the *f-k* filter, the dispersion compression enables the dip filter to remove negative aliased dip on the radial component, and the shallow section (<500ms) on both components is dramatically improved. In the case of the median *f-k* filter, the data are different but it is difficult to discern on the basis of a single shot record if the LFM compression operator improves this non-linear filter.

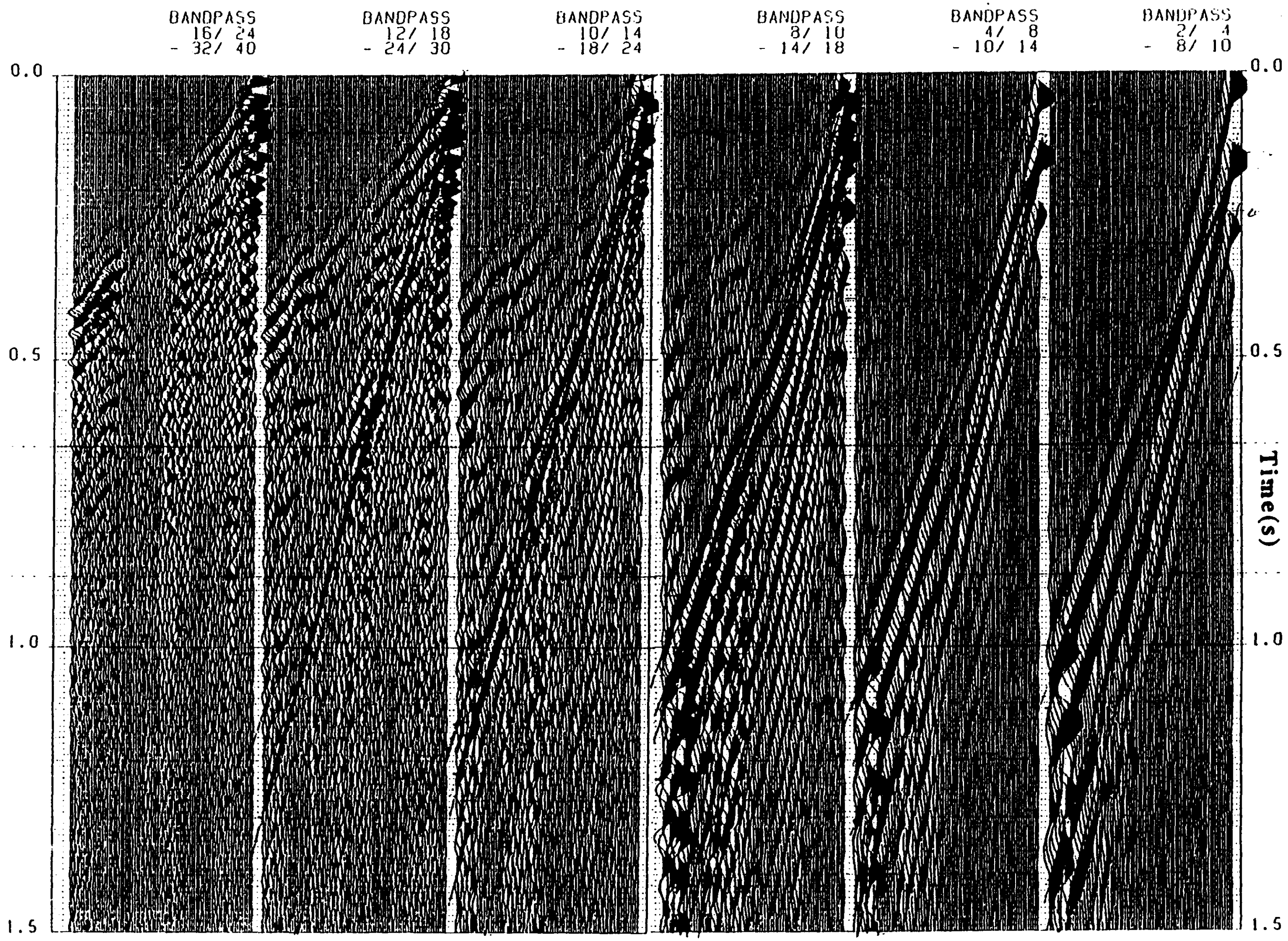

Figure 4.23 South Casper Creek radial component shot gather narrowband filter panel to estimate dispersion.

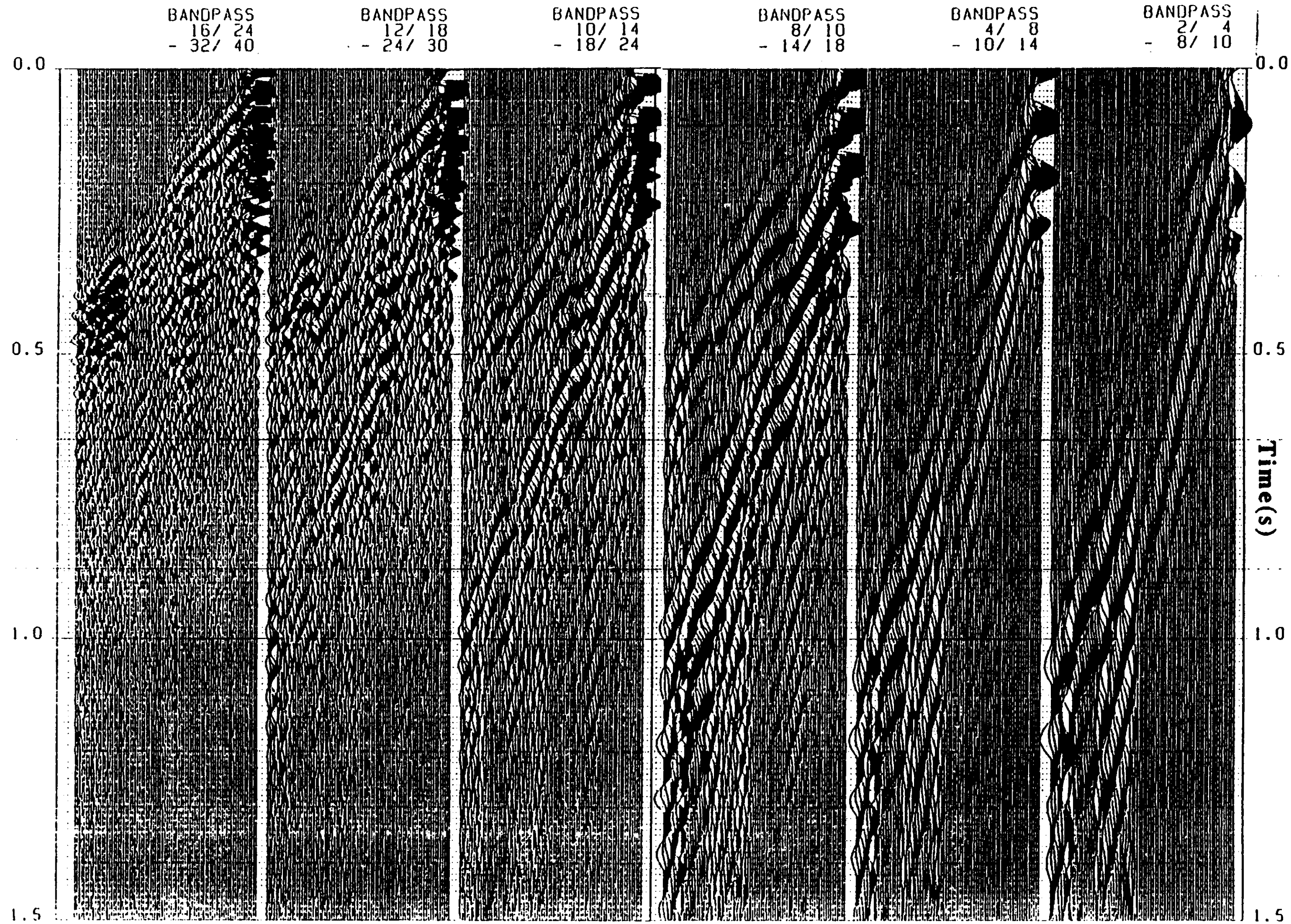

Figure 4.24 South Casper Creek radial component gather filter panels after dispersion compression filter is applied.

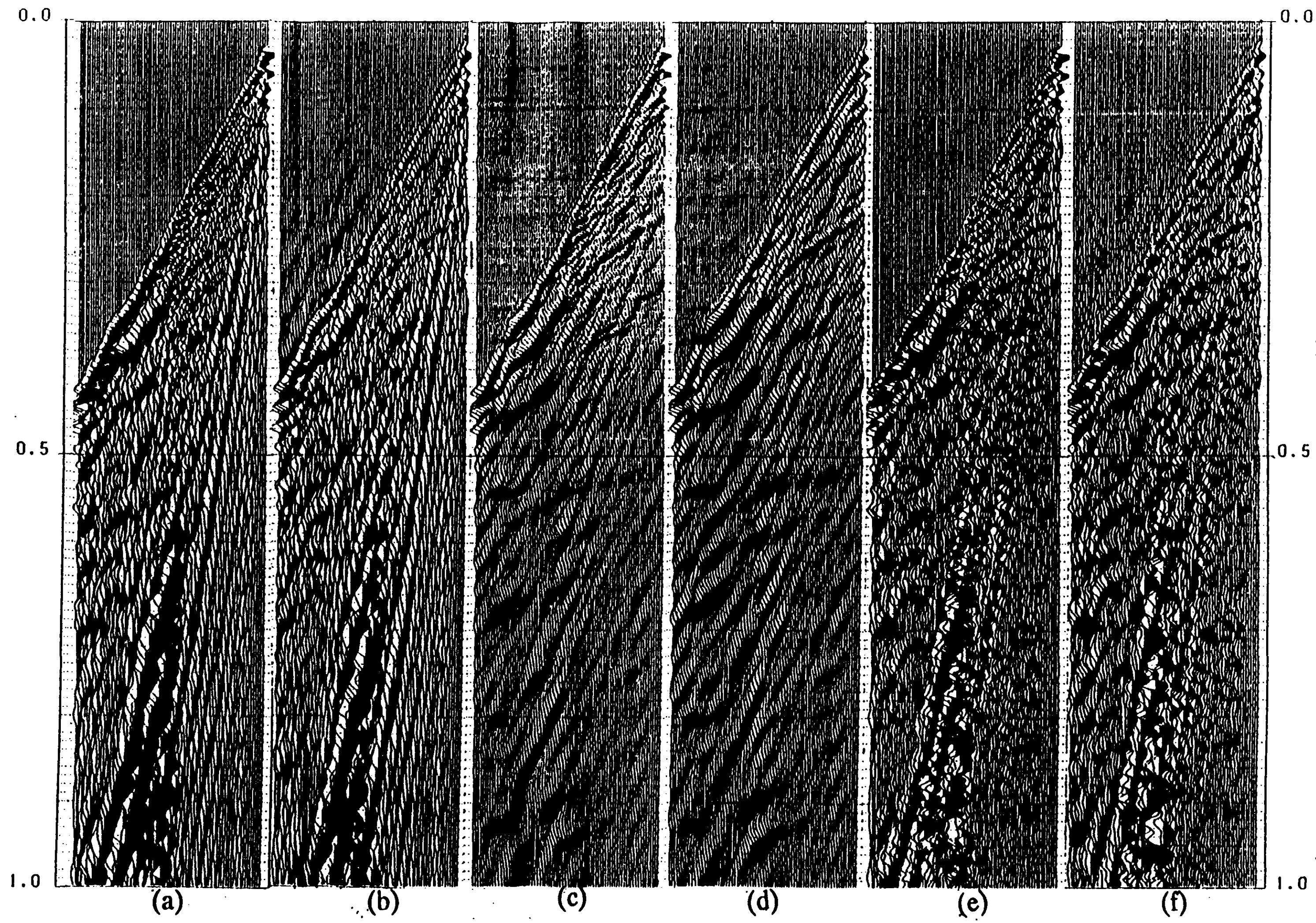

Figure 4.25 Vertical component shot gather a) raw data b) dispersion LFM compression of a), c) f-k filtered, d) f-k including LFM compression/decompression, e) median f-k filtered, f) median f-k including LFM compression/decompression.

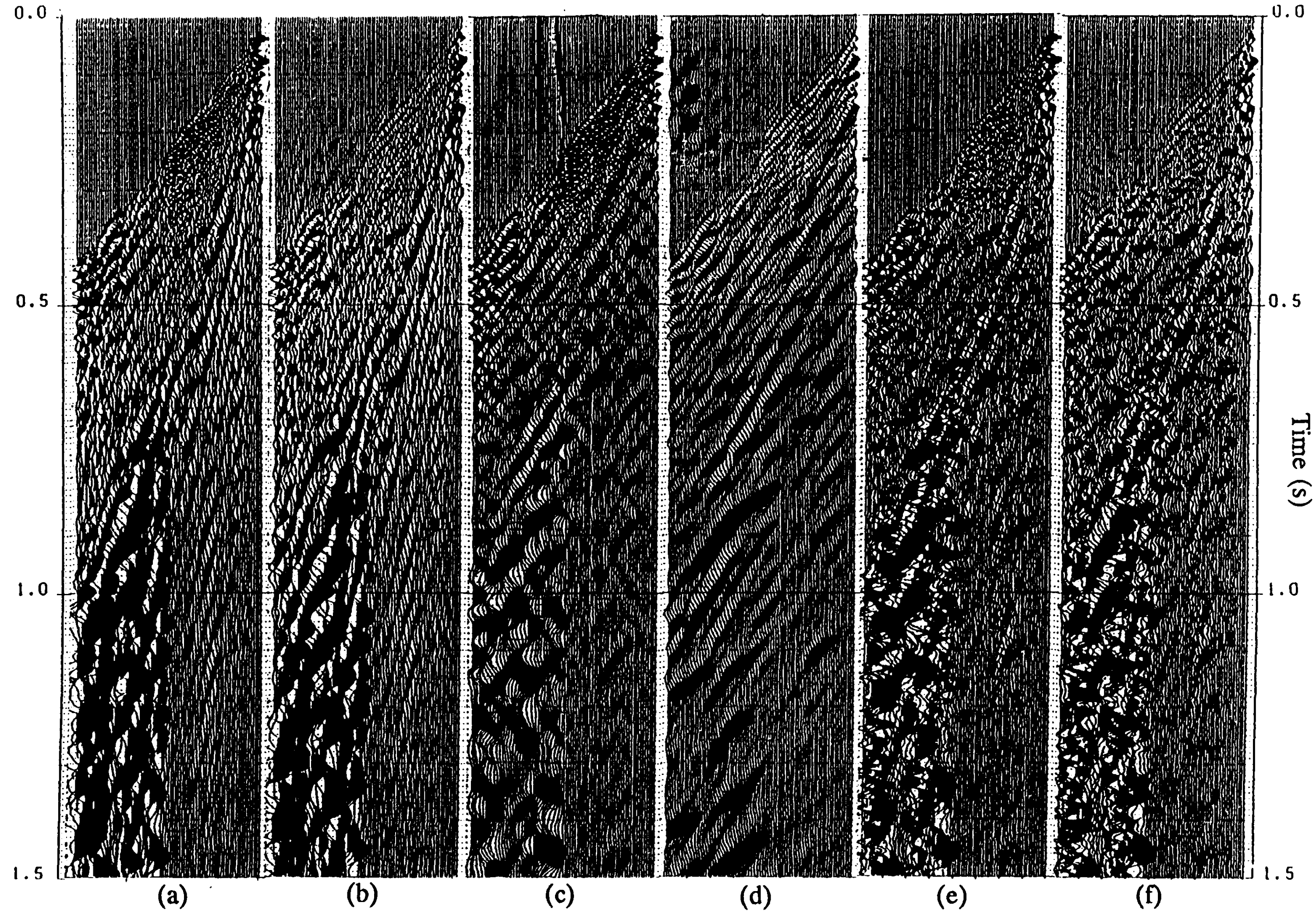

Figure 4.26 Radial component shot gather a) raw data b) f-k filtered c) median f-k filtered d) dispersion LFM compression of a), e) f-k including LFM compression, f) median f-k including LFM compression.

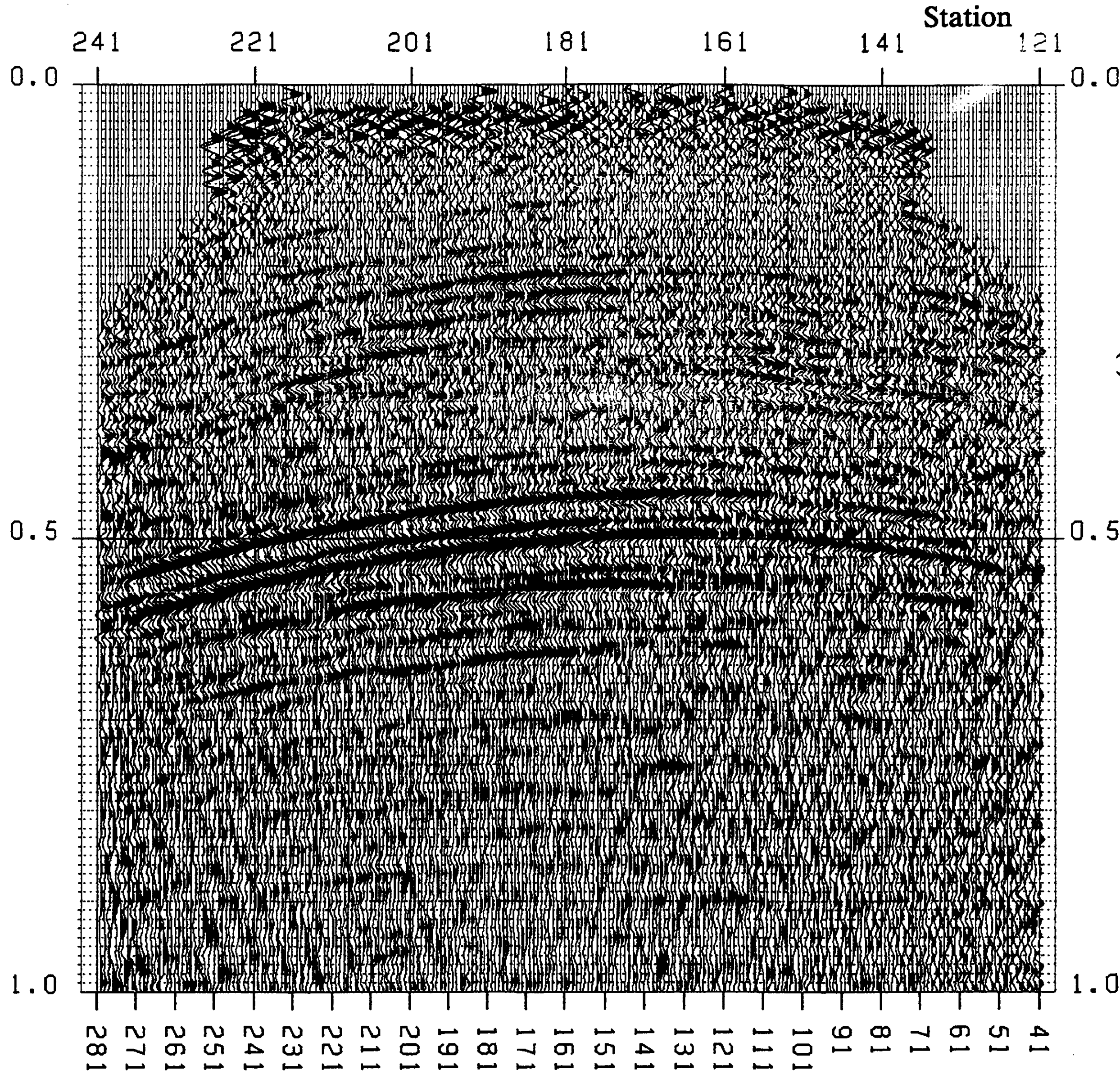

Figure 4.27 South Casper Creek vertical component final stack.

The final vertical component stacks are displayed in Figures 4.27 to 4.31. Generally, the application of a pre-stack filter improves the signal-to-noise ratio of the stacked section particularly at the shallow horizon (≈220 ms). The median *f-k* filter appears to work the best above this horizon where the fold is very low. The application of the LFM compression filter aids in the removal of residual aliased noise, which is especially noticeable on the right hand side of these sections. These are positive aliased dips which wrap around to negative dips and subsequently are not removed within the positive reject fan (refer Figure 1.2). The compression of dispersed aliased noise often brings the aliased dips back to the positive dip space in the *f-k* domain (ie. dips become less steep) which optimizes their removal with *f-k* filters.

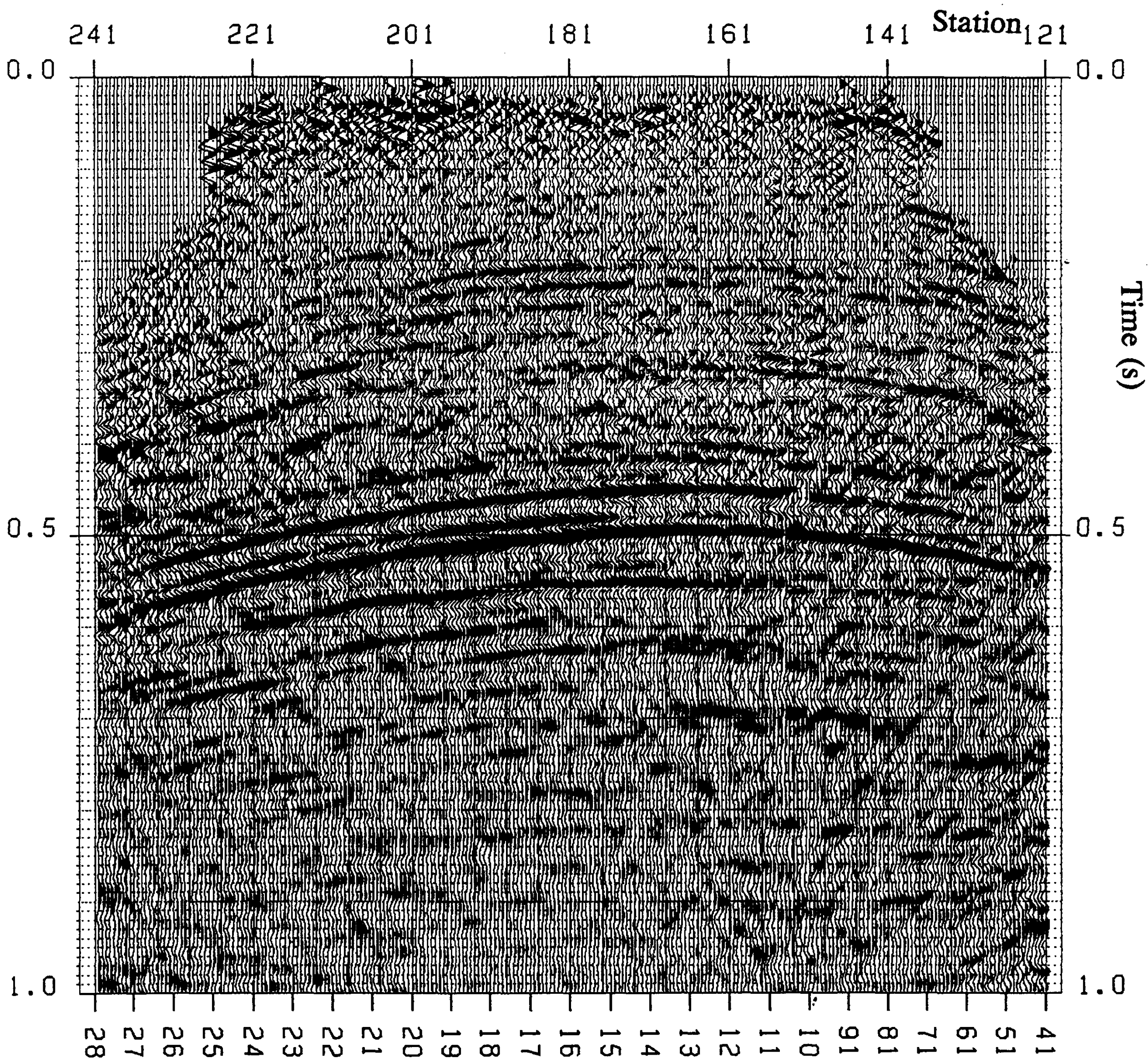

Figure 4.28 South Casper Creek vertical component stack with pre-stack f-k filter.

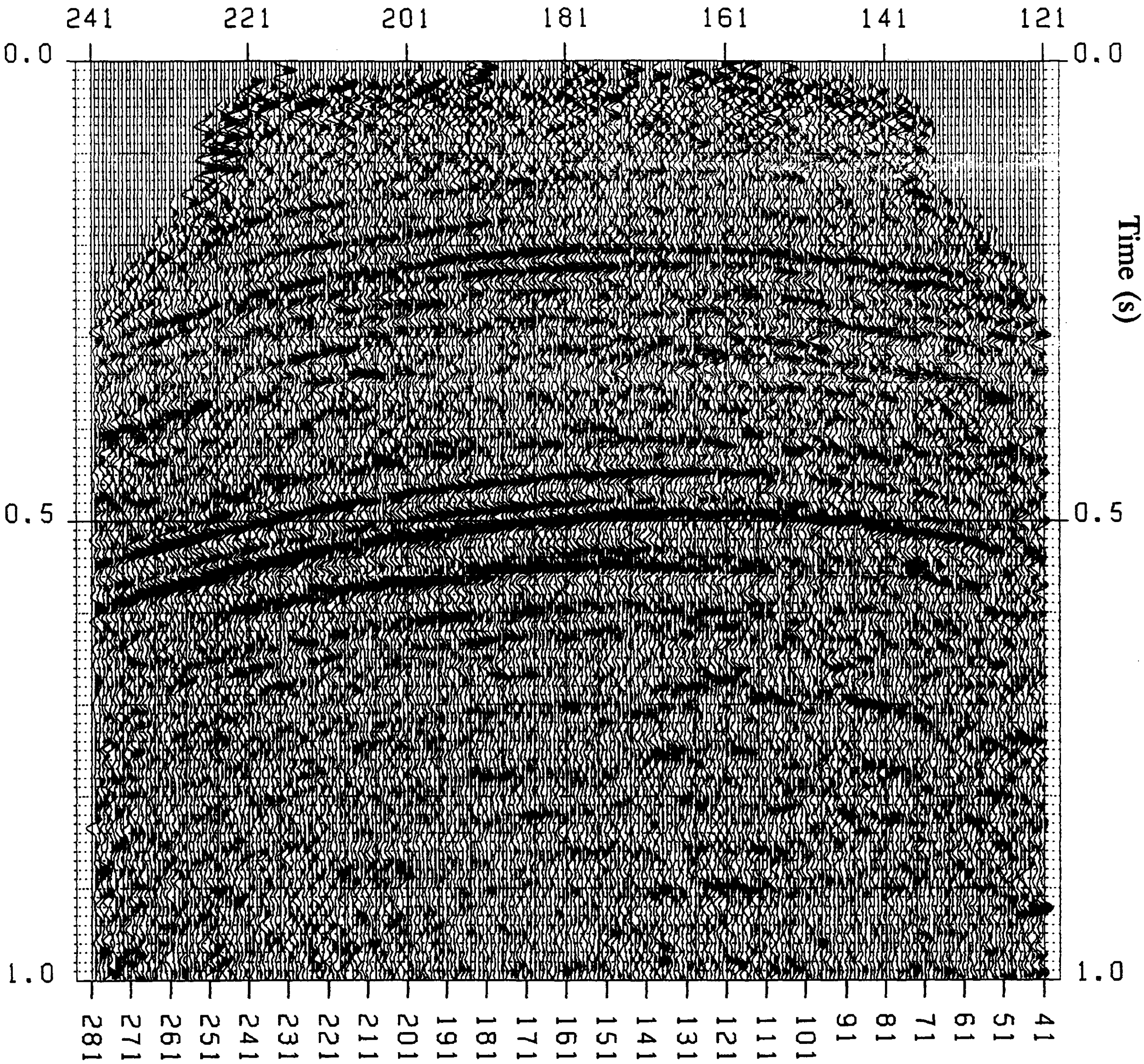

Figure 4.29 South Casper Creek vertical component stack with dispersion compression and pre-stack f-k filter.

The radial component (P-SV wave) sections are shown in Figures 4.32 to 4.36. These data are poorer in quality than the vertical component with lower frequency content, and lower signal-to-noise ratio for both random and coherent noise. The best results appear to be the output of an *f-k* filter with the LFM compression operator. The LFM compression operator improves the *f-k* filter (Figure 4.33 and 4.34) but seems to degrade the median *f-k* filter section (Figure 4.35 and 4.36). This may be

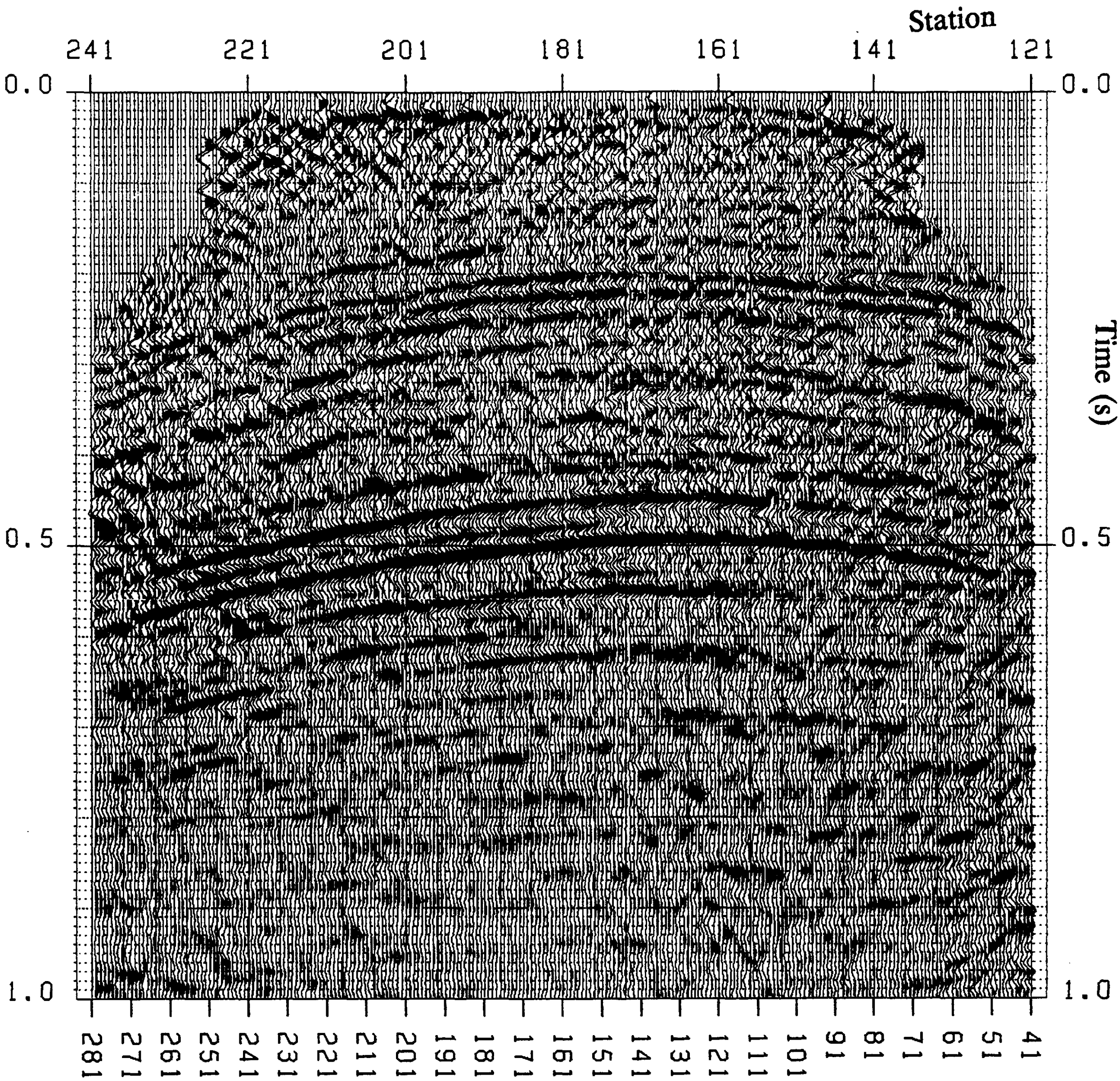

Figure 4.30 South Casper Creek vertical component stack with pre-stack median f-k filter.

due to the fact that shear-wave statics were often within the range of $\pm$ 100 ms for the radial component section. No pre-filter statics were applied, and thus sharp dips in the reflection horizons due to static shifts were treated as localized dips by the median *f-k* filter and true reflection horizons were erroneously removed. The LFM compression operator pre-median *f-k* appears to intensify this problem as depicted in Figure 4.36 when compared to Figure 4.35.

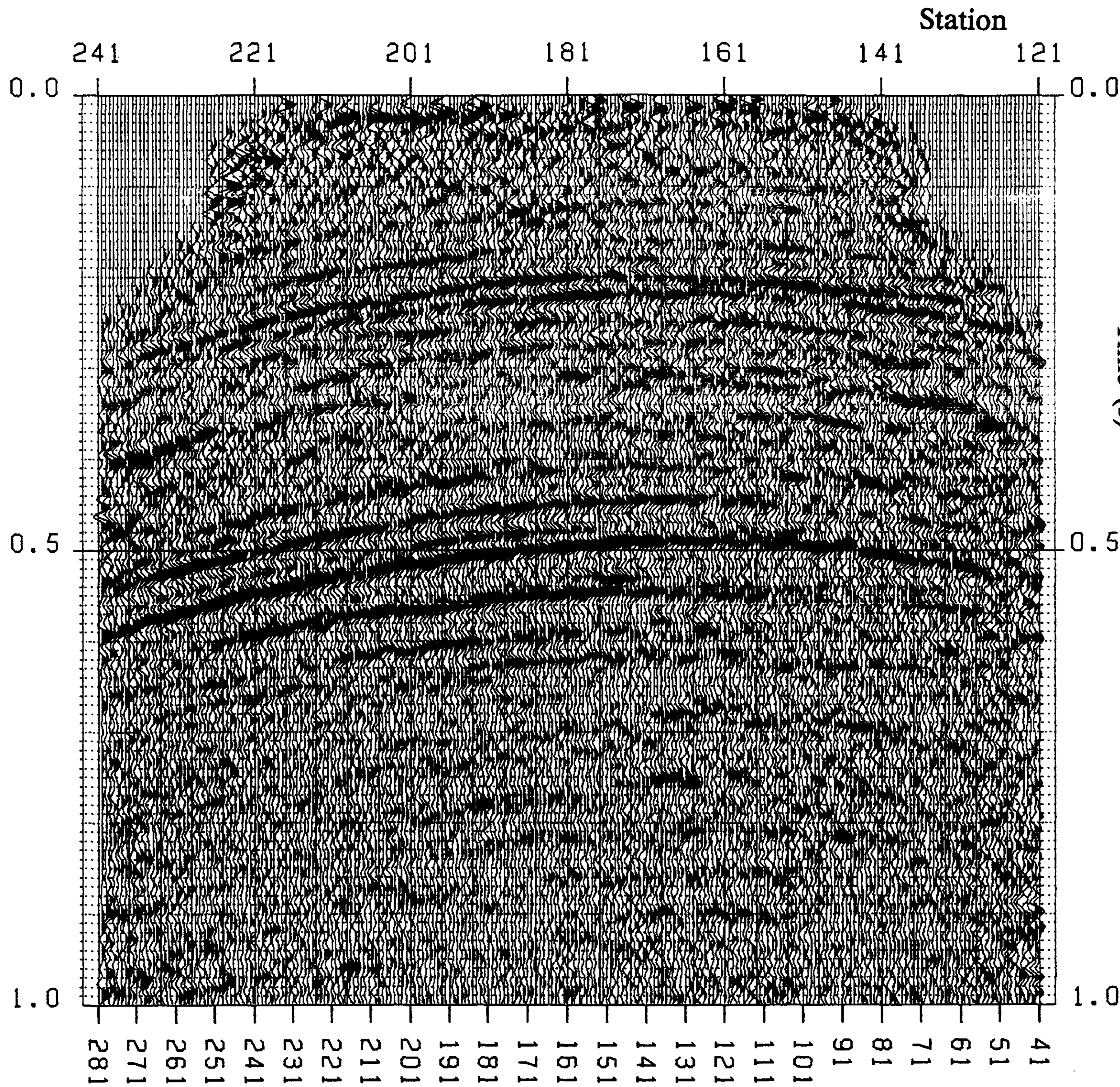

Figure 4.31 South Casper Creek vertical component stack with dispersion compression and pre-stack median f-k filter.

The *f-k* filtered final P-P section with LFM compression is correlated with the similarly processed final P-SV section in Figure 4.37. This demonstrates the difference in data quality between the vertical and radial component data in terms of over-all signal-to-noise ratio, frequency content, and geological response.

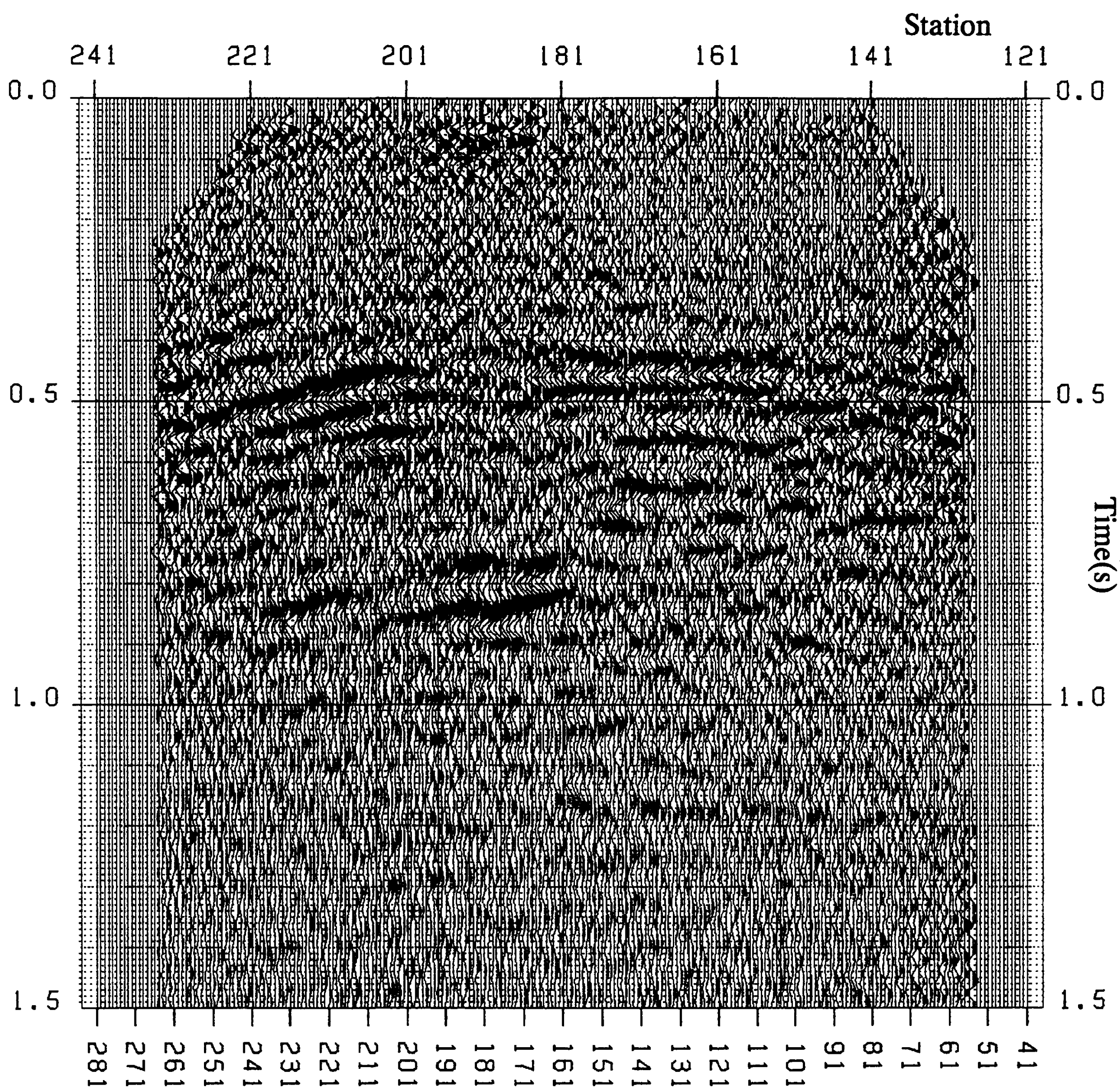

Figure 4.32 South Casper Creek radial component final stack.

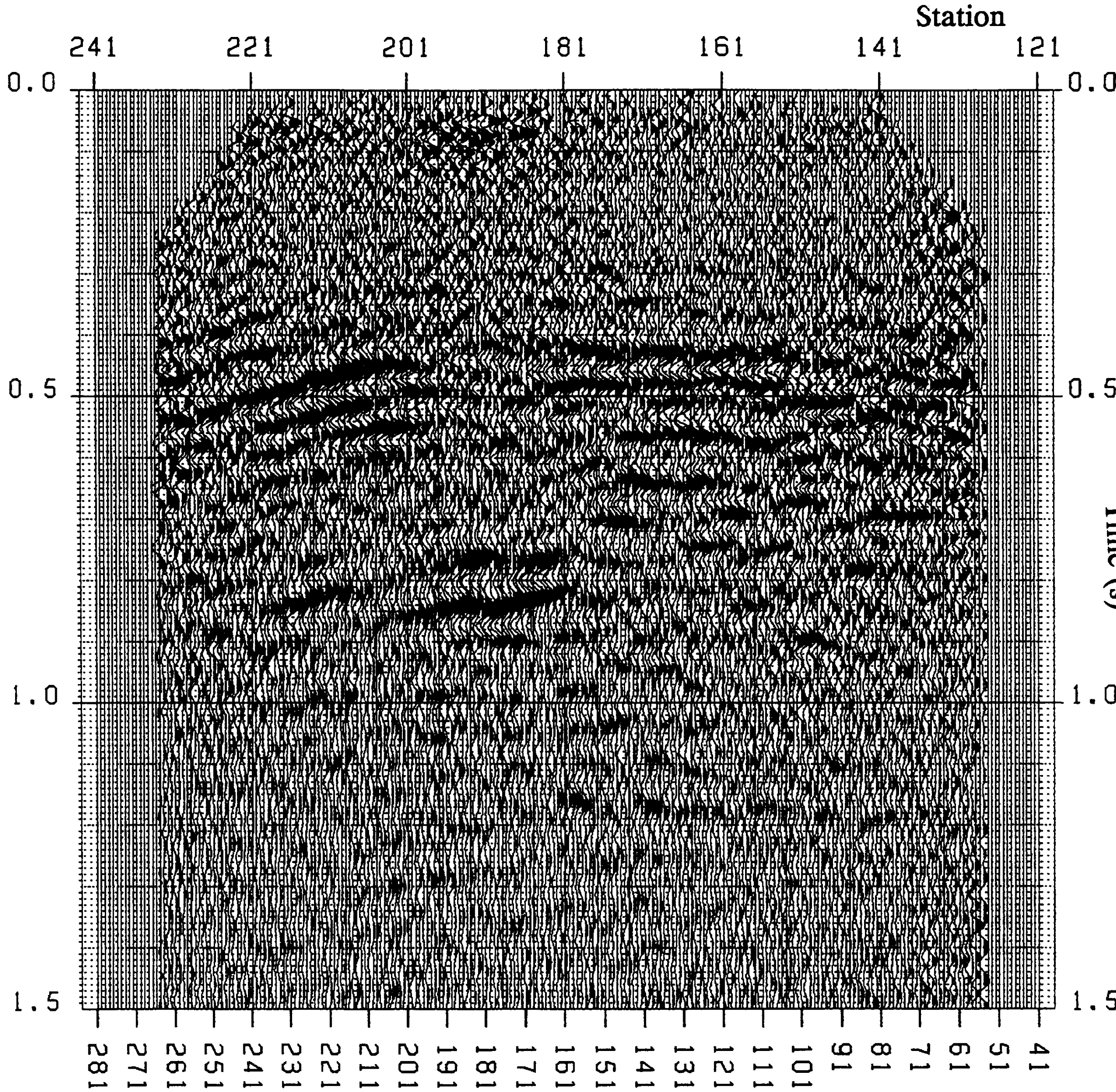

Figure 4.33 South Casper Creek radial component stack with pre-stack f-k filter.

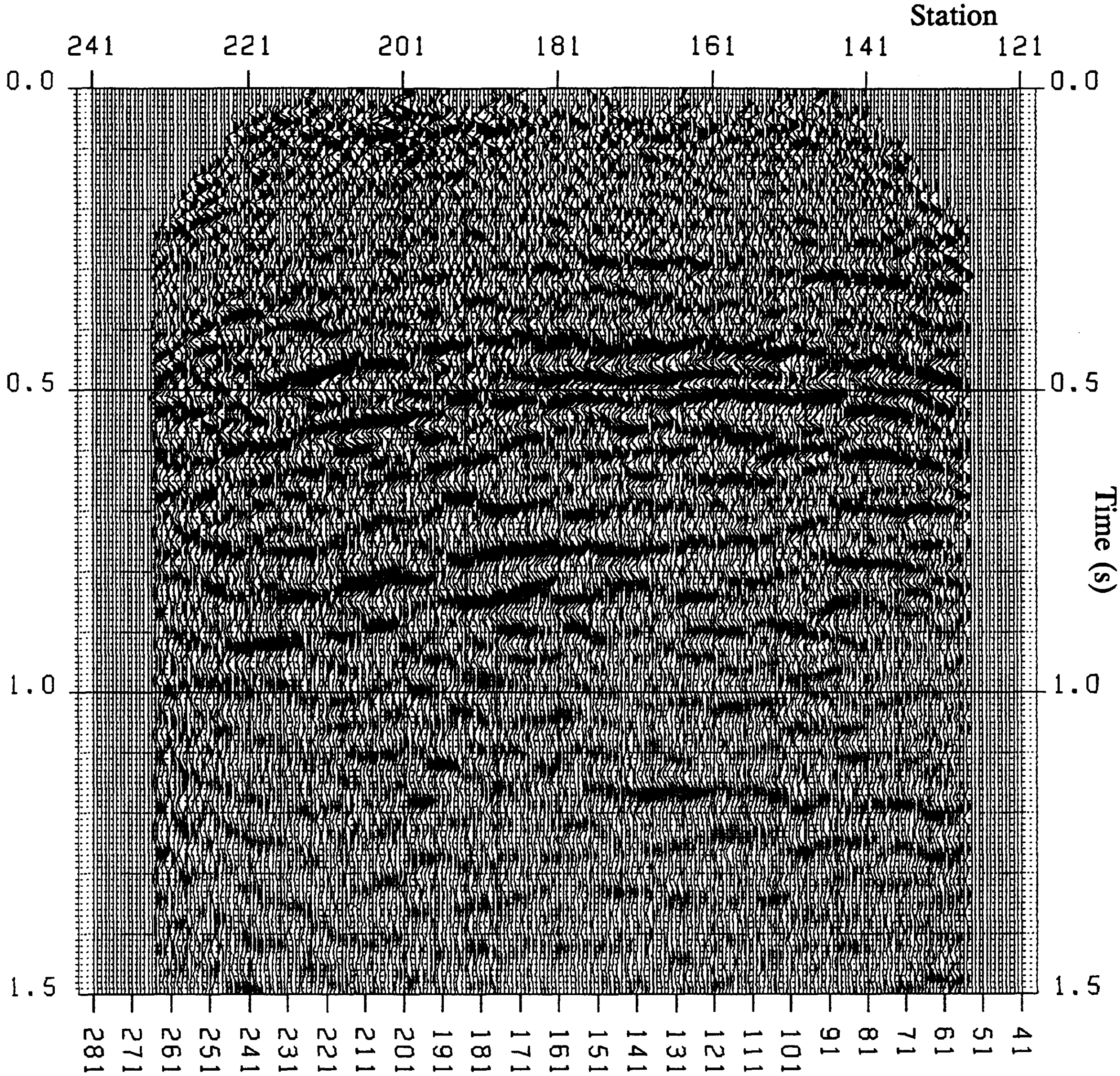

Figure 4.34 South Casper Creek radial component stack with dispersion compression and pre-stack f-k filter.

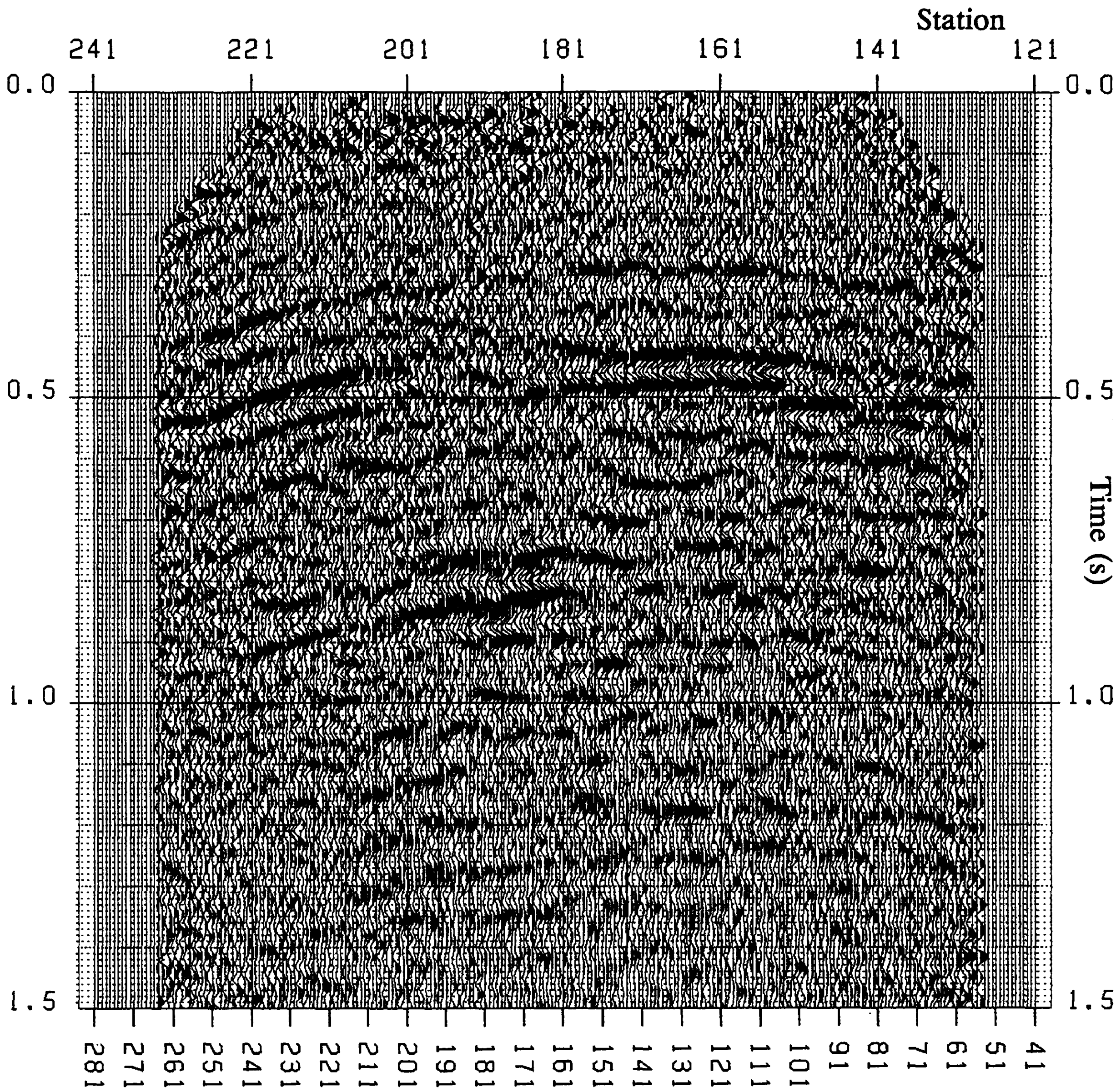

Figure 4.35 South Casper Creek radial component stack with pre-stack median f-k filter.

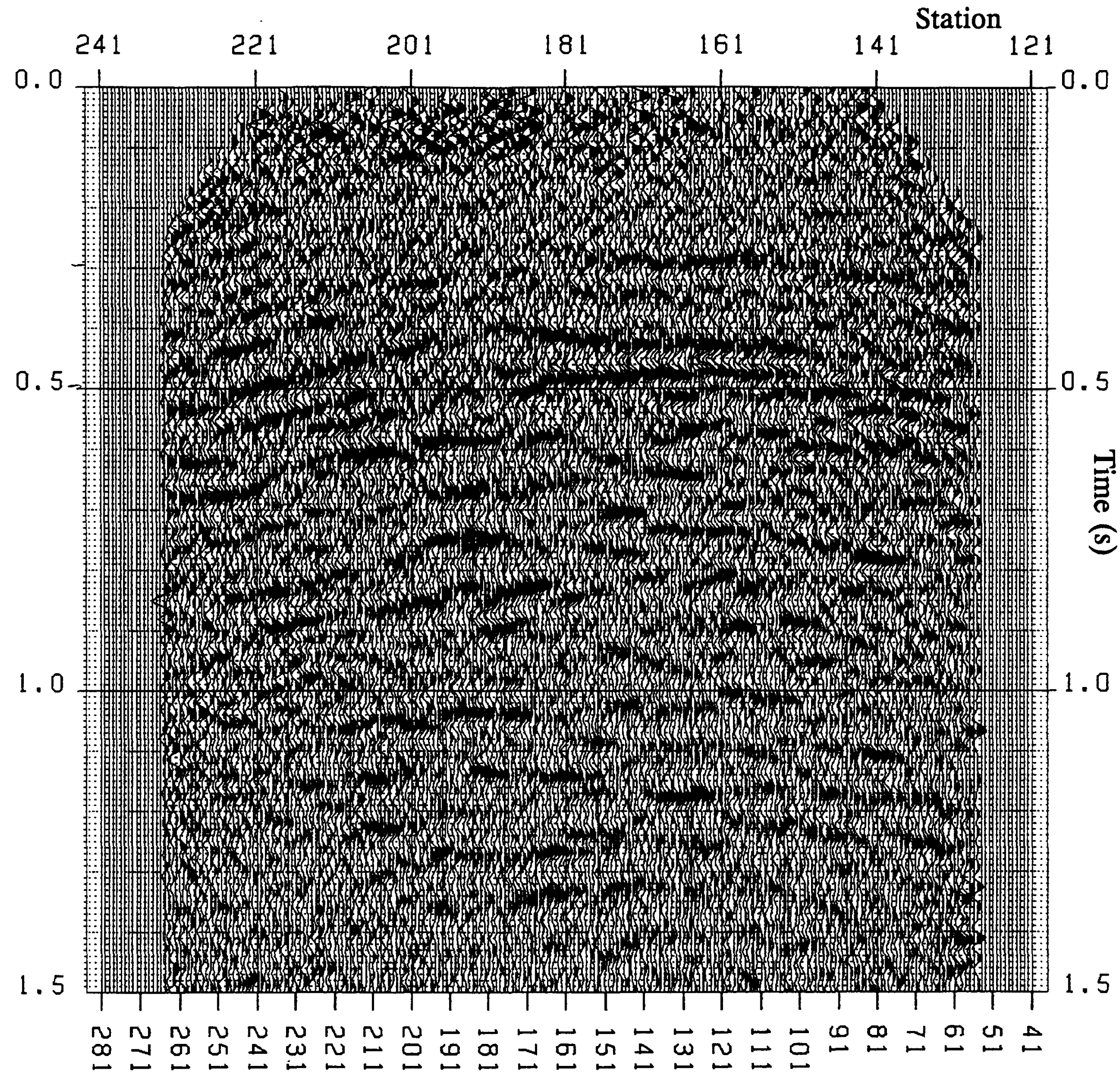

Figure 4.36 South Casper Creek radial component stack with dispersion compression and pre-stack median f-k filter.

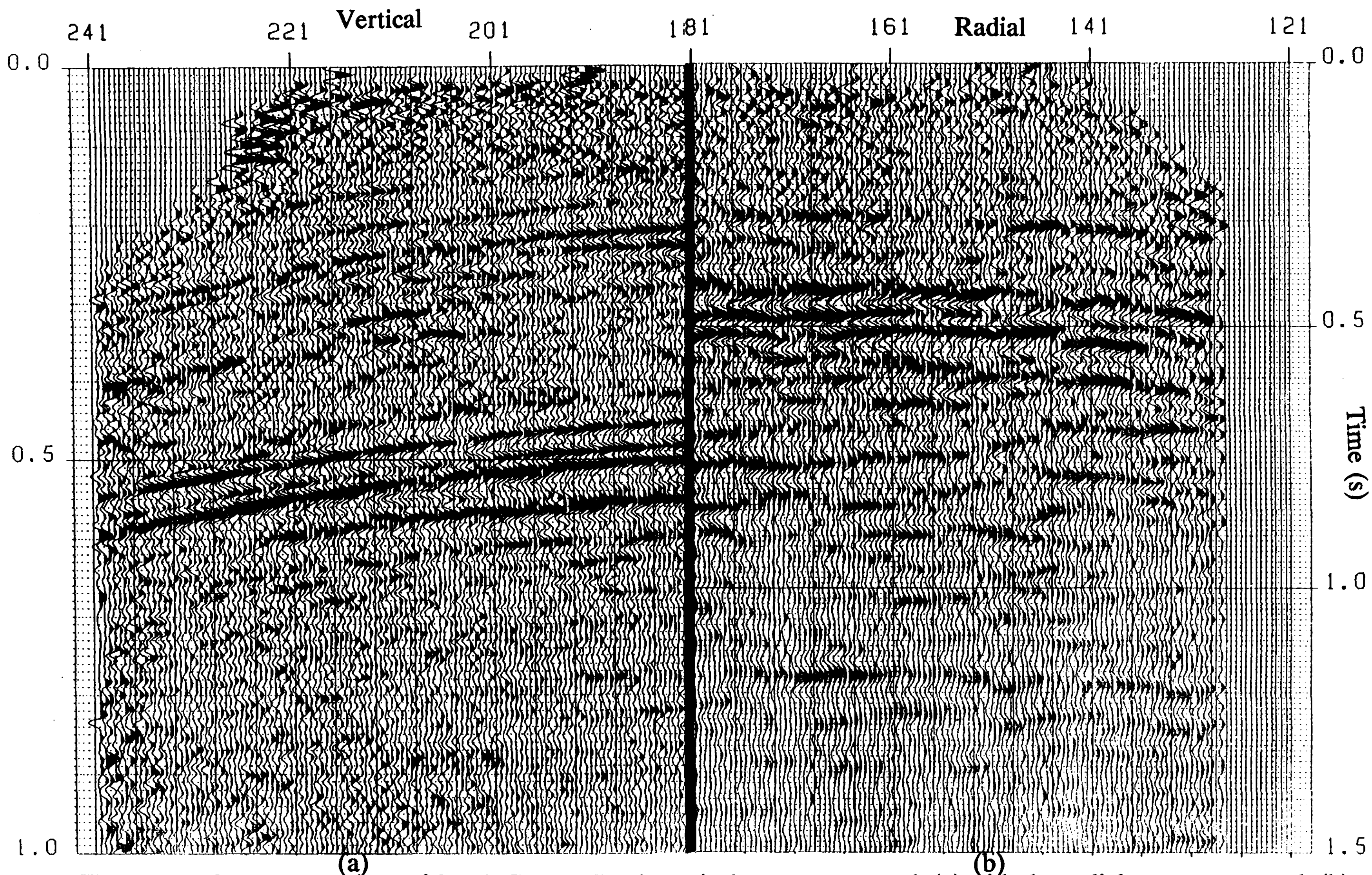

Figure 4.37 Cross-comparison of South Casper Creek vertical component stack (a) with the radial component stack (b).

Chapter 5 CONCLUSIONS

Conventional *f-k* filters and *f-k* weighted median filters are useful in removing coherent, random, and spiky noise from a shot gather before stacking. The median processes can edit bad traces or noise glitches, remove aliased dipping events, and reduce random noise in skewed distributions. The variance of the mean is 57% of the median variance for normal white noise. This suggests that mean processes are more effective in minimizing random noise. The weighted median process can be augmented with time domain coefficients to selectively remove dips, including aliased events, on a *x-t* gather. Tapering the *f-k* space dip filter edges (30% Nyquist) when creating these filter weights helps to collapse the size of this operator to optimize computer time. A fast 2-D weighted median algorithm was developed to provide virtual run time only 2.5 times the conventionally applied mean *f-k* process routinely used in seismic data processing.

The application of a 1-D linear frequency modulated compression operator before multichannel filtering of dispersive ground roll enhances the advantages of the median *f-k* filter; namely, dispersive ground roll can be compressed to a single aliased dip which is more easily filtered with this pre-stack filter. The dispersion of Rayleigh waves is primarily dependent on the near-surface S-wave thicknesses and velocities. Estimates of the dispersion parameters can be obtained by interpreting the S-wave refraction first breaks, ground roll apparent velocities on narrowband filter panels, or a multichannel ω-p transform. Accurate dispersion estimates can be made which enable optimal dispersion compression before multichannel filtering when at least two components of the seismic wavefield are recorded.

Careful acquisition parameters in the case of P-wave shallow reflection studies can avoid the problem of surface wave noise by staying within the optimum window. However, due to logistical limitations, this may not always be possible, and some form of ground roll filtering may be required. Converted P-SV shallow reflection studies are even more limited because the additional time delay due to the slower S-wave travel times reduces the available optimum window within which adequate signal-to-noise ratios can be obtained.

The inversion of Rayleigh wave dispersion patterns to estimate near-surface shear-wave velocities and thicknesses for shear statics or compression of dispersive noise for land seismic data is difficult. Lateral variations in these layers, the cost of dense spatial sampling, significant operator intervention, and over-all noise severely limit this application to land seismic data.

Chapter 6 FUTURE WORK

A recent improvement in the compression of dispersive seismic signals involves iteratively determining the curvature of the dispersion curve function rather than approximating it with a linear function (Boer et al, 1977). The criterion used for maximum compression is that the arrival envelope width is minimized. It may be possible to improve the linear approximated compression filter used in this study by adaptively predicting it on a shot-by-shot basis. An iterative method might be useful to perturb the linear approximation and minimize the dispersion.

The weighted median *f-k* algorithm developed here has been applied as a post-stack process to 3-D data (Stewart and Schieck, 1993). Appendix A demonstrates the errors in approximating a 3-D operator with axially rotated 2-D filter coefficients. An improvement to the 3-D algorithm is to incorporate the full 3-D operator. The development of a pre-stack 3-D dip filter would involve the interpolation of non-existent offsets to build a radially symmetric 3-D shot gather. Ground roll originating from the source would manifest itself as a 3-D noise cone on pre-stack records.

The potential of routinely recording and analysing shear-wave refractions as demonstrated in section 4.3.2 will improve our understanding of noise such as ground roll or poor data quality due to shallow layers at a seismic prospect. This might be extended to engineering and environmental applications where in-situ shear-wave parameters are often critical in investigations to estimate shear strength, fracture density, and orientation, or simply for discriminating the hydrostatic surface.

When applying the non-linear median *f-k* filter to pre-stack shear-wave records it may be advantageous to apply the often large statics pre-filter. This would be an off-line process and the statics would be removed before proceeding to the next processing step. This avoids the localized dip rejection capabilities of the median *f-k* filter that degrade true reflection events.

REFERENCES

Abo-Zena, A., 1979, Dispersion function computations for unlimited frequency values: Geophys. Journal R. Astr. Soc., 58, 1-105.

Abramowitz, M., and Stegan, I.A., 1972, Handbook of mathematical functions: Dover Publications Inc., 360.

Aki, K. and Richards, P.G., 1980, Quantitative seismology: Theory and methods, v.1: W.H. Freeman and Co.

Aldridge, D.F., 1992, Mathematics of Linear Sweeps: Canadian Journal of Expl. Geophys., 62-68.

Al-Husseini, M.I., Glover, J.B., and Barley, B.J., 1981, Dispersion patterns of the ground roll in eastern Saudi Arabia: Geophysics, 46, 121-137.

Bednar, J.B., 1983, Applications of median filtering to deconvolution, pulse estimation, and statistical editing of seismic data: Geophysics, 48, 1598-1610.

Bednar, J.B., and Watt, T.L., 1984, Alpha-trimmed means and their relationship to median filters: IEEE Trans. Acoust., Speech and Signal Processing, ASSP-32, 145-153.

Beresford-Smith, G., and Rango, R.N., 1988, Dispersive noise removal in *t-x* space: Application to Arctic data: Geophysics, 53, 346-358.

Beyer, W.H, 1982, Standard math tables: CRC press, Inc.

Boer, A.K., Chambers, J., and Mason,I.M., 1977, Fast numerical algorithm for the recompression of dispersed time signals: Electronics Letters, 13, 453-455.

Bovik, A.C., Huang, T.S., and Munson, D.C., Jr., 1983, A generalization of median filtering using linear combinations of order statistics: IEEE Trans. on Acoust., Speech and Sig. Proc., ASSP-31, 1342-1349.

Brune, J., and Dorman, J., 1963, Seismic waves and earth structure in the Canadian shield: Bull. Seism. Soc. Am., 53, 167-210.

Claerbout, J.F., 1985, Fundamentals of geophysical data processing: Blackwell Scientific Publications.

Claerbout, J.F., and Muir, F., 1973, Robust modelling with erratic data: Geophysics, 38, 826-844.

Dobrin, M.B., Simon, R.F., and Lawrence, P.L., 1951, Rayleigh waves from small explosions: Transactions, Am. Geophys. Union, 32, 822-832.

Doornbos, D.J., 1988, Seismological algorithms: Academic Press Ltd., 317-319.

Dziewonski, A.M., and Hales, A.L., 1972, Numerical analysis of dispersed surface waves *in* Methods in computational physics. Vol. 11, *ed:* Bolt, B.A., Academic Press.

Edelmann, H.A.K., and Helbig, K., 1987, Shear-wave surveys: Some aspects of field layout: *in* Shear Wave Exploration, Soc. Expl. Geophys., Geophysical development series, V.1, 165-179.

Evans, J.R., 1982, Running median filters and a general despiker: Bull. Seism. Soc. Am., 72, 331-338.

Fertig, J., and Krajewski, P., 1989, Acquisition and processing of pure and converted shear waves generated by compressional wave sources: Surveys in Geophysics 10, 103-132.

Gabriels, P., Snieder, R., and Nolet, G.,1987, In situ measurements of shear-wave velocity in sediments with higher-mode rayleigh waves: Geophys. Prosp. 35, 187-196

Glangeaud, F., 1990, Surface wave identification and filtering in multicomponent seismics: presented at the 60th Ann. Int. Mtg., Soc. Expl. Geophys., San Fransisco.

Green, R., 1986, An improved median window-filter to provide rounding of extreme values: Bull. Aust. Soc. Expl. Geophys. 17, 118-121.

Gurwitz, C., 1990, Weighted median algorithms for L_1 norm approximations, BIT, 30, 301-310.

Hampson, D., and Russell, B. H., 1984, First-break interpretation using generalized linear inversion: Canadian Journal of Expl. Geophys., 40-54.

Hardage, B.A., 1983, Vertical seismic profiling, Part A: Principles: Geophysical Press, London.

Haskell, N.A., 1953, The dispersion of surface waves on multilayered media: Bull. Seism. Soc. Am., 17-34.

Hatton, L., Worthington, M.H., and Makin, J., 1986, Seismic data processing, Blackwell Scientific Publications, 93-94.

Herrin, E., and Goforth, T., 1977, Phase matched filters: Applications to the study of Rayleigh waves: Bull. Seis. Soc. Am., 67, 1259-1275.

Herrmann, R.B., and Russell, D.R., 1990, Ground roll: Rejection using adaptive phase-matched filters: Geophysics, 55, 776-781.

Hiltunen, D.R., and Woods, R.D., 1989, Influence of source and receiver geometry on the testing of pavements by surface waves method: *in* Nondestructive testing of pavements and backcalculation of moduli, ASTM STP 1026, *ed:* A.J. Bush III and G.Y. Baladi, Am. Soc. for testing and materials, 138-154.

Huang, T.S., Yang, G.J., and Tong, G.Y., 1979, A fast two-dimensional median filtering algorithm: IEEE Trans. on Acoust., Speech, and Sig. Proc., ASSP-27, 13-18.

Hunter, J.A., Pullen, S.E., Burns, R.A., Gagne, R.M., and Good, R.L., 1984, Short note - Shallow seismic reflection mapping of the overburden-bedrock interface with the engineering seismograph- some simple techniques: Geophysics, 49, 1381-1385.

Justusson, B.J., 1981, Median filtering: Statistical properties: *in* Topics in applied physics: Vol.43, New York: Springer-verlag, Ch. 5.

Kirlin, R.L., Cudzilo, B., Wilson, S., 1985, Two-dimensional orthogonal median filters and applications: Proc. Internat. Conf. on Acoust., Speech and Sig. Proc., Tampa, Florida, 1325-1328.

Knopoff, L., 1952, On Rayleigh wave velocities: Bull. Seism. Soc. Am., 42, 37-308.

Landisman, M., Dziewonski, A., and Satô, Y., 1969, Recent improvements in the analysis of surface wave observations: Geophys. J.R. astro. Soc., 17, 369-403.

Lawton, D.C., 1990, A nine-component refraction seismic experiment: Canadian Journal of Expl. Geophys., 26, 7-16.

Lawton, D., and Harrison, M.P., 1990, A two-component reflection seismic survey, Springbank, Alberta: CREWES Project Research Report, 2, 123-163.

Leaney, W.S., and Ulrych, T.J., 1992, Compound median filtering and the median decomposition: Log processing applications: Journal Seismic Expl., 1, 173-190.

Liao, G., Nodes, T. A., and Gallagher Jr., N. C., 1985, Output distributions of two-dimensional median filters: IEEE Trans. on Acoust., Speech, and Sig. Proc., 33, 1280-1295.

Longbotham H.G., and Bovik, A.C., 1989, Theory of order statistic filter (OS) and their relationship to linear FIR filters: IEEE Trans. on Acoust., Speech, and Sig. Proc., 37, 275-287.

Mari, J.L., 1984, Estimation of static corrections for shear-wave profiling using the dispersion properties of Love waves: Geophysics, 49, 1169-1179.

McMechan G.A., and Yedlin, M.J., 1981, Analysis of dispersive waves by wavefield transformation: Geophysics, 46, 869-874.

Meskó, A., 1984, Digital filtering: Applications in geophysical exploration for oil: John Wiley and sons, 74-97.

Miller, S.L.M., Bertram, M.B., and Lawton, D.C., 1990, Source generated noise on multicomponent records: CREWES Research Report, University of Calgary, 2, 18-35.

Mooney, H.M., and Bolt, B.A., 1966, Dispersive characteristics of the first three Rayleigh modes for a single surface layer: Bull. Seism. Soc. of Am. 56, 43-67.

Narendra, P.M., 1978, Noise reduction by median filtering: Proc. IEEE Conf. Pattern Recognition.

Nazarian, S., and Stokoe, K.H., 1989, Nondestructive evaluation of pavements by surface wave methods: *in* Nondestructive testing of pavements and backcalculation of moduli, ASTM STP 1026, *ed* A.J. Bush III and G.Y. Baladi, Am. Soc. for testing and materials, 119-137.

Nolet, G., 1977, The upper mantle under western Europe inferred from the dispersion of Rayleigh waves: Journal of Geophysics, 43, 1169-1179.

Nolet, G. and Panza, G.F., 1976, Array analysis of seismic surface waves: limits and possibilities: Pure and Applied Geophysics, 114, 776-790.

Pitas, I., and Venetsanopoulos, A.N., 1986, Nonlinear order statistic filters for image filtering and edge detection: Signal Processing, 10, 395-413.

Press, W.H., 1986, Numerical Recipes: Cambridge University Press, Cambridge England.

Rix, G.J., Stokoe, K.H., and Roesset, J.M., 1990, Experimental determination of surface wave mode contributions: presented at the 60th Ann. Int. Mtg., Soc. Expl. Geophys., San Fransisco, 447-450.

Russell, B.H., 1989, Statics corrections - A tutorial: Recorder, Can. Soc. Expl. Geophys., 14(3), 16-30.

Russell, D.R., 1987, Multi-channel processing of dispersed surface waves: Ph. D. Thesis, Saint Louis University.

Saatçilar, R., and Canitez, N., 1988, A method of ground roll elimination: Geophysics, 53, 346-358.

Schwab, F.A., and Knopoff, L., 1972, Fast surface wave and free mode computation: *in* Bolt, B.A., ed., Methods in computational physics. Vol. 11, Academic Press, New York.

Song, Y.Y., Costagna, J.P., Black, R.A., and Knapp, R.W., 1989, Sensitivity of near-surface shear-wave velocity determination from Rayleigh and Love waves: presented at the 59th Ann. Int. Mtg., Soc. Expl. Geophys., Dallas, TX.

Stavig, G.R., and Gibbons, J.D., 1977, Comparing the mean and the median as measures of centrality: International Statistical Review, 44, 63-70.

Stewart, R.R., 1985, Median filtering: Review and a new f/k analogue design: Journal Can. Soc. Expl. Geophys., 21, 54-63.

Stewart, R.R., and Schieck, D.G., 1993, 3-D *f-k* filtering: Journal Seismic Expl., 2, 30-46.

Szelwis, R., and Behle, A., 1987, Shallow shear-wave velocity estimation from multimodal rayleigh waves: Shear wave exploration, Soc. Expl. Geophys., Tulsa, 214-226.

Takeuchi, H. and Saito, M., 1972, Seismic surface waves: in Bolt, B.A.,ed., Methods in Computational Physics, Vol. 11, Academic Press, New York, 217-295.

Thomson, W.T., 1950, Transmission of elastic waves through a stratified solid medium: Journal Appl. Phys., 21, 89-93.

Tolstoy, I., and Usdin, E., 1953, Dispersive properties of stratified elastic and liquid media: A ray theory: Geophysics, 18, 844-870.

Tukey, J.W., 1971, Exploratory Data Analysis: Addison-Wesley, Reading Massacheusetts.

Turin, G.L., 1960, An introduction to match filters: IRE Trans., 6, 311-329.

Turner, G., 1990, Aliasing in the tau-p transform and the removal of spatially aliased coherent noise, Geophysics, 55, 1496-1503.

Waters, K.H., 1978, Reflection Seismology: John Wiley and Sons, Inc.

Wattrus, N.J., 1989, Inversion of ground roll dispersion for near-surface shear-wave velocity variations: presented at the 59th Ann. Int. Mtg., Soc. Expl. Geophys., Dallas, TX.

Wirth, N, 1986, Algorithms and data structures: Prentice Hall, 98-100.

Yilmaz, O., 1987, Seismic data processing: Soc. Expl. Geophys., Investigations in Geophysics, Vol.2.

Yuan, D., and Nazarian, S., 1990, Economical mapping of variations in near-surface shear-wave velocity using high-frequency Rayleigh waves: presented at the 60th Ann. Int. Mtg., Soc. Expl. Geophys., San Fransisco, 451-454.

APPENDIX A

To create a 3-D time-domain operator it may seem intuitively correct to rotate a 2-D operator (in x,t) by 2π, around the time axis, to sweep out a 3-D cylinder. However, the full 3-D operator is not equivalent to an axially rotated 2-D operator. The inverse transform of a 3-D filter F can be defined as:

$$f(t,x,y)=\frac{1}{(2\pi)^3}\int\int\int_{-\infty}^{\infty} F(\omega,k_x,k_y)e^{i(\omega t+k_x x+k_y y)}dk_x dk_y d\omega \ . \qquad \text{(A.1)}$$

If the filter $F(w,k_x,k_y)$ is axially symmetric and the spatial components x and y are written as:

$$x=r\cos\phi \ , \qquad y=r\sin\phi$$

and frequency components as :

$$k_x=k_r\cos\alpha' \ , \qquad k_y=k_r\sin\alpha',$$

eq. (A.1) becomes:

$$f(t,r,\phi)=\frac{1}{(2\pi)^3}\int_{-\infty}^{\infty}\int_{0}^{2\pi}\int_{0}^{\infty} F(\omega,k_r)e^{i(\omega t+k_r r\cos(\alpha'-\phi))}k_r dk_r d\alpha' d\omega \qquad \text{(A.2)}$$

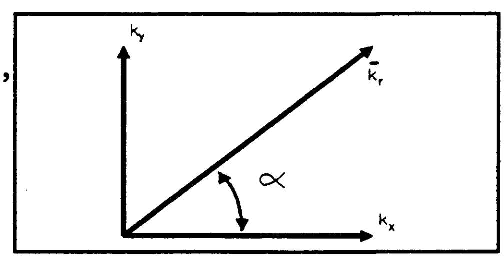

where $k_r=\sqrt{k_x^2+k_y^2}$, $r=\sqrt{x^2+y^2}$, $dk_x dk_y=k_r dk_r d\alpha'$,

and α' is the angle between the k_r and k_x axes. Substituting $\alpha=(\alpha'-\phi)$ in eq. (A2) we get the following integral (Meskó,1984):

$$f(t,r)=\frac{1}{(2\pi)^3}\int_{-\infty}^{\infty}\int_{0}^{\infty} F(\omega,k_r)k_r e^{i\omega t}\left[\int_{-\phi}^{2\pi-\phi} e^{ik_r r\cos\alpha}d\alpha\right]$$

$$=\frac{1}{(2\pi)^3}\int_{-\infty}^{\infty}\int_{0}^{\infty} F(\omega,k_r)k_r e^{i\omega t}\left[\int_{0}^{2\pi} e^{ik_r r\cos\alpha}d\alpha\right]$$

(A.3)

The integral formulation of a zero-order Bessel function (Abramowitz and Stegan, 1972) is:

$$2\pi J_0(u)=\int_0^{2\pi} e^{iucos\alpha}d\alpha \ . \tag{A.4}$$

Using (A.4) with (A.3) gives:

$$f(t,r)=\frac{1}{2\pi^2}\int_{-\infty}^{\infty}[\int_0^{\infty}F(\omega,k_r)k_rJ_0(k_rr)dk_r]e^{i\omega t}d\omega, \tag{A.5}$$

where the term in the square brackets is now a zero-order Hankel transform. Suppose $F(\omega,k_r)$ is a cylinder of radius a:

$$\begin{aligned} F(\omega,k_r) &= \frac{1}{2\pi a^2} \quad for \quad k_r \le a \\ &= 0 \qquad for \quad k_r > a. \end{aligned} \tag{A.6}$$

Substituting for $F(\omega,k_r)$, the filter operation becomes:

$$f(t,r)=\frac{1}{4\pi^3a^2}\int_{-\infty}^{\infty}[\int_0^{a}k_rJ_0(k_rr)dk_r]e^{i\omega t}d\omega \tag{A.7}$$

We can write the Hankel transform in (A.5) as:

$$\frac{1}{2\pi a^2}\int_0^{a}\frac{k_rr}{r}J_0(k_rr)dk_r \ . \tag{A.8}$$

The recurrence relation between the zero- and first-order Bessel function is:

$$\int uJ_0(u)du=uJ_1(u) \tag{A.9}$$

so if $u=k_r r$, $dk_r = \frac{1}{r}\, du$ and $0 \leq u \leq ar$ then the expression in (A.8) becomes:

$$\frac{rJ_1(ar)}{2\pi ar} \tag{A.10}$$

Finally, eq. (A.5) can be reduced to

$$f(t,r) = \frac{J_1(ar)}{(2\pi)^3 ar}\int_{-\infty}^{\infty} e^{i\omega t} d\omega \;=\; \frac{J_1(ar)}{(2\pi)^3 ar}\delta(t)\ . \tag{A.11}$$

This expression can be compared with the integral equation of the inverse 2-D transform of the same filter:

$$f(t,R) = \frac{1}{2\pi^2}\int\int_{-\infty}^{\infty} F(\omega,k_R) e^{i(\omega t + k_R R)} dk_R d\omega, \tag{A.12}$$

where R is the radius in 2-D along the x or y directions. Consider an axial slice through the previous 3-D disk to define a panel with a width of $2a$:

$$\begin{aligned} F(\omega,k_r) &= 1 \;\; for \;\; |k_r| \leq a \\ &= 0 \;\; for \;\; |k_r| > a\ . \end{aligned} \tag{A.13}$$

Then

$$\begin{aligned} f(t,R) &= \frac{1}{(2\pi)^2}\int_{-\infty}^{\infty}\Big[\int_{-a}^{a} e^{i(k_R R)} dk_R\Big] e^{i\omega t} d\omega = \frac{1}{(2\pi)^2} sinc(2aR)\int_{-\infty}^{\infty} e^{i\omega t} d\omega \\ &= \frac{1}{(2\pi)^2} sinc(2aR)\,\delta(t)\ . \end{aligned} \tag{A.14}$$

We see that the Hankel function is not equivalent to the integration of the same filter in the 2-D case. Figure A-1 compares the function of eq. (A.11) to that of eq. (A.14). This indicates that an axial slice of the 3-D time-domain operator is not equivalent to the 2-D operator. The filter time-domain response of these two equations is demonstrated in Figures A-2 and A-3 for a dip-reject filter of 4 ms/trace. While the two operators are similar they are not equivalent.

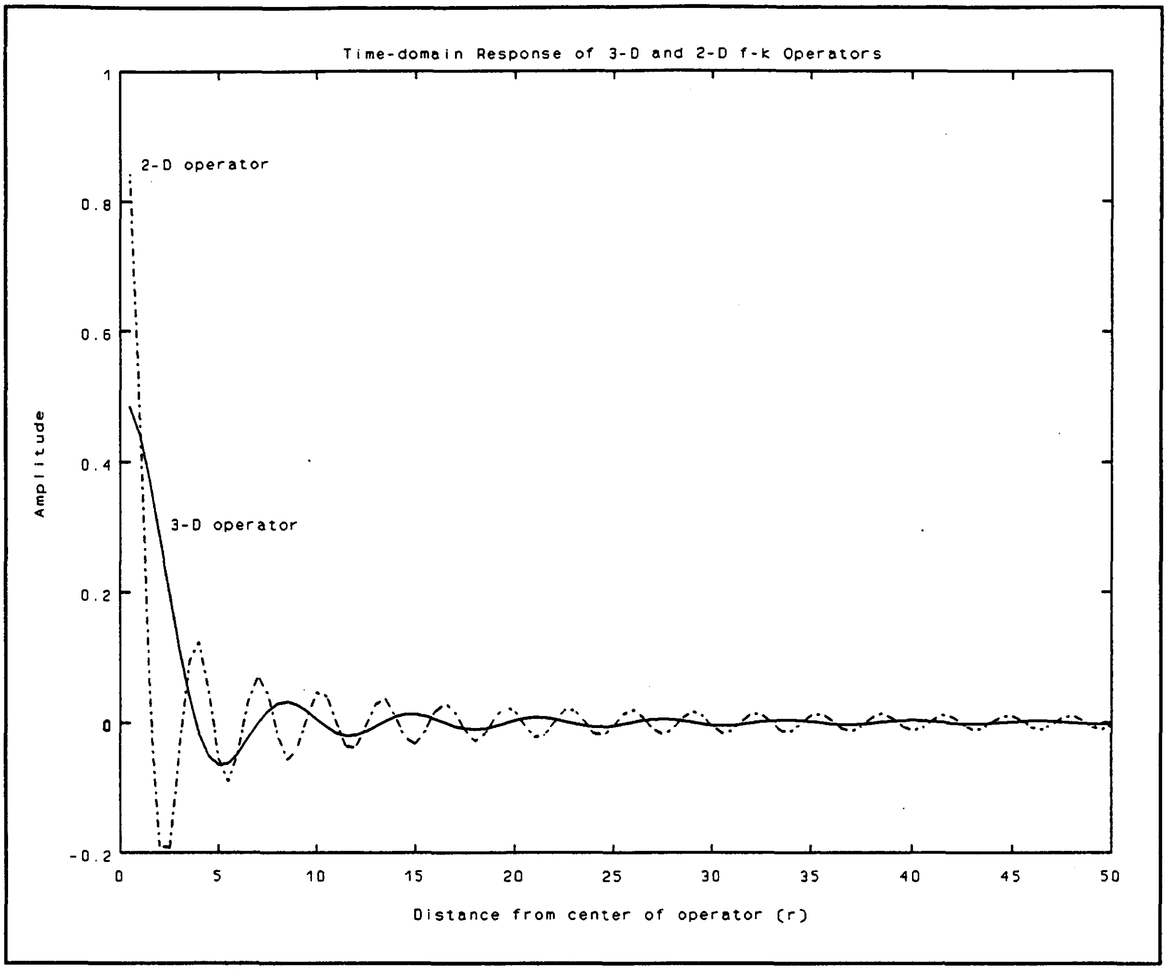

Figure A-1 $J_1(r)/r$ function of 3-D operator compared with sinc(2R) for 2-D filtering.

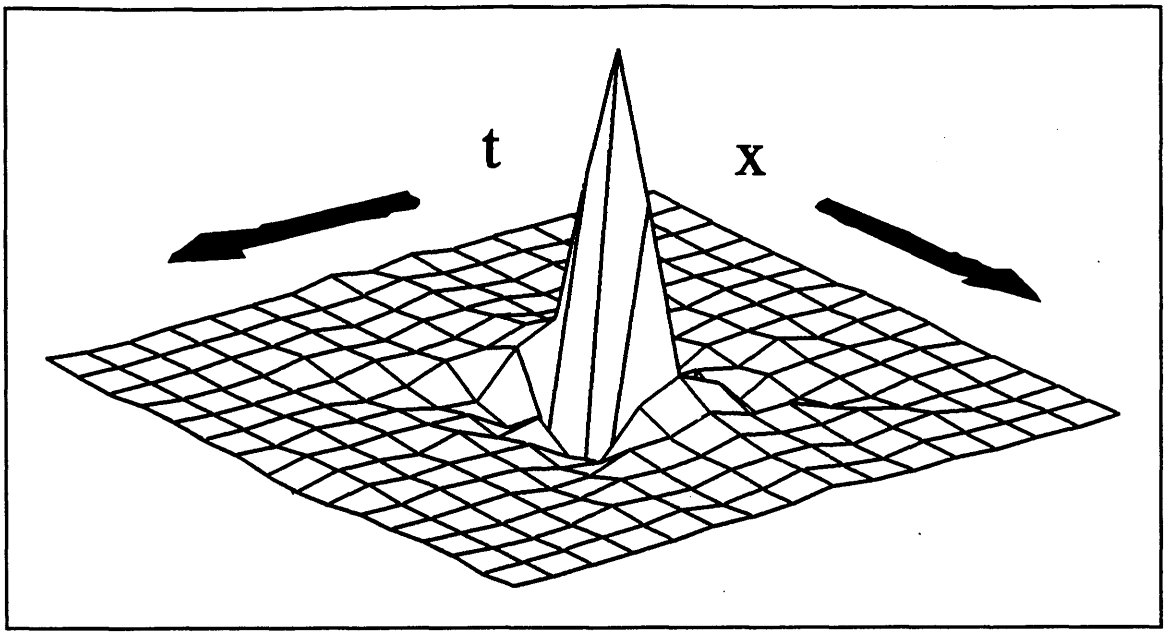

Figure A-2 2-D time-domain operator.

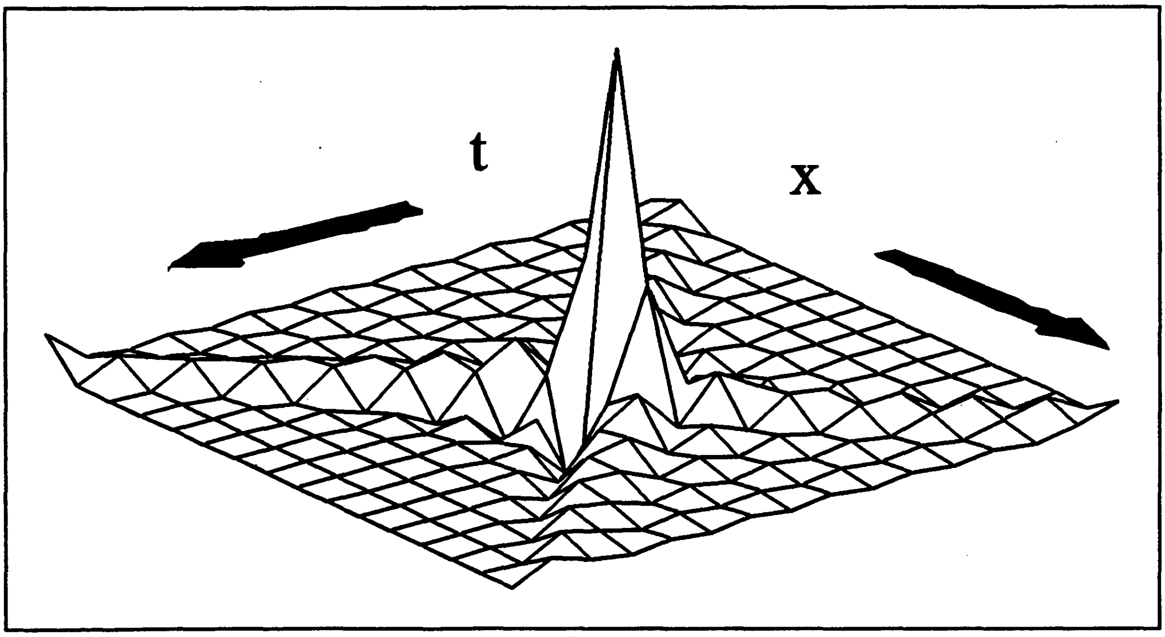

Figure A-3 Axial slice of 3-D time-domain operator.